UNIVERSITÀ DEGLI STUDI DI MILANO

Scuola di Dottorato in Fisica, Astrofisica e Fisica Applicata
Dipartimento di Fisica

Corso di Dottorato in Fisica, Astrofisica e Fisica Applicata
Ciclo XXXVIII

Strong gravitational lensing modeling of galaxy clusters in the Era of Big Data

Settore Scientifico Disciplinare FIS/05

Supervisor: Professor Marco LOMBARDI

Co-supervisor: Professor Claudio GRILLO

Coordinator: Professor Daniele MENNELLA

Tesi di Dottorato di: Davide Abriola
Matr. number: R13783
ORCID: 0009-0005-4230-3266

Anno Accademico 2024-2025

Commission of the final examination:

External Referee:
Professor Maruša BRADAČ

External Member:
Professor Raphael GAVAZZI

Internal Member:
Professor Luigi GUZZO

Final examination:

Date: 26 January 2026

Università degli Studi di Milano, Dipartimento di Fisica, Milano, Italy

To ...

Cover illustration:

The cover illustration is *Relativity*, a lithograph by the Dutch artist M. C. Escher, first printed in December 1953. I chose this piece of art as cover illustration of my Thesis since it represents an analogy with the different approaches that can be used to study galaxy clusters: X-ray- and dynamical-based studies, and gravitational lensing. Despite they rely on different hypotheses and methodologies, these techniques all contribute to give a complete view of galaxy clusters.

Internal illustrations:

This Thesis contains several illustrations. I will give each author credit for the images found in the literature. Where credit is not explicitly given, it refers to images produced by me in the context of this Thesis and related publications.

MIUR subjects:

FIS/05

PACS:

95.30.Sf, 98.62.Sb, 98.65.Cw

Contents

List of Figures

List of Tables

Introduction

Motivation

Galaxy clusters are the most massive gravitationally bound structures in the Universe. They grow hierarchically by accretion of matter along the filaments of the cosmic web and by mergers of smaller-scale galaxy groups. As such, they represent efficient gravitational lenses (GL). GL is the set of phenomena associated with the deflection of the light rays emitted by a background source (like quasars and galaxies) as they cross the gravitational well of a foreground mass distribution (a galaxy cluster, in the context of this Thesis), which therefore acts as a lens. In the inner cores of these deflectors, the density is sufficiently high to enable the production of multiple images and elongated arcs of background galaxies. This GL regime is called strong lensing (SL). SL by galaxy clusters is a well known phenomenon that can be used for the detailed reconstruction of the total mass of lens, without requiring any hypothesis about its nature, state or equilibrium conditions. In addition, SL clusters act as cosmic telescopes, allowing for the detection and study of faint and high-redshift sources, which would not be feasible otherwise. Finally, SL by clusters is a powerful cosmological tool: indeed, it enables to put constraints on the values of the parameters describing the structure and evolution of the Universe.

So far, the number of massive clusters displaying SL features is restricted to few tens. This scenario is set to drastically change thanks to current and future wide surveys (e.g. with the *Euclid* satellite and the Vera Rubin Observatory), which are expected to help increase this number by two orders of magnitude. Complementary, the James Webb Space Telescope (JWST) is providing us with images of unprecedented quality, allowing for the identification of new multiple images and smaller-scale structures than ever known, that can be used to put tighter constraints in high-precision lens models. During my PhD, I have focused on the modelling of the total mass distribution of galaxy clusters based on imaging with two telescopes, namely *Euclid* and the JWST, in order to quantify the limits and quality of the lens models and lensing-derived quantities of interest achievable using data collected with these facilities. The main motivations that have led to my research are summarised below.

A new modelling code: `Gravity.jl`. The amount of data being collected by *Euclid* and the JWST poses serious challenges from a computational point of view. In order to reconstruct the total mass distribution of a lens galaxy cluster, a parametric SL modelling code has to deal with hundreds to thousands of constraints, and to perform Bayesian inference over tens or even hundreds of parameters. Moreover, currently available softwares are not always able to correctly evaluate the qual-

ity of a lens model, to robustly compare different mass parametrisations, and adequately take into account potential systematics. These issues motivates the need of a next generation of SL codes capable of reconciling speed and accuracy, and `Gravity.jl` (Lombardi 2024) finds itself in this context. `Gravity.jl` is a Julia-written proprietary software specifically developed for cluster-scale SL analyses. Its high-performance architecture makes it ideally suited for processing the large and complex datasets from these and next-generation observatories. During my PhD, I contributed in testing, applying, and validating the robustness of this code.

Strong Gravitational Lensing in the Era of Big Data. As anticipated above, current and future facilities are providing us with a large stream of data that will enable SL analyses of unprecedented precision. One the one hand, *Euclid* will enlarge the number of massive clusters showing SL features by two orders of magnitude. On the other, the JWST is providing images of unparallel quality. It is therefore necessary to quantify the robustness and accuracy of the lens models based on data acquired with these facilities, and here my PhD finds place. In particular, the unequalled number of constraints provided by the JWST demands a proper modelling of the mass distribution of lens cluster, with the line-of-sight (los) structures correctly put at their redshift (i.e., a full multi-plane lensing study). Complementarily, *Euclid*-based observations will be wider but shallower than the ones with the JWST, thus resulting in a limited number of SL features to be identified. Hence, it is mandatory to explore the limits of SL studies allowed with this telescope.

In summary, SL by galaxy clusters is the most robust tool to reconstruct their total mass distribution. It is also a competitive cosmological tool, if compared to other probes. To reach these aims, accurate mass modelling is crucial, and this represents the core of my PhD. With this Thesis work, I intend to contribute to the scientific progress on this interesting topic.

Thesis overview

Main results

Driven by the motivations described above, we intend to show in this Thesis the accuracy achievable by SL models based on *Euclid* and JWST imaging, thus providing case studies of the precision expected by next-generation SL analyses in the Era of Big Data. The main results of the Thesis are summarized below.

SL analysis of the *Euclid* ERO galaxy cluster Abell 2390. Soon after its lauch, the *Euclid* telescope targeted two galaxy clusters as part of the Early Release Observations (ERO, Cuillandre et al. 2024) program Magnifying Lens (P.I.: Atek, H., Atek et al. 2024). This program was designed to showcase the science questions that *Euclid*'s observations of galaxy clusters will be able to address, and to reveal and address challenges and limitations for a full scientific exploitation of the prime mission survey data. One of the two galaxy clusters observed was Abell 2390, which was targeted on 28 November 2023. For this cluster, we developed the very first SL parametric model entirely based on *Euclid* multi-band imaging. We also relied on archival deep spectroscopic data with the MUSE instrument. We performed our analysis with `Gravity.jl`, whose speed allowed us to test and compare more than 10 total mass parametrizations and explore potential systematics arising in modeling choices (Abriola et al., sub.).

A glimpse of SL by galaxy clusters in the *Euclid* era. Abell 2390 was a particular cluster, since it was given dedicated time to obtain deep observations. *Euclid*-like imaging of galaxy clusters are less deep, thus resulting in the identification of a reduced number of multiple images. Additionally, they would possibly not benefit from planned spectroscopic follow-up, which is a crucial ingredient to build accurate SL models. We therefore quantified the impact these limitations may have on future SL studies, in particular on SL-derived quantities of interest, including the total mass distribution. We faced the problem through a statistical approach: we generated hundreds of lens models by considering subsets of randomly extracted multiple images.

JWST-based SL analysis of the galaxy cluster MACS J0416.1-2403. After exploring the limits achievable through typical *Euclid*-based SL analyses of galaxy clusters, in the context of wide field surveys, we examined the complementary potentialities offered by high-precision JWST imaging. We modelled the galaxy cluster MACS J0416.1-2403 using multi-band JWST imaging data and archival spectroscopy. Starting from the available catalogs of multiple images, we managed to identify new images and new substructures, hence producing a lens model characterised by the highest number of spectroscopically-confirmed multiple images to date, with nearly 500 elements. In doing so, we exploited the full potential of `Gravity.jl` and performed the first multi-plane lensing analysis of this cluster. This work allowed us to further test the capabilities of this software. Whereas the optimization of the lens model of the same cluster carried out with different codes required up to a month to be performed, with `Gravity.jl` we were able to carry out the same studies in less than a week.

Organizational note

The present Thesis consists of three Parts, for a total of six Chapters. Part I is devoted to the presentation of strong gravitational lensing in galaxy clusters and its applications. It is composed of Chapters 1, 2 and 3, and presents an introduction to the theory of strong gravitational lensing, a brief recall on galaxy clusters and how strong lensing analyses are performed. Part II is dedicated to the results obtained with *Euclid*. Chapter 4 focuses to the analysis of the galaxy cluster Abell 2390 with *Euclid* imaging, whereas in Chapter 5 we draw some statistical considerations about strong lensing in the Eulid era. Part III, which actually corresponds solely to Chapter 6, is dedicated to strong lensing with the James Webb Space Telescope. Some variations have been made in the presentation of previously published results, to maintain consistency of style and content structure through the manuscript. Throughout this Thesis, we adopt a flat ΛCDM cosmology with $\Omega_{\rm m} = 0.3$ and $H_0 = 70\,{\rm km\,s^{-1}\,Mpc^{-1}}$. All magnitudes are expressed in the AB system.

Part I
Gravitational lensing

CHAPTER 1

An introduction to gravitational lensing

Light rays emitted by a background astronomical source (like a star, a quasar, or a galaxy) can be deflected as they cross the gravitational potential generated by a foreground mass distribution (as a galaxy and a cluster of galaxies), which therefore acts as a lens, or deflector. The set of phenomena associated with this occurrence is collectively known as *gravitational lensing* (GL). Despite first studies around the hypothetical deflection of light rays by massive objects date back to the XVIII century (see Schneider et al. 1992, for an historical review), it was only in the context of the General Relativity (GR) (Einstein 1915, 1936; Zwicky 1937b) that GL was fully developed as a firm theory. The very first confirmation of GL, which in turn represented the first evidence in support of GR, was indeed the measurement of the deflection angle of a light ray grazing the surface of the Sun during the solar eclipse of 1919, which confirmed the predictions of GR (Dyson et al. 1920).

More distant, more massive, or more compact cosmic bodies than the Sun may bend light rays from a background source sufficiently strongly such that multiple light rays from the background astronomical object can reach an observer. The observer thus sees an image in the direction of each ray, so that the source appears multiply imaged. This is the *strong* gravitational lensing (SL) regime. The first multiple-image system was discovered only in 1979 (Walsh et al. 1979): two multiple images of the quasar Q0957+561, at redshift $z = 1.405$. In 1986, Lynds & Petrosian (1986) announced the discovery of the first *luminous arc*, i.e., a highly-distorted image of a high-redshift galaxy seen through a massive foreground galaxy cluster, Abell 2390. From then on, GL has become one of the most active fields of research in extragalactic astronomy.

GL has developed into a robust and versatile tool for observational cosmology and astrophysics. In particular, the main applications of GL are the following (please refer to Chapter 2 for a more detailed discussion):

Total mass distribution. The deflection angle of the light rays depends neither on the nature of the mass distribution bending the rays nor on its physical state or symmetry assumptions, e.g. temperature, composition, etc. In other words, light deflection probes the total matter density, without distinguishing between ordinary (baryonic) or dark matter (DM). Hence, GL is a powerful probe to reconstruct the total mass distribution of the lens, and gives the possibility to directly investigate the DM distribution, once the baryonic component has been properly mapped out. This potentiality has led to substantial results over recent years. However, lensing measures only the mass distribution projected along the line of sight, and is therefore insensitive to the extent of the lens along the light rays, as long as this extent is small compared to the distances from the observer and the source to the deflecting mass.

GL as cosmic telescopes. Strong lenses act as cosmic telescopes, allowing us to probe faint sources in the background Universe. Indeed, SL magnifies distant, faint background galaxies that would otherwise remain inaccessible and can lead to the discovery of high-redshift sources (Atek et al. 2023a,b; Roberts-Borsani et al. 2023).

Cosmology applications. SL can be exploited to probe the geometry and expansion rate of the Universe. Indeed, as was first pointed out by Refsdal (1964), this phenomenon can be used to measure the expansion rate of the Universe at the current epoch, namely the Hubble constant, in case multiply-imaged background sources are subject to luminosity variation over time. Additionally, in case two or more background sources at different redshifts are multiply-lensed by the same deflector, their distance ratios provide constraints on the value of key cosmological parameters.

In this Chapter, we give a brief introduction to the theory of GL, with a specific regard for SL. We invite the reader to Schneider et al. (1992), Bartelmann & Schneider (2001) and Meneghetti (2022) for a more exhaustive overview of the topic. The content of this Chapter is based on the above-mentioned references.

1.1 The deflection angle

The study of GL has to be properly developed through the use of GR, since it yields the correct expression for the deflection angle of light rays, which is twice the value found with classical mechanics. Nonetheless, in almost every astrophysically relevant case of GL, we may consider a Minkowski metric weakly deformed by a mass distribution. If this were the case, the metric following from Einstein's field equations of GR assumes the following form,

$$\mathrm{d}s^2 = \left[1 + \frac{2}{c^2}\phi(\boldsymbol{x})\right] c^2 \mathrm{d}t^2 - \left[1 - \frac{2}{c^2}\phi(\boldsymbol{x})\right] \mathrm{d}\boldsymbol{x}^2 \,, \tag{1.1}$$

where $\phi(\boldsymbol{x}) < 0$ is the value of the gravitational potential ϕ associated with the mass distribution in a point $\boldsymbol{x}$ of space. Light rays propagate along null geodesics, i.e., along curves characterised by $\mathrm{d}s^2 = 0$. If we impose this condition, a relationship between $|\mathrm{d}\boldsymbol{x}|$ and $\mathrm{d}t$ follows, yielding a kind of *effective* velocity for the light as it propagates through the gravitational field. This allows us to describe GL by introducing an effective refraction index $n = n(\boldsymbol{x})$ that locally depends on the gravitational potential. Indeed,

$$\mathrm{d}s^2 = 0 \Longrightarrow \left|\frac{\mathrm{d}\boldsymbol{x}}{\mathrm{d}t}\right| = \left[1 + \frac{2}{c^2}\phi(\boldsymbol{x})\right]^{\frac{1}{2}} \left[1 - \frac{2}{c^2}\phi(\boldsymbol{x})\right]^{-\frac{1}{2}} c \simeq \left(1 + \frac{2}{c^2}\phi(\boldsymbol{x})\right) c \,, \tag{1.2}$$

where we exploited the fact that space is only weakly perturbed by the mass distribution, i.e., the weak field limit $\phi \ll c^2$, and proceeded with a McLaurin expansion to the first order. We can then define the effective refraction index $n(\boldsymbol{x})$ as

$$n(\boldsymbol{x}) = c \left|\frac{\mathrm{d}\boldsymbol{x}}{\mathrm{d}t}\right|^{-1} = \left[1 + \frac{2}{c^2}\phi(\boldsymbol{x})\right]^{-1} \simeq 1 - \frac{2}{c^2}\phi(\boldsymbol{x}) \,, \tag{1.3}$$

where, in the last step, we performed a further expansion. Since $\phi(\boldsymbol{x}) < 0 \,\forall \boldsymbol{x}$, it follows that $n > 1$, i.e., light is slowed down when it propagates through a gravitational field. Moreover, as can be noticed, the effective refraction index does not depend either on

the wavelength of the radiation, or, equivalently, on its frequency, as it might have been expected in a classical optical system, but only on the gravitational potential, thus the mass distribution of the lens. The vacuum gravitational field acts therefore as a non-dispersive medium and gravitational lenses are thus perfectly *achromatic*. This means that every image of the same source is observed with the same colour and the same absorption and emission spectrum of the source: consequently, we can study the physical properties of the lensed source by analysing its images.

In order to derive the expression of the deflection angle, let us first determine the time Δt the light takes to cross a gravitational field along a trajectory γ, given by

$$c\Delta t = \int_\gamma n(\boldsymbol{x})\mathrm{d}l = \int_\gamma \left(1 - \frac{2}{c^2}\phi(\boldsymbol{x})\right)\mathrm{d}l = |\gamma| + \frac{2}{c^2}\int_\gamma |\phi(\boldsymbol{x})|\mathrm{d}l\,, \tag{1.4}$$

where $|\gamma|$ is the length of the trajectory and $\mathrm{d}l$ is the infinitesimal segment parallel to the path. Then, the Euler-Lagrange equations applied to Fermat's principle $-$ which states that a null smooth curve γ connecting a source to an observer is a geodetic line if and only if its arrival time to the observer is stationary with respect to small perturbations of γ $-$ yield the following relation (Meneghetti 2022),

$$\frac{\mathrm{d}\boldsymbol{e}}{\mathrm{d}l} = \nabla_\perp n(\boldsymbol{x}) = -\frac{2}{c^2}\nabla_\perp\phi(\boldsymbol{x})\,. \tag{1.5}$$

Here, $\boldsymbol{e}$ is a versor tangent to the light path, i.e., it gives the direction of light rays, whereas $\nabla_\perp n(\boldsymbol{x})$ is the component of the gradient orthogonal to $\boldsymbol{e}$: $\nabla_\perp n(\boldsymbol{x}) = \nabla n(\boldsymbol{x}) - [\nabla n(\boldsymbol{x})\cdot\boldsymbol{e}\,]\boldsymbol{e}$. Hence, the deflection angle $\hat{\boldsymbol{\alpha}}$ is given by the difference between the initial $\boldsymbol{e}_i$ and the final direction $\boldsymbol{e}_f$ after travelling along γ,

$$\hat{\boldsymbol{\alpha}} = \boldsymbol{e}_i - \boldsymbol{e}_f = -\int_\gamma \frac{\mathrm{d}\boldsymbol{e}}{\mathrm{d}l}\mathrm{d}l = \frac{2}{c^2}\int_\gamma \nabla_\perp\phi(\boldsymbol{x})\mathrm{d}l\,. \tag{1.6}$$

This integral has to be evaluated along the path γ followed by light rays, which in turn depends on the deflection itself. Anyway, in the weak field limit, we may approximate the integral with a calculation along a straight and unperturbed ray, a solution called Born or impulsive approximation. The potential associated with a generic tridimensional mass distribution of density $\rho(\boldsymbol{x})$ is

$$\phi(\boldsymbol{x}) = -G\int \frac{\rho(\boldsymbol{x}')}{|\boldsymbol{x}-\boldsymbol{x}'|}\,\mathrm{d}^3x'\,. \tag{1.7}$$

Consequently, the deflection angle is

$$\hat{\boldsymbol{\alpha}}(\boldsymbol{\xi}) = \frac{4G}{c^2}\int \Sigma(\boldsymbol{\xi}')\frac{\boldsymbol{\xi}-\boldsymbol{\xi}'}{|\boldsymbol{\xi}-\boldsymbol{\xi}'|^2}\,\mathrm{d}^2\xi'\,, \tag{1.8}$$

after projecting the tridimensional mass density $\rho(\boldsymbol{x}) = \rho(\boldsymbol{\xi}, z)$ along the line of sight, i.e., the path of the light, represented by the z-coordinate, to get the surface mass density $\Sigma(\boldsymbol{\xi})$ ($\boldsymbol{\xi}$ is the coordinate orthogonal to the line of sight):

$$\Sigma(\boldsymbol{\xi}) = \int \rho(\boldsymbol{\xi}, z)\,\mathrm{d}z\,. \tag{1.9}$$

If we consider a point-like mass M, the deflection angle of a light ray with impact parameter $\boldsymbol{\xi}$ given by Eq. (1.8) reduces to

$$\hat{\boldsymbol{\alpha}} = \frac{4GM}{c^2}\frac{\boldsymbol{\xi}}{|\boldsymbol{\xi}|^2} \,. \tag{1.10}$$

If the lens is instead composed of N point-like masses $\{M_i\}_{i=1}^N$, all concentrated in a region whose typical length scale is well smaller than the distances observer-deflector and deflector-background source, then, by virtue of the weak field limit, the gravitational effects can be linearised, and the total deflection angle $\hat{\boldsymbol{\alpha}}$ of a light ray crossing the lens plane in $\boldsymbol{\xi}$ can be assumed to be the vectorial sum of the single deflection angles $\{\hat{\boldsymbol{\alpha}}_i\}$ due to the single masses lying at positions $\{\boldsymbol{\xi}_i\}$ (superposition principle),

$$\hat{\boldsymbol{\alpha}}(\boldsymbol{\xi}) = \sum_{i=1}^{N} \frac{4G}{c^2} M_i \frac{\boldsymbol{\xi} - \boldsymbol{\xi_i}}{|\boldsymbol{\xi} - \boldsymbol{\xi_i}|^2} \,. \tag{1.11}$$

As can be seen from the previous equations, the deflection angle depends only on the surface mass density of the lens, i.e. its tridimensional density projected along the line of sight. Lensing analysis can therefore lead to the determination of the surface density only, not the full tridimensional one, as briefly mentioned above.

1.2 The lens equation

Let us now consider the typical GL configuration, sketched in Figure 1.1. The lens lies at redshift $z_{\rm d}$ (or, equivalently, at the angular-diameter distance $D_{\rm d}$ from an observer), and deflects the light rays emitted by a background astronomical source at redshift $z_{\rm s}$ (angular-diameter distance $D_{\rm s}$ from the observer). Let $D_{\rm ds}$ be the mutual distance between the deflector and the source. Suppose the lens is *geometrically thin*, i.e., the mass distribution of the deflector has a typical length scale much smaller than both $D_{\rm s}$ and $D_{\rm ds}$. Hence, we may assume that all the mass elements of the lens lie on a single plane, called the *lens plane* at distance $D_{\rm d}$ from the observer. In the absence of other deflectors along the line of sight, we can describe the deflection as a kink on the lens plane, quantified by the deflection angle $\hat{\boldsymbol{\alpha}}$. This assumption is verified in most of the cases of interest for GL: galaxies have a typical length scale $\simeq 100$ kpc, whereas clusters of galaxies have a characteristic value $\simeq 1$ Mpc. For typical values of the redshift of the astronomical sources involved in GL, the corresponding angular-diameter distances are of the order of the Gpc, i.e. well greater than the previous length scales.

Let $\boldsymbol{\xi}$ represent the position of the image of a source on the lens plane, and, similarly, $\boldsymbol{\eta}$ the position of the source itself on the so-called *source plane*. Both these two-dimensional vectors refer to the origin of a suitable frame of reference introduced on the planes. To that end, it is useful to define a straight line through the observer and the center of the lens, known as the *optical axis* (the *bold dotted line* of Figure 1.1). The coordinate frames in the source and lens plane can therefore be chosen to have their origin on the point of intersection of the optical axis with the corresponding plane, as depicted in the previous sketch. Finally, we introduce $\boldsymbol{\theta}$ and $\boldsymbol{\beta}$ as the angular positions of the source and the image with respect to the observer, which are related to the previous vectors by

$$\boldsymbol{\eta} = D_{\rm s}\boldsymbol{\beta} \,, \tag{1.12}$$

$$\boldsymbol{\xi} = D_{\rm d}\boldsymbol{\theta} \,. \tag{1.13}$$

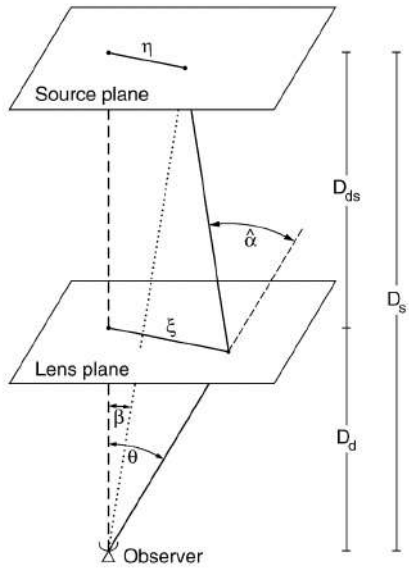

Figure 1.1: Sketch of a typical GL configuration. Credits: Bartelmann & Schneider (2001).

In order to obtain a relation between the position of the image as seen by the observer and the true position of the source, let us begin with the following trigonometric relation, that holds for $\hat{\boldsymbol{\alpha}} \ll 1$ and that can be verified by looking at Figure 1.1:

$$D_\mathrm{s}\boldsymbol{\beta} \simeq D_\mathrm{s}\boldsymbol{\theta} - D_\mathrm{ds}\,\hat{\boldsymbol{\alpha}}(\boldsymbol{\theta})\ . \tag{1.14}$$

By dividing both members of Eq. (1.14) by D_s, we gain

$$\boldsymbol{\beta} = \boldsymbol{\theta} - \frac{D_\mathrm{ds}}{D_\mathrm{s}}\,\hat{\boldsymbol{\alpha}}(D_\mathrm{d}\boldsymbol{\theta}) = \boldsymbol{\theta} - \boldsymbol{\alpha}(\boldsymbol{\theta})\ , \tag{1.15}$$

where

$$\boldsymbol{\alpha}(\boldsymbol{\theta}) = \frac{D_\mathrm{ds}}{D_\mathrm{s}}\,\hat{\boldsymbol{\alpha}}(D_\mathrm{d}\boldsymbol{\theta}) \tag{1.16}$$

is called *scaled* deflection angle. Eq. (1.15) is called *ray-tracing* or *lens* equation, and describes a mapping $\boldsymbol{\theta} \mapsto \boldsymbol{\eta}$ from the lens plane to the source plane, relating the image position to the true position of the source. This mapping is generally not one-to-one since a source can have more than one image (as in the case of SL), therefore the inversion $\boldsymbol{\eta} \mapsto \boldsymbol{\theta}$ is usually carried out via numerical methods.

We can rewrite the expression of the scaled deflection angle in Eq. (1.16) as

$$\begin{aligned}\boldsymbol{\alpha}(\boldsymbol{\theta}) = \frac{D_\mathrm{ds}}{D_\mathrm{s}}\,\hat{\boldsymbol{\alpha}}(D_\mathrm{d}\boldsymbol{\theta}) = \frac{4G}{c^2}\,\frac{D_\mathrm{ds}}{D_\mathrm{s}}\int D_\mathrm{d}\Sigma(\boldsymbol{\theta}')\frac{\boldsymbol{\theta}-\boldsymbol{\theta}'}{|\boldsymbol{\theta}-\boldsymbol{\theta}'|^2}\mathrm{d}^2\theta' = \\ = \frac{1}{\pi}\int\frac{4\pi G}{c^2}\,\frac{D_\mathrm{ds}}{D_\mathrm{s}}D_\mathrm{d}\Sigma(\boldsymbol{\theta}')\frac{\boldsymbol{\theta}-\boldsymbol{\theta}'}{|\boldsymbol{\theta}-\boldsymbol{\theta}'|^2}\mathrm{d}^2\theta' = \frac{1}{\pi}\int\frac{\Sigma(\boldsymbol{\theta}')}{\Sigma_\mathrm{c}}\frac{\boldsymbol{\theta}-\boldsymbol{\theta}'}{|\boldsymbol{\theta}-\boldsymbol{\theta}'|^2}\mathrm{d}^2\theta'\,.\end{aligned} \tag{1.17}$$

where we introduced the quantity

$$\Sigma_{\rm c} = \frac{c^2}{4\pi G}\,\frac{D_{\rm s}}{D_{\rm ds}\,D_{\rm d}}\,, \tag{1.18}$$

called *critical* surface mass density, a parameter which does not depend on the mass distribution of the lens or any of its characteristics, but is a geometrical parameter depending only on the angular-diameter distances involved.

In order to have a strong lens, i.e., a lens capable of producing multiple images (such that, for fixed source position $\boldsymbol{\beta}$, the lens equation admits more than one solution), it is sufficient (see Sect. 1.4, Condition II) to have $\Sigma \geq \Sigma_{\rm cr}$ somewhere on the lens plane, or, equivalently, $\kappa \geq 1$, with

$$\kappa(\boldsymbol{\theta}) = \frac{\Sigma(\boldsymbol{\theta})}{\Sigma_{\rm c}} \tag{1.19}$$

called the dimensionless surface mass density, or *convergence*. We can rewrite the expression of the scaled deflection angle introducing the convergence as

$$\boldsymbol{\alpha}(\boldsymbol{\theta}) = \frac{1}{\pi}\int \kappa(\boldsymbol{\theta}')\frac{\boldsymbol{\theta}-\boldsymbol{\theta}'}{|\boldsymbol{\theta}-\boldsymbol{\theta}'|^2}{\rm d}^2\theta' = \nabla_\theta\,\psi(\boldsymbol{\theta})\,, \tag{1.20}$$

which allows us to express $\boldsymbol{\alpha}$ as the gradient of the *deflection potential*

$$\psi(\boldsymbol{\theta}) = \frac{1}{\pi}\int \kappa(\boldsymbol{\theta}')\ln|\boldsymbol{\theta}-\boldsymbol{\theta}'|{\rm d}^2\theta'\,, \tag{1.21}$$

as $\boldsymbol{\alpha} = \nabla_\theta\,\psi$. The deflection potential is the two-dimensional analogue of the Newtonian potential, and satisfies the Poission equation $\nabla^2\psi(\boldsymbol{\theta}) = 2\kappa(\boldsymbol{\theta})$. The deflection potential $\psi(\boldsymbol{\theta})$ is related to the gravitational potential $\phi(D_{\rm d}\boldsymbol{\theta}, z)$ of the lens through a projection along the line of sight (given by the z-direction),

$$\psi(\boldsymbol{\theta}) = \frac{2}{c^2}\frac{D_{\rm ds}}{D_{\rm d}D_{\rm s}}\int\left|\phi(D_{\rm d}\boldsymbol{\theta}, z)\right|{\rm d}z\,. \tag{1.22}$$

1.3 Magnification and distortion

Let us suppose now that the typical length scale of a source in $\boldsymbol{\beta}$ and observed in $\boldsymbol{\theta}$ is much smaller than the characteristic scale on which the properties of the deflector change. In this case, we may linearise the lens equation locally, in a neighbourhood of $\boldsymbol{\theta}$, by Taylor expanding the equation to the first order around the centre $\boldsymbol{\theta}_c$ of the image, assumed for simplicity to be zero, $\boldsymbol{\theta}_c = 0$. We also assume that the lensed position of $\boldsymbol{\theta}_c$ on the lens plane through the ray-tracing equation vanishes as well. To do so, we introduce a Jacobian matrix $A = A(\boldsymbol{\theta})$ that accounts for the distortion of the source image, and express Eq. (1.15) as

$$\boldsymbol{\beta} \simeq A(\boldsymbol{\theta})\cdot\boldsymbol{\theta}\,, \tag{1.23}$$

by expressing the relationship for the single components of the two-dimensional vectors. We then apply the Einstein convention on repeated indexes,

$$\beta_i = A_{ij}\,\theta_j = \frac{\partial\beta_i}{\partial\theta_j}\,\theta_j\,, \tag{1.24}$$

where the indexes i and j run over the two components of $\boldsymbol{\theta}$ and $\boldsymbol{\beta}$. Therefore, given the ray tracing equation expressed through the lensing potential, we can rewrite

$$A_{ij} = \frac{\partial \beta_i}{\partial \theta_j} = \frac{\partial}{\partial \theta_j}[\theta_i - \alpha_i(\boldsymbol{\theta})] = \frac{\partial}{\partial \theta_j}\left[\theta_i - \frac{\partial \psi}{\partial \theta_i}(\boldsymbol{\theta})\right] = \delta_{ij} - \frac{\partial^2 \psi}{\partial \theta_j \partial \theta_i}(\boldsymbol{\theta})\,, \tag{1.25}$$

with δ_{ij} Kronecker's delta. If we now represent the partial derivative of ψ with respect to both the ith and the jth component of $\boldsymbol{\theta}$ as $\psi_{,ij}$, the Jacobian (or *lensing*) matrix A can be expressed as

$$A(\boldsymbol{\theta}) = \begin{pmatrix} 1 - \psi_{,11} & -\psi_{,12} \\ -\psi_{,12} & 1 - \psi_{,22} \end{pmatrix}. \tag{1.26}$$

The components of A can be rewritten after introducing a quantity known as *shear*, indicated as γ. This quantity can be expressed in a complex notation as

$$\gamma = \gamma_1 + i\gamma_2 = |\gamma| e^{2i\omega}\,, \tag{1.27}$$

where the factor reminds that the shear is not a vector, since it does not transform as such. The components γ_1 and γ_2 of the shear are related to the derivatives of ψ through

$$\gamma_1 = \frac{1}{2}(\psi_{,11} - \psi_{,22}) \quad \gamma_2 = \psi_{,12} = \psi_{,21}\,. \tag{1.28}$$

Hence,

$$A(\boldsymbol{\theta}) = \begin{pmatrix} 1 - \kappa - \gamma_1 & -\gamma_2 \\ -\gamma_2 & 1 - \kappa + \gamma_1 \end{pmatrix} = (1-\kappa)\mathbb{1} - |\gamma| \begin{pmatrix} \cos 2\omega & \sin 2\omega \\ \sin 2\omega & -\cos 2\omega \end{pmatrix}. \tag{1.29}$$

From Eq. (1.29) we notice that, to first order, the deflection can be seen as the superposition of two effects. The convergence describes a global isotropic magnification (or demagnification), i.e., images appear larger or smaller than the source, whereas the shear introduces an anisotropic distortion along a privileged axis. More in detail, the amplitude and the phase of the shear represent the degree and the direction of distortion of the image. Furthermore, if we consider a Cartesian frame of reference, and a small circular source centred on the origin, then γ_1 is responsible for the distortion along the coordinate axes, while γ_2 along the bisectors. Images are thus distorted in shape and size: Figure 1.2 describes schematically the distortion effects induced by the convergence and the shear on a circular source.

From Eq. (1.29), we can read off the eigenvalues $\lambda_{1,2}$ of the Jacobian matrix, its determinant, and its trace,

$$\lambda_{1,2} = 1 - \kappa(\boldsymbol{\theta}) \pm |\gamma(\boldsymbol{\theta})|\,, \tag{1.30}$$

$$\det A(\boldsymbol{\theta}) = [1 - \kappa(\boldsymbol{\theta})]^2 - |\gamma|^2(\boldsymbol{\theta})\,, \tag{1.31}$$

and

$$\mathrm{tr} A(\boldsymbol{\theta}) = 2[1 - \kappa(\boldsymbol{\theta})]\,. \tag{1.32}$$

More specifically, the eigenvalue $\lambda_1 = \lambda_t = 1 - \kappa(\boldsymbol{\theta}) - |\gamma(\boldsymbol{\theta})|$ is called *tangential* eigenvalue, and represents the amplification along the tangential direction. Complementarily, $\lambda_2 = \lambda_r = 1 - \kappa(\boldsymbol{\theta}) + |\gamma(\boldsymbol{\theta})|$ is called *radial* eigenvalue, and quantifies the distortion along the radial direction.

The absence of emission and absorption of photons in GL and the Poincaré integral invariant imply that lensing conserves surface brightness. The surface brightness distribution $I^{(\mathrm{s})}$ of a point-like source on the source plane is equal to the observed surface

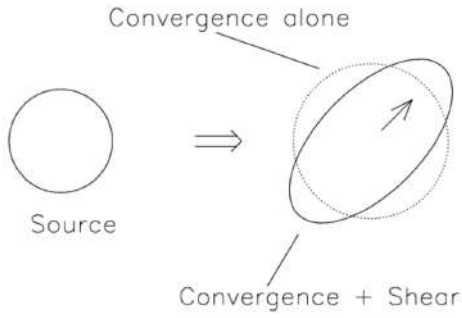

Figure 1.2: Distortion effects due to convergence and shear on a circular source. Credits: Meneghetti (2022).

brightness distribution I of the image on the lens plane: $I(\boldsymbol{\theta}) = I^{(\mathrm{s})}[\boldsymbol{\beta}(\boldsymbol{\theta})]$. The ratio between the corresponding observed and unlensed flux is the *magnification*, which describes how brighter (and bigger) the images appear with respect to the relative source. If we apply the linearization of the ray-tracing equation introduced above, it can be found that

$$|\mu(\boldsymbol{\theta})| = \frac{1}{|\det A(\boldsymbol{\theta})|} = \frac{1}{|[1-\kappa(\boldsymbol{\theta})]^2 - |\gamma|^2(\boldsymbol{\theta})|}\,. \tag{1.33}$$

Here, $\mu(\boldsymbol{\theta})$ is called magnification factor, or, simply, magnification. Its sign is called parity of the image, and determines its orientation relative to the unperturbed image. An image with positive parity maintains the same orientation of the source (the parity is said to be conserved), whereas an image with negative parity is subject to a mirror-symmetric transformation.

1.4 Classification of multiple images

The deflection of light rays causes a delay in the time between the emission of radiation by the source and the signal reception by the observer along a path γ, as given by Eq. 1.4. Having introduced the deflection potential ψ, we may rewrite the expression for the travel time as

$$c\Delta t = \int_\gamma n\,\mathrm{d}l = |\gamma| + \frac{2}{c^2}\int_\gamma |\phi(\boldsymbol{\theta})|\,\mathrm{d}l = |\gamma| + \frac{D_\mathrm{d} D_\mathrm{s}}{D_\mathrm{ds}}\psi(\boldsymbol{\theta})\,. \tag{1.34}$$

This expression (valid for a single-plane lens) can therefore be considered as the sum of two terms: a geometrical and a gravitational factors. The geometrical term $|\gamma|$ is due to

the actual length of the path. The deflection causes a light ray to be bent, and curved rays are geometrically longer than straight rays. It can be shown that this factor depends on the distance between the lens and the source (Schneider et al. 1992). The gravitational factor $\propto \psi(\boldsymbol{\theta})$ is instead associated with the GR effect of time dilatation. As stated above, the mass distribution acts as a lens with an effective refraction index greater than the unity, therefore light rays are slowed down. This latter term is also called *Shapiro* time delay (Shapiro 1964). We can properly combine the two factors and obtain the total time delay introduced by GL (Schneider 1985; Blandford & Narayan 1986) at a given position $\boldsymbol{\theta}$ on the lens plane,

$$\begin{aligned} c\Delta t &= (1+z_{\rm d})\frac{D_{\rm d}D_{\rm s}}{D_{\rm ds}}\left\{\frac{1}{2}|\boldsymbol{\theta}-\boldsymbol{\beta}|^2-\psi(\boldsymbol{\theta})\right\}+k(\boldsymbol{\beta})= \\ &= (1+z_{\rm d})\frac{D_{\rm d}D_{\rm s}}{D_{\rm ds}}\varphi(\boldsymbol{\theta},\boldsymbol{\beta})+k(\boldsymbol{\beta})\,, \end{aligned} \tag{1.35}$$

where

$$\varphi(\boldsymbol{\theta},\boldsymbol{\beta})=\frac{1}{2}|\boldsymbol{\theta}-\boldsymbol{\beta}|^2-\psi(\boldsymbol{\theta})\,. \tag{1.36}$$

is called *Fermat potential*, and $k(\boldsymbol{\beta})$ is an addictive function depending only on the position of the source. Through the deflection potential, we can rewrite the ray-tracing equation (once again, in case of a single-plane lens) as

$$(\boldsymbol{\theta}-\boldsymbol{\beta})-\nabla\psi(\boldsymbol{\theta})=\nabla\left\{\frac{1}{2}|\boldsymbol{\theta}-\boldsymbol{\beta}|^2-\psi(\boldsymbol{\theta})\right\}=\nabla\varphi(\boldsymbol{\theta},\boldsymbol{\beta})=0\,. \tag{1.37}$$

Eq. (1.35) and Eq. (1.37) imply that $\nabla\Delta t(\boldsymbol{\theta},\boldsymbol{\beta})=0$, hence, images satisfy the Fermat principle. Images occur at the stationary points of the time delay surface given by Eq. (1.35), i.e., maxima, minima, or saddle points. The Hessian matrix of this surface is

$$T_{ij}=\frac{\partial^2\Delta t(\boldsymbol{\theta})}{\partial\theta_i\partial\theta_j}\propto\delta_{ij}-\frac{\partial^2\psi}{\partial\theta_j\partial\theta_i}(\boldsymbol{\theta})=A_{ij}\,, \tag{1.38}$$

namely it is proportional to the Jacobian matrix. We can then classify the multiple images into these following categories.

Type I images. If both the eigenvalues of the Jacobian matrix (Eq. 1.30) are positive, then its determinant and its trace are positive. This implies that the magnification factor is positive, hence parity is conserved. These images are minima of the Fermat potential.

Type II images. If $\lambda_1\lambda_2<0$, then the determinant of the Jacobian matrix is negative, but the sign of its trace cannot be determined a priori. The magnification factor is always negative, hence parity is not conserved. These images are saddle points of the Fermat potential.

Type III images. If both the eigenvalues of the Jacobian matrix are negative, then its determinant is positive, and the trace is negative. Hence, the magnification factor is positive, implying that parity is conserved. These images are maxima of the Fermat potential.

It can be shown (Burke 1981; McKenzie 1985) that, under the assumption that $\kappa(\boldsymbol{\theta})$ is a smooth function which decreases faster than $\boldsymbol{\theta}^{-2}$ for $\boldsymbol{\theta}\to\infty$, the number of positive-parity images (i.e., Type I and/or III) exceeds that of negative parity images (Type II) by

one, and the total number of images is odd (*odd number* theorem). It can also be demonstrated, under the same hypothesis, that the image of a source which first arrives to an observer is of Type I, and this is brighter than (or as bright as) the source would appear in the absence of the lens (Schneider 1984).

We conclude this section by giving two conditions such that a matter distribution (under the same assumptions stated before) can produce multiple images of the source:

Condition I. An isolated lens can produce multiple images of a source if, and only if, it exists a point $\boldsymbol{\theta}$ such that $\det A(\boldsymbol{\theta}) < 0$. If $\det A(\boldsymbol{\theta}) > 0 \, \forall \boldsymbol{\theta}$, then the lens mapping would be globally invertible, and could not cause multiple images. On the other hand, if a source has an image observed at a point $\boldsymbol{\theta}_0$ such that $\det A(\boldsymbol{\theta}_0) < 0$, then such image would be a saddle point of the Fermat potential. Since the potential has always a minimum and the total number of images must be odd, there must exist two more images of the same source.

Condition II. A sufficient but not necessary condition for the possible production of multiple images is that there exists a point $\boldsymbol{\theta}$ such that $\kappa(\boldsymbol{\theta}) > 1$. Indeed, if a source has an image observed at a point $\boldsymbol{\theta}_0$ such that $\kappa(\boldsymbol{\theta}_0) > 1$, then it cannot be a minimum of the Fermat potential. In fact, the trace of the Jacobian matrix is positive in case of a minimum of the Fermat potential, which requires the convergence to be less than unity, Again, since this potential has always a minimum and the total number of images must be odd, there must exist at least two more images of the same source.

1.5 Critical lines and caustics

The closed lines on the lens plane where the determinant of the Jacobian matrix A annuls are called *critical* curves. Since $\det A(\boldsymbol{\theta}) = 0$ for the points $\boldsymbol{\theta}$ belonging to a critical curve, for such points the lens mapping is not locally invertible. Additionally, the determinant depends on the convergence and thus on the critical surface mass density and the distances between source, lens and observer. Hence the position of the critical lines changes as the redshift of the source varies. Furthermore, given Eq. (1.33), the magnification formally diverges: $\mu \to \infty$, i.e. point-like images located on critical lines are amplified to infinity and appear infinitely brighter than the corresponding unlensed source. In reality, the total observed flux is always finite for extended astrophysical sources: we have to consider the source as an extended distribution, and therefore the magnification has to be weighted all over the source profile.

The determinant of the Jacobian matrix can be interpreted as the product of its eigenvalues: the equation of the critical curves can then be obtained by imposing $\lambda_{r,t} = 0$. The curve associated with $\lambda_t = 0$ is called tangential critical curve: an image forming along it is strongly distorted tangentially to this line. Similarly, the curve associated with $\lambda_r = 0$ is called radial critical curve: an image forming along it is strongly distorted perpendicular to this line. When crossing a critical curve, at least one of the eigenvalues of the Jacobian matrix changes sign: therefore, these curves divide the lens plane into regions where maxima, minima, or saddle points of the Fermat potential occur.

The curves corresponding to the critical lines on the source plane, which can be evaluated through the ray tracing equation, are known as *caustics*. Differently from the critical lines, caustics are not smooth, and often show an asteroidal shape made up of cusps and folds. They separate regions on the source plane characterised by different image multiplicities: if a source crosses a caustic, the number of images predicted changes by ± 2

(see Sect. 1.4), i.e., a change in the source position leads to a variation of the number of images. Shortly before their fusion (or creation), the images appear very bright because they are in the vicinity of the corresponding critical curve on the lens plane. The position of the source relative to a caustic allows us to understand which type of image will be formed. Generally two caustics are formed, relative to the radial and the tangential critical curves: if a source is located outside both caustics, then at least one image will be formed, outside both critical curves on the lens plane, and it will be a minimum of the Fermat potential, with both eigenvalues of the lensing Jacobian positive. If the source is located between the caustics, then an additional image will be formed between the two critical curves: since at least one eigenvalue of the Jacobian vanishes when crossing a critical curve, then the image will be a saddle point. Finally, if the source lies inside the innermost caustic, another image will be formed inside the innermost critical curve: the second eigenvalue has changed sign, thus both of them are negative, and the image is a maximum of the Fermat potential.

1.6 Multiple light deflection

There may be situations where the light rays emitted by an astronomical source are deflected multiple times on the way to the observer. For example, the light emitted by a distant quasar may be deflected by two galaxies lying at different redshifts. If the separation between the two lenses is sufficiently small, then the two deflectors will act as if they were a single geometrically thin lens, and the single lens-plane theory applies. On the other hand, if the separation is sufficiently large, then a light ray is deflected by each lens independently, namely the deflection induced by one lens is not influenced by the other one. Here, we will briefly recall the principles of the multiple lens-plane theory, following Blandford & Narayan (1986), Kovner (1987), and Schneider et al. (1992). The assumption regarding the validity of the multi lens-plane theory is that the light ray, after being deflected by one matter distribution, is well within the asymptotic regime before being deflected by another mass component.

Suppose we have N matter distributions having total surface mass densities Σ_i, and lying at redshifts z_i (with $i = 1, 2, \ldots, N$), ordered such that $i < j$ ($z_i < z_j$). Let us consider a source at $z_\mathrm{s} > z_N$. The ray-tracing equation is

$$\boldsymbol{\eta} = \frac{D_\mathrm{s}}{D_1}\boldsymbol{\xi}_1 - \sum_{i=1}^{N} D_{i\mathrm{s}}\hat{\boldsymbol{\alpha}}(\boldsymbol{\xi}_i)\,, \tag{1.39}$$

where $\boldsymbol{\eta}$ and $\boldsymbol{\xi}_i$ represent the position vectors on the source plane and on the ith lens plane, respectively, and $\hat{\boldsymbol{\alpha}}(\boldsymbol{\xi_i})$ is the deflection angle of a light ray when it crosses the ith lens plane in $\boldsymbol{\xi_i}$. The impact vectors $\boldsymbol{\xi}_i$ can be derived recursively through

$$\boldsymbol{\xi}_j = \frac{D_j}{D_1}\boldsymbol{\xi}_1 - \sum_{i=1}^{j-1} D_{ij}\hat{\boldsymbol{\alpha}}(\boldsymbol{\xi}_i)\,. \tag{1.40}$$

Here, $D_{ij} = D(z_i, z_j)$ is the angular diameter distance of the jth plane from the ith plane, and $D_i = D(0, z_i) = D(z_i)$ is the distance of the ith plane from the observer. Eq. (1.40) can be rewritten as a function of the angular variables $\boldsymbol{\theta}_i = \boldsymbol{\xi}_i/D_i$ as

$$\boldsymbol{\theta}_j = \boldsymbol{\theta}_i - \sum_{i=1}^{j-1} \frac{D_{ij}}{D_1}\hat{\boldsymbol{\alpha}}_i(D_i\boldsymbol{\theta}_i)\,. \tag{1.41}$$

The deflection angles can be derived from the total surface mass densities as in Eq. (1.17). We define the dimensionless surface mass densities κ_i as

$$\kappa_i(\boldsymbol{\theta}_i) = \frac{4\pi G}{c^2}\frac{D_i D_{i\mathrm{s}}}{D_{\mathrm{s}}}\Sigma_i(D_i\boldsymbol{\theta}_i)\,, \tag{1.42}$$

and the deflection potentials as

$$\psi_i(\boldsymbol{\theta}_i) = \frac{1}{\pi}\int \mathrm{d}^2\theta' \kappa_i(\boldsymbol{\theta}')\ln|\boldsymbol{\theta}_i - \boldsymbol{\theta}'|\,, \tag{1.43}$$

such that $\boldsymbol{\alpha}_i = \nabla\psi_i$ and $\boldsymbol{\alpha}_i = D_{i\mathrm{s}}/D_{\mathrm{s}}\hat{\boldsymbol{\alpha}}_i$. We can finally express Eq. (1.41) as a function of the scaled deflection angles as

$$\boldsymbol{\theta}_j = \boldsymbol{\theta}_1 - \sum_{i=1}^{j-1} d_{ij}\boldsymbol{\alpha}_i(\boldsymbol{\theta}_i)\,, \tag{1.44}$$

with

$$d_{ij} = \frac{D_{ij}D_{\mathrm{s}}}{D_j D_{i\mathrm{s}}}\,. \tag{1.45}$$

In particular, $d_{i\mathrm{s}} = 1$. So, for $j = N+1 = \mathrm{s}$, Eq. (1.44) reduces to

$$\boldsymbol{\beta} = \boldsymbol{\theta}_{N+1} = \boldsymbol{\theta}_1 - \sum_{i=1}^{N}\boldsymbol{\alpha}_i(\boldsymbol{\theta}_i)\,. \tag{1.46}$$

The previous equations describe the impact parameters of a light ray in the different lens planes as a function of $\boldsymbol{\theta}_1$, which is the angular position of an image on the observer's sky, hence it is an independent variable.

CHAPTER 2

Galaxy clusters

Galaxies are not distributed uniformly in the Universe, but instead show the tendency to form overdense regions called groups or clusters of galaxies (Geller & Huchra 1989; Colless et al. 2001; Zehavi et al. 2011). According to the currently accepted paradigm of structure formation, these objects are thought to form through a hierarchical sequence of mergers and accretion of smaller-scale systems driven by gravity (see, e.g., Kravtsov & Borgani 2012, for a review). Galaxy clusters are the most massive gravitationally-bound structures in the Universe, composed of hundreds to thousands of galaxies, with typical total masses in the range $10^{14} - 10^{15} M_{\odot}$ and typical sizes in the range $1 - 2$ Mpc (Schneider 2006).

2.1 Mass components of galaxy clusters

During the 1930s, it was realized that stars visible in galaxies contribute up to $\sim 5\%$ to the total mass of a cluster of galaxy. This issue was initially pointed out by Frank Zwicky. He registered a large dispersion in the apparent velocities of 8 galaxies belonging to the Coma cluster, with differences higher than 2000 km/s (Zwicky 1933). When applying the virial theorem (see below, Sect. 2.3.1) to measure the total mass of the system, he found a discrepancy of a factor ~ 10 with the value obtained by adding the contribute of the single galaxies (i.e., their optical stellar content), thus concluding that galaxy clusters must contain more mass than is visible in galaxies – the so-called *missing mass* problem.

2.1.1 Hot gas in galaxy clusters

A step forward was made with the advent of X-ray astronomy: in the 1970s, an extended X-ray emission from galaxy clusters was detected (Cavaliere et al. 1971; Giacconi et al. 1972; Forman et al. 1978). Indeed, the space between member galaxies is permeated by a hot gas component, the so-called intracluster medium (ICM), which extends up to few Mpc from the cluster core (for a review see, e.g., Kravtsov & Borgani 2012; Vikhlinin et al. 2014; Walker et al. 2019). The ICM has typical temperatures $T \sim 10^7 - 10^8$ K ($1 - 10$ keV), and characteristic luminosities $L_X \sim 10^{43} - 10^{45}$ erg/s, which make them the brightest extragalactic X-ray sources in the Universe beside the Active Galactic Nuclei (AGN). The emission is mainly due to thermal bremsstrahlung (or free-free emission): the radiation is produced by the acceleration of electrons in the electric field of protons and atomic nuclei. It is by studying the properties of this radiation that the gas temperature of galaxy clusters may be estimated. The emissivity of bremssthralung (except for a quantum

mechanical correction factor of the order of unity) is described by

$$\epsilon_\nu^{\rm ff} \sim \frac{32\pi Z^2 e^6 n_{\rm e} n_{\rm i}}{3 m_{\rm e} c^2} \sqrt{\frac{2\pi}{3 k_{\rm B} T m_{\rm e}}} \exp\left\{-\frac{h\nu}{k_{\rm B} T}\right\}, \tag{2.1}$$

where e is the elementary charge, $n_{\rm e}$ ($n_{\rm i}$) the number density of electrons (ions), Ze the charge of the ions, and $m_{\rm e}$ the electron mass. Since the plasma is approximately uncharged, $n_{\rm e} \sim n_{\rm i} \sim n$, with n the global number density. Hence, $\epsilon_\nu^{\rm ff} \propto n^2$.

Apart from the free-free emission, the X-ray spectra of low-temperature galaxy clusters show emission lines, e.g. the Lyman-α ("Kα") line of the 25-fold ionised iron at ~ 6.7 keV. These lines tend to become less important with increasing temperature, since more atoms get fully ionised and thus the line emission becomes weaker.

2.1.2 Dark matter

The ICM represents the main baryonic component of a cluster, being responsible for $\sim 12 - 15\%$ of its total mass. The remaining $\sim 80\%$ is in the form of a non-baryonic matter component, called dark matter (DM), an idea that first emerged in the 1930s when Zwicky refined his mass estimate of the Coma cluster (Zwicky 1937a) and, contemporarily, Sinclair Smith measured the mass of the Virgo cluster (Smith 1936) through a similar method. Since then, galaxy clusters have become the ideal playground to test, compare, and put constraints on different DM theories, being its gravitational potential mainly dominated by this unseen component, as well as to examine theories alternative to DM. A notable example is represented by the *Bullet cluster* (see Fig. 2.1), a system composed of two clusters having recently collided. Indeed, if the discrepancy between the the observed mass in clusters (in the form of stars and ICM) and the total one deduced from dynamical methods (or lensing) was due to a modification in the law of gravity on large scales then the bulk of the mass of the cluster has to be centered on its X-ray emitting gas. On the other hand, if the disagreement was due to the presence of DM, then DM should behave similarly to galaxies, and, if it was collisionless, as the currently accepted paradigm supports, the DM components of both merging systems simply run through each other. The studies by Markevitch et al. (2002) and Clowe et al. (2006) showed that the mass of the system is centered on the galaxy distributions of the two clusters, and clearly displaced from the X-ray emitting gas. Hence, the mass discrepancy cannot be explained with a modification of the laws of gravity.

2.2 Catalogs of galaxy clusters

Historically, galaxy clusters were first identified as galaxy over-densities. The first catalogue of galaxy clusters was compiled in 1958 by George Abell (Abell 1958), who registered regions in the sky showing an over-density of galaxies. He defined clusters those over-densities of $N > 50$ galaxies with apparent magnitude m in the interval $m_3 \leq m \leq m_3 + 2$, with m_3 the apparent magnitude of the third brightest galaxy of the cluster. He also required clusters to lie within a circle of angular radius $\theta_{\rm A} = 1.7'/z$, with z the estimated redshift of the cluster, which had to be in the range $0.02 \leq z \leq 0.2$. $\theta_{\rm A}$ is called Abell radius, and corresponds to a physical scale of $R_{\rm A} \sim 1.5\,{\rm Mpc}$. Adopting these criteria, ~ 1700 over-densities were classified as clusters. Abell performed his identification by eye on photoplates from the Palomar Observatory Sky Survey (POSS), a photographic atlas of the Northern sky. Following the same procedure, an extension of the Abell catalogue to the Southern sky was published in 1989 by Abell, Corwin,

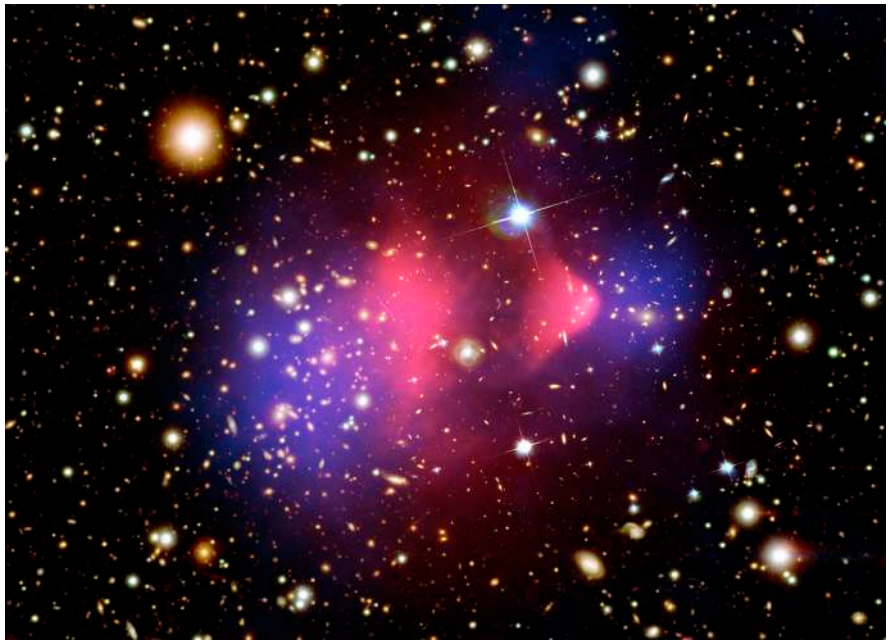

Figure 2.1: The galaxy cluster 1E0657-56, also known as the *Bullet cluster*. The X-ray emission of the ICM of the cluster as detected with the *Chandra* telescope is shown in *red* overlaid over the optical rgb-composite HST image. *Violet* areas are derived using weak lensing and highlight the total mass distribution, i.e. the DM content. Credit: X-ray map: NASA/CXC/CfA/M. Markevitch; Optical and lensing map: NASA/STScI, Magellan/U. of Arizona/D. Clowe; Lensing map: ESO WFI. Clowe et al. (2006).

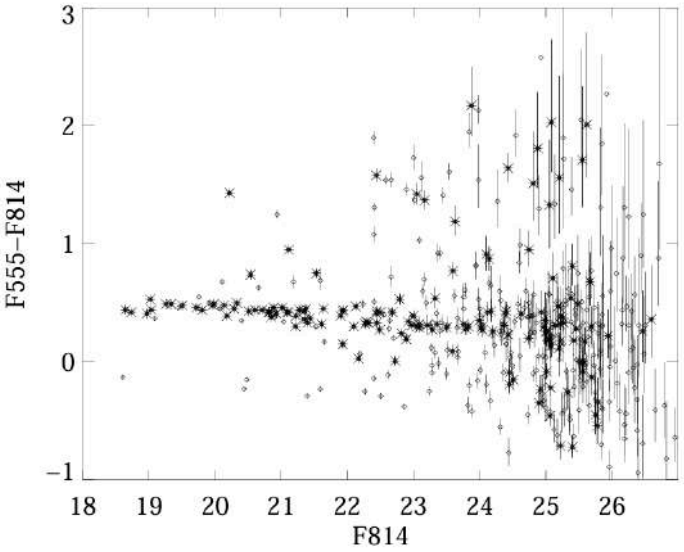

Figure 2.2: Colour-magnitude diagram of the galaxy cluster Abell 2390, observed with the HST. The data are from Gladders et al. (1998). The asterisks indicate galaxies morphologically selected as elliptical, and diamonds indicate other galaxies in the field. Credits: Gladders & Yee (2000).

and Olowin (Abell et al. 1989), which increased the number of clusters up to ~ 4000. Similarly, Zwicky et al. (1961, 1968) presented another catalogue of galaxy clusters, considered less reliable than the others due to the presence of more spurious candidates. The selection of galaxy clusters through optical search suffers from several problems, including random over-densities caused by line-of-sight projection being erroneously classified as clusters, and the subjectivity in the visual inspection of photoplates.

Nowadays, these issues have been overcome: all processes are digitalized, and other criteria are adopted to discriminate galaxy clusters from random fluctuations. One method that is adopted is based on the colours of early-type (elliptical) galaxies. Indeed, elliptical galaxies have rather uniform colours, due to the fact that they are mainly composed of an old red stellar population, with essentially no (or little) star formation. Hence, when plotting the colours of the early-type galaxies of a galaxy cluster as a function of their magnitude, they tend to lie along a rather horizontal straight line, called red cluster sequence (RCS), of which an example is shown in Fig 2.2. The scatter of elliptical galaxies around the RCS is typically small, and possible slopes can be attributed to the fact that more massive ellipticals have higher metallicity, resulting in redder colours. The RCS methodology was used in several multi-band imaging surveys to detect galaxy clusters, including the RCS survey (Gladders 2000) with the Canada France Hawaii Telescope (CFHT). This survey targeted $100\,\mathrm{deg}^2$ with two filters, providing more than 1000 cluster candidates in the redshift range $0.1 \leq z \leq 1.4$. This survey was complemented with the RCS-II survey (Gilbank et al. 2011), which observed $100\,\mathrm{deg}^2$ with three filters from the CFHT, yielding $\sim 10^4$ cluster candidates up to $z \sim 1$.

Today, we can now rely on catalogues of galaxies based on ground-based large spectroscopic surveys, including the Sloan Digital Sky Survey (SDSS, York et al. 2000), and,

more recently, the Dark Energy Survey (DESI, DESI Collaboration et al. 2016). In addition, the European Space Agency (ESA) satellite *Euclid*(Euclid Collaboration: Scaramella et al. 2022; Euclid Collaboration: Mellier et al. 2024) is expected to drastically increase the number of galaxies with available spectroscopic measurements (up to redshift ~ 2).

An alternative and more reliable way of selecting galaxy clusters with respect to optical surveys is given by their X-ray emission. First, the X-ray signal allows to probe higher redshift. Secondly, since the X-ray emissivity is proportional to the square of the particle density, a X-ray peak reflects a deep potential well (hence projection effects are, in principle, negligible). X-ray surveys have thus been an alternative to optical ones to look for clusters. The very first X-ray catalogue of clusters was obtained within the Extended Medium Sensitivity Survey (EMSS, Gioia et al. 1990), containing 104 clusters identified from archival images obtained with the *Einstein* observatory, followed by the ROSAT All-Sky-Survey (RASS, Trümper 1984; Ebeling et al. 1998), containing about 10^5 entries.

2.3 Methods to measure the total mass of galaxy clusters

2.3.1 Dynamical mass of clusters

This sub-section is based on Girardi et al. (1998), Biviano (2000), and Mamon et al. (2013). Given the Abell radius $R_{\rm A}$ introduced in the previous Section, we may define a dynamical time-scale $t_{\rm dyn}$ of a cluster as the time a typical galaxy with velocity equal to the one-dimensional velocity dispersion σ_v requires to cross the cluster,

$$t_{\rm dyn} = \frac{R_{\rm A}}{\sigma_v} \sim 1.5\,{\rm Gyr}\,, \tag{2.2}$$

where $\sigma_v \simeq 10^3\,{\rm km/s}$ has been assumed as a typical value (Schneider 2006) and $R_{\rm A} \simeq 1.5\,{\rm Mpc}$ as above. This time-scale is much smaller than the age of the Universe which can be roughly estimated from the inverse of the Hubble constant, $H_0^{-1} \simeq 14\,{\rm Gyr}$. If we assume the virial equilibrium, then the following relation holds,

$$2K + U = 0\,, \tag{2.3}$$

with K and U the total kinetic and potential energy of the cluster galaxies, respectively. If we assume that the total mass distribution of a cluster follows the galaxies distribution, then we may associate to each galaxy a *representative* mass. Given this, we express K and U as

$$K = \frac{1}{2}\sum_{i=1}^{N} m_i v_i^2 \quad \text{and} \quad U = -\frac{1}{2}\sum_{i\neq j} \frac{G m_i m_j}{r_{ij}}\,, \tag{2.4}$$

where m_i denotes the total mass of the ith representative mass element, v_i its velocity, and r_{ij} the distance between the ith and jth mass elements. Given $M = \sum_i m_i$ the total mass, we define the three-dimensional velocity dispersion $\langle v^2 \rangle$, weighted by the mass, as

$$\langle v^2 \rangle = \frac{1}{M}\sum_i m_i v_i^2\,, \tag{2.5}$$

and the gravitational radius r_G as

$$r_G = 2M^2 \left[\sum_{i \neq j} \frac{m_i m_j}{r_{ij}} \right]^{-1} . \tag{2.6}$$

Thus,

$$K = \frac{1}{2} M \langle v^2 \rangle \quad \text{and} \quad U = -\frac{GM^2}{r_G} , \tag{2.7}$$

and, by applying the virial theorem Eq. (2.3),

$$M = \frac{r_G \langle v^2 \rangle}{G} . \tag{2.8}$$

In Eq. (2.6), the virial radius is evaluated starting from the three-dimensional distances r_{ij}, which are not direct observables. Thus, it is necessary to express M in terms of projected quantities. In case the velocity vectors of the representative masses are not correlated and randomly oriented, e.g. as for an isotropic velocity distribution, then $\langle v^2 \rangle = 3\sigma_v^2$, with σ_v the velocity dispersion of galaxies along the line of sight. Furthermore, we can define the projected gravitational radius R_G as

$$R_G = 2M^2 \left[\sum_{i \neq j} \frac{m_i m_j}{R_{ij}} \right]^{-1} , \tag{2.9}$$

with R_{ij} the projected distance between the ith and the jth masses. In case of a spherical mass distribution, $r_G = R_G \, \pi/2$, hence,

$$M = \frac{3\pi \, R_G \, \sigma_v^2}{2G} \simeq 1.1 \times 10^{15} \, M_\odot \left(\frac{\sigma_v}{10^3 \, \mathrm{km/s}} \right)^2 \left(\frac{R_G}{1 \, \mathrm{Mpc}} \right) , \tag{2.10}$$

where typical values for clusters of galaxies have been applied. When compared with the total optical luminosity of cluster galaxies, $L \sim 10^{12} - 10^{13} \, L_\odot$, one finds as total mass-to-light ratio a value of $M/L \simeq 300 M_\odot/L_\odot$, which is by far larger than typical values for early-type galaxies by at least a factor 10.

2.3.2 X-ray based mass of clusters

This sub-section is based on Schneider (2006), Ettori et al. (2019), and Ettori & Eckert (2022). We can derive an estimate of the mass of a galaxy cluster based on the X-ray luminosity of the ICM. If we denote with P the gas pressure, ρ_g its mass density, and n_g its number density, then we can introduce the sound-crossing time t_sc as

$$t_\mathrm{sc} \simeq 2 \, \frac{R_\mathrm{A}}{c_\mathrm{s}} , \tag{2.11}$$

with R_A the Abell radius and c_s the speed of sound in the ICM. For a cluster with temperature $T \sim 10^8$ K, we have $t_\mathrm{sc} \sim 7 \times 10^8$ years, which is much shorter than the estimate of the age of the Universe made before. We can thus safely assume the gas to be in hydrostatic equilibrium. We can then apply

$$\nabla P = -\rho_\mathrm{g} \nabla \phi , \tag{2.12}$$

where ϕ is the total gravitational potential of the cluster. If we assume spherical symmetry, then the previous equation reduces to

$$\frac{1}{\rho_{\rm g}}\frac{{\rm d}P}{{\rm d}r} = -\frac{{\rm d}\phi}{{\rm d}r} = -\frac{GM(r)}{r^2}\,, \tag{2.13}$$

with $M(r)$ the total mass enclosed within a sphere of radius r. We can express the pressure of the gas as

$$P = n_{\rm g}k_{\rm b}T = \frac{\rho_{\rm g}k_{\rm b}T}{\mu m_{\rm p}}\,, \tag{2.14}$$

where $k_{\rm b}$ is the Boltzmann constant, $m_{\rm p}$ is the proton mass, and μ is the average molecular mass, defined as the average mass of a gas particle of mass m in units of the proton mass, $\mu = \langle m\rangle/m_{\rm p}$. Finally, we can recover the total mass profile of the cluster as a function of the radial profiles of its gas density and temperature,

$$M(r) = -\frac{k_{\rm b}Tr^2}{G\mu m_{\rm p}}\left(\frac{{\rm d}\ln\rho_{\rm g}}{{\rm d}r} + \frac{{\rm d}\ln T}{{\rm d}r}\right)\,. \tag{2.15}$$

However, $\rho_{\rm g}(r)$ and $T(r)$ cannot be directly measured: they are extracted from the X-ray luminosity and spectral energy distribution, which are observed only in projection. In addition, before the launch of XMM-*Newton* and Chandra, the angular and energy resolution of previous X-ray telescopes were not high enough to enable precise measurements of $\rho_{\rm g}(r)$ and $T(r)$. Further simplifying assumptions were then required to determine the mass of a cluster.

2.4 Galaxy clusters as gravitational lenses

Galaxy clusters are the most massive structures in the Universe and, as observed, they are the largest repositories of DM. As a result, they are some of the most efficient gravitational lenses known to date. Once again, it was Zwicky (1937b) who first addressed the possibility of exploiting GL by galaxy clusters as a valuable tool to measure the amount of this unseen mass component and study distant, magnified objects lying behind clusters. Nevertheless, the lack of appropriate resolution and imaging facilities at the time and the inadequacy of a solid theoretical understanding of how structure assembles prevented progress in GL by cluster studies. The first observational detection of a SL event by a galaxy cluster was reported independently by Lynds & Petrosian (1986) and Soucail et al. (1987), a giant arc in the galaxy cluster Abell 370. Initially, different hypotheses on the origin of this arc were formulated, including the emission by shock fronts of the ICM originating from explosive events. This scenario was disproven as the measurement of the redshift of the arc by Soucail et al. (1988) showed that the source was at a redshift higher than that of the cluster: the arc was recognized as a strongly distorted and highly magnified structure given by the merging images of a strongly lensed background galaxy (Paczynski 1987).

With this discovery of giant arcs, the SL regime was established as a property of the deflection produced by dense cluster cores. The unique angular resolution of the Hubble Space Telescope (HST) played a crucial role in revolutionizing SL studies by helping in the discovery of giant arcs in massive clusters. SL features in galaxy clusters are typically observed in the inner one arcminute central region (inner $\sim$ hundreds of kpc), where the density is sufficiently higher than the critical density. The James Webb Space Telescope (JWST), launched in late 2021, is providing images of unprecedented resolution, thus paving the way to a further revolution in the field of SL.

2.4.1 Mapping dark matter

The central core of galaxy clusters (few hundreds of kpc from their centres) is the region where SL features are observed, namely multiple images and giant arcs, being characterized by an elevated concentration of matter (both baryonic and DM). SL permits the mapping of the detailed two-dimensional total mass distribution of galaxy clusters, and also allows to recover their projected total mass profile. Differently from other galaxy cluster mass probes (dynamics- and X-ray based), GL does not require any hypotheses on the dynamical state of the cluster, hence enabling the study of merging and out-of-equilibrium clusters as well. Once the baryonic mass components have been properly independently mapped, it is possible to infer the DM-only mass distribution (see, e.g. Grillo et al. 2015; Bonamigo et al. 2018; Annunziatella et al. 2017; Granata et al. 2022; Meneghetti et al. 2017, 2020, 2022, 2023) and measure the inner slope of the associated density profile. This quantity is of extreme importance. Indeed, according to the currently accepted cosmological paradigm, DM is believed to be cold and collisionless, interacting only gravitationally with the baryonic components. Cosmological simulations of structure formation over cosmic time suggest that DM settles into a nearly universal density profile (Wang et al. 2020), the Navarro, Frenk, and White profile (NFW, Navarro et al. 1996, 1997), which is thus expected also in galaxy clusters. In presence of further interactions (e.g., self-interaction), or in case DM particles were warm, these additional effects would produce detectable observables in the central dense region (see, e.g., Natarajan et al. 2024, for an overview), which is the one best probed by SL. By combining strong and weak gravitational lensing, using a set of 20 galaxy clusters, Umetsu et al. (2016, 2018) found that the stacked density profile in these systems is very well described by a NFW profile over a wide range of radii (from 30 kpc to 3 Mpc). The density profile on smaller scales (less than ~ 50 kpc) is more difficult to estimate due to the lack of identifiable SL constraints: as a matter of fact, in these regions images are usually de-magnified, and thus harder to detect. Being able to better constrain the mass profile on these scales would further discriminate between alternative DM models.

2.4.2 Cluster lenses as cosmic telescopes

As briefly mentioned in Chapter 1, the magnification that GL by galaxy clusters induces on faint and distant background sources brings them into view, since it increases the flux we receive from them by a factor of tens to hundreds. This effect would not be possible even with the most powerful space telescopes. In addition, GL enlarges (and stretches) the size of these sources, making possible a detailed study of the physical properties of even individual star-forming clumps within them (Johnson et al. 2017; Rigby et al. 2018). Detailed lens models based on deep imaging data are therefore necessary to properly reconstruct the unlensed galaxy morphologies. This feature can be used, in particular, to study star-forming galaxies at the *cosmic noon* ($z \sim 1-3$), an important epoch for the assembly of the massive galaxy population in the Universe, and even more distant galaxies (Acebron et al. 2018; Castellano et al. 2023). Indeed, this is currently being done to study high-z galaxies (see, e.g., Adams et al. 2023).

In addition, the number counts of highly magnified sources obtained from cluster lenses can help in constraining the faint end of the galaxy luminosity function from moderate to high redshifts, which is of crucial importance to extract information about the efficiency of star formation, a piece of information in galaxy evolution that is still missing (Atek et al. 2018; Bouwens et al. 2022).

2.4.3 Cosmology with SL by clusters

In addition, SL can be exploited to probe the geometry and expansion history of the Universe. In the context of SL by galaxy clusters, two main approaches are adopted. On the one hand, measuring the time delays observed in the multiple images of time-varying sources (such as quasars and supernovae) strongly lensed by galaxy clusters can be used to probe constraints on the value of the Hubble constant (Acebron et al. 2023; Bergamini et al. 2024; Grillo et al. 2018, 2020, 2024). These time delays have typical values of several months or years, and can be measured with an approximate precision of 1-3%.

On the other hand, having multiply-imaged sources distributed in redshift helps in measuring the value of key cosmological parameters, thanks to the dependence of the ratios between mutual distances on these values (Acebron et al. 2017; Caminha et al. 2022a; Grillo et al. 2024), among which the matter ($\Omega_{\rm m}$) and dark-energy (Ω_Λ) density parameters, and the dark-energy equation-of state (w) parameter. Cluster strong lensing cosmography has been shown to be competitive with other cosmological probes once systematics are better quantified and controlled (Jullo et al. 2010; Magaña et al. 2018).

2.5 Surveys for cluster lenses

To achieve the aims outlined above, accurate lensing modelling, based on both high-quality imaging, deep photometry, and spectroscopy, is required, and this need has motivated several SL dedicated surveys.

2.5.1 HST lens cluster surveys

HST has devoted significant resources to cluster lensing observations via multiple programs including, CLASH, RELICS, HFF, and BUFFALO. Here we also cite the MACS survey which, despite not being based on HST, facilitated other following surveys.

MACS. The MAssive Cluster Survey (MACS, Ebeling et al. 2001) project aimed at the compilation and characterization of a statistically complete sample of very X-ray luminous, massive, and distant clusters of galaxies. The primary goal of MACS was to increase the number of known massive clusters at $z > 0.3$ from a handful to a hundred. The final MACS cluster sample comprises 124 spectroscopically confirmed clusters at $0.3 < z < 0.7$, of which more than two thirds were new discoveries (Ebeling et al. 2010). To achieve this aim, the survey started from the ROSAT Bright Source Catalogue (Voges et al. 1999), consisting of more than 5,000 X-ray sources, in order to detect distant and massive cluster candidates. Follow-up observations of MACS clusters were launched as the survey proceeded, including images with the HST.

CLASH and CLASH-VLT. The HST Multi-Cycle Treasury program Cluster Lensing And Supernova survey with Hubble (CLASH, Postman et al. 2012) was given 524 orbits of HST time (GO 12066; PI: M. Postman) to observe 25 massive (virial masses $M_{\rm vir} \sim 5 - 30 \times 10^{14} M_\odot$, and X-ray temperatures $T_X \geq 5$ keV) galaxy clusters in the redshift range $z \sim 0.18 - 0.90$. Observations were carried out with 16 broad-band filters, ranging from approximately 200 nm to 1.700 μm, with the Wide Field Camera 3 (WFC3) and the Advanced Camera for Surveys (ACS). The survey was designed to meet different objectives, including the measurement of the total mass profiles of clusters over a wide radial range by combining strong and weak lensing observations, and the study of high-redshift galaxies and their evolution (please refer to Postman et al. 2012, for a more detailed overview).

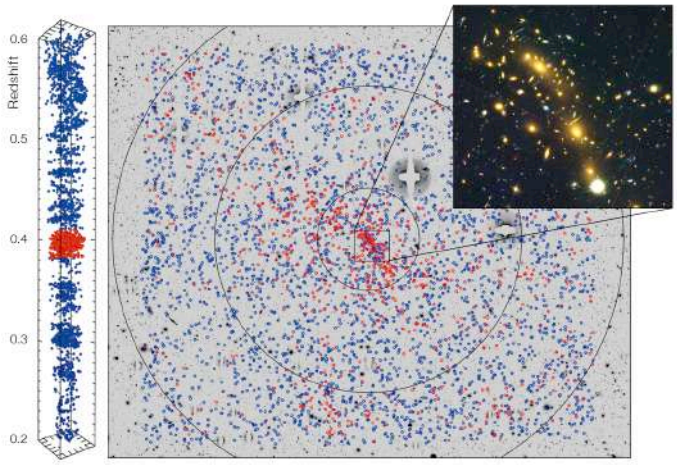

Figure 2.3: Spatial and redshift distribution of the galaxies in the field of view of the galaxy cluster MACS J0416.1−2403 (a HST RGB-composite image is in the top right extract) from CLASH-VLT. The red dots correspond to the spectroscopically confirmed cluster members, whereas the blue ones are foreground and background galaxies. Black circles with 1, 3, and 5 Mpc radii centred on the northern brightest cluster galaxy (BCG) are also indicated. From Rosati et al. (2014).

The survey was complemented by a Large Programme (186.A-0798, PI: P. Rosati; Rosati et al. 2014) which consisted in 225 hours with the Visible Multi Object Spectrograph (VIMOS; Le Fèvre et al. 2003) instrument at the Very Large Telescope (VLT) to perform a panoramic spectroscopic survey of the 13 CLASH clusters visible from ESO-Paranal. For each cluster, this campaign enabled the measurement of the spectroscopic redshifts of ~ 500 cluster members within 3 Mpc from their centres (see, e.g., Fig. 2.3, which refers to the galaxy cluster MACS J0416.1-2403) and for tens to hundreds lensed multiple images inside the HST field of view. The survey allowed for the discovery of new multiple images systems (Coe et al. 2012; Monna et al. 2014; Zitrin et al. 2015; Grillo et al. 2014), the development of robust strong lensing models (Umetsu et al. 2012; Grillo et al. 2015), the study of the kinematics of cluster members (Biviano et al. 2013; Sartoris et al. 2014), and the analysis of the stellar mass functions and stellar mass density profiles (Annunziatella et al. 2014).

HFF. The results from the studies of lensing clusters with HST, including those from CLASH, paved the way to the deeper Hubble Frontier Fields (HFF, Lotz et al. 2017) initiative, that targeted six massive galaxy clusters (Abell 2744, MACS J0416.1−2403, MACS J0717.5+3745, MACS J1149.5+2233, Abell S1063, and Abell 370, see Fig. 2.4), for a total of 140 HST orbits per cluster in 7 broadband filters (up to a 5σ point-source depth of AB magnitude of ~ 29, ~ 1.5 magnitude deeper than CLASH). The project enabled the study of the structure of the DM halos hosting these clusters (Caminha et al. 2016; Bergamini et al. 2019), and the discovery of some of the highest-redshift lensed galaxies. A HST color-composite image of the HFF galaxy cluster MACS J0416−2403 is displayed on the left panel of Fig. 2.5.

RELICS. The Reionization Lensing Cluster Survey (RELICS, P.I.: D. Coe, Coe et al.

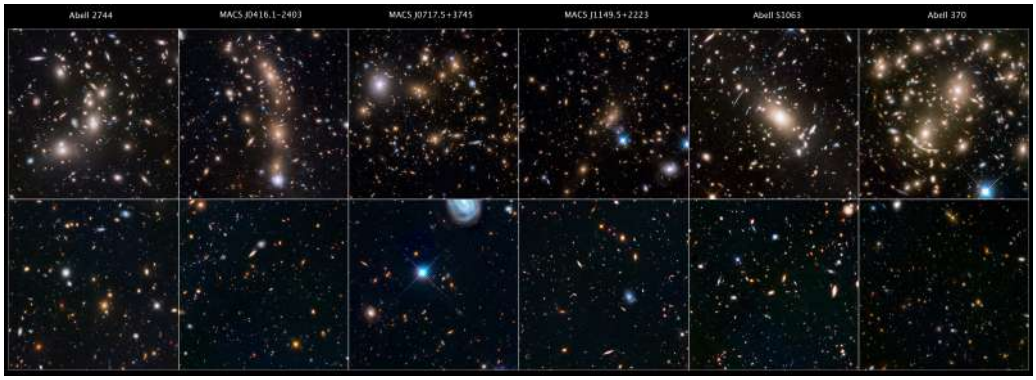

Figure 2.4: RGB images and parallel fields of the six HFF clusters. Credits: NASA, ESA, STScI, and the HFF team.

2019) consisted of 188 orbits of HST time to observe 41 galaxy clusters with 7 broad-band filters using the WFC3 and the ACS. This sample included some of the most massive galaxy clusters, selected on the basis of their mass estimates from the Sunyaev-Zel'dovich effect, spanning the redshift range $z = 0.18 - 0.97$ (see, e.g., Zitrin et al. 2013; Acebron et al. 2019). This project led to the discovery of over 300 $z \sim 6 - 10$ candidates, including the most distant spatially resolved lensed arc known at $z \sim 10$ (Salmon et al. 2018).

BUFFALO. Finally, the Beyond Ultra-deep Frontier Fields and Legacy Observations (BUFFALO, Steinhardt et al. 2020) Program consisted in 101 orbits and 101 parallels as part of the HST Treasury program, which collected data from 2018 to 2020. BUFFALO targeted the six HFF clusters, extending the photometric coverage with additional WFC3 and ACS filters.

2.5.2 JWST lens clusters samples

The unparallel angular resolution in the near-infrared wavelengths of the JWST can be exploited to obtain deeper imaging, thus allowing to produce SL models of unprecedented quality. This has motivated multiple programs of lensing clusters observations with this new facility, including GLASS, PEARLS and UNCOVER.

The The GLASS-JWST Early Release Science (P.I.: T. Treu, Treu et al. 2022) program has obtained the deepest observations of galaxies within all Early Release Science Programs by targeting the HFF lensing cluster Abell 2744, exploiting the NIRISS and NIRSpec instruments to measure the spectroscopic redshifts of the lensed background galaxies. This project paved the way to the next-generation of SL models (Bergamini et al. 2023a).

The Prime Extragalactic Areas for Reionization and Lensing Science (PEARLS, Windhorst et al. 2023) project aims to study the epoch of galaxy assembly, AGN growth, and first light using the JWST. This 110 hour GTO program uses NIRCam to target, among the others, seven SL galaxy clusters and two high redshift proto-clusters. Three lensing clusters (MACS J0416−2403, MACS J1149.5+2223, and Abell 2744), were observed in up to four epochs over a year, to find strongly-lensed high-z supernovae. A JWST color-composite image of the galaxy cluster MACS J0416−2403 is displayed on the right panel of Fig. 2.5.

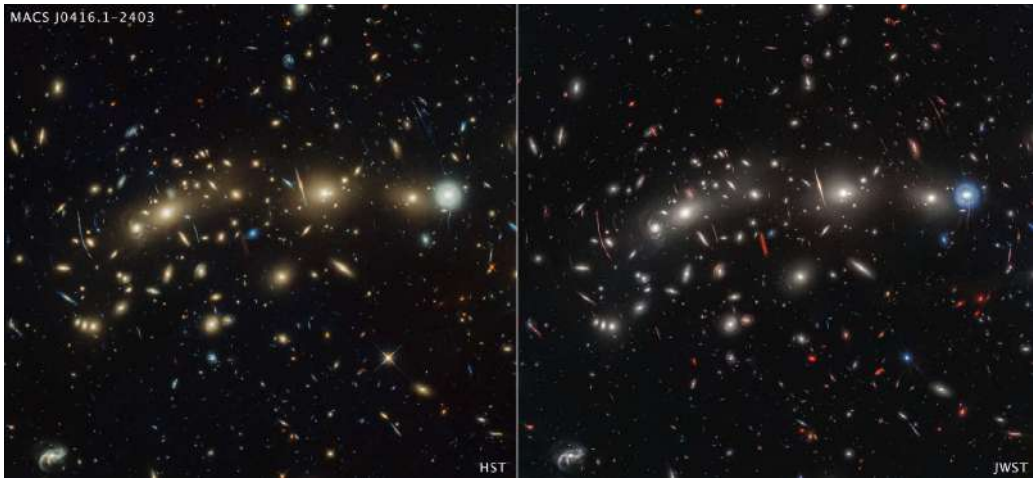

Figure 2.5: The lensing galaxy cluster MACS J0416.1-2403. *Left*: A RGB HST composite image of the cluster (HST filters: ACS/F435W, F606W, F814W, and WFC3/IR F105W, F125W, F140W, F160W). *Right*: A RGB JWST composite image of the cluster (JWST NIRCam filters: F090W, F115W, F150W, F200W, F277W, F356W, F410M, F444W). Credits: NASA, ESA, CSA, STScI.

The Ultradeep NIRSpec and NIRCam ObserVations before the Epoch of Reionization (UNCOVER, Bezanson et al. 2024) survey is a JWST Cycle 1 public Treasury survey that obtained deep NIRCam multiband imaging (down to $\sim 29 - 30$ AB magnitude) and ultradeep low-resolution NIRSpec spectroscopy of the HFF galaxy cluster Abell 2744. This project was designed to reach two aims, the identification of first-light galaxies at redshift $z \geq 10$, and the characterization of the ultra-low luminosity galaxies at $z \sim 6-7$.

The CAnadian NIRISS Unbiased Cluster Survey (CANUCS, Willott et al. 2022) aims to use the unparallel imaging capabilities of JWST in order to build robust SL mass models in galaxy clusters to study high redshift galaxies. With three of the four instruments on board JWST (NIRCam, NIRISS, and NIRSpec), CANUCS targeted, with ~ 200 hours of observing time, five massive clusters known to be effective gravitational lenses: Abell 370, MACS J0416.1−2403, MACS J1423.8+2404, MACS J0417.5-1154, and MACS J1149.6+2223.

2.6 Spectroscopy

Spectroscopy plays a crucial role in SL modelling of galaxy clusters: indeed, secure redshift measurements are necessary to identify the multiple images of the same background source and to properly reconstruct the total mass profile of a lensing cluster. In fact, as outlined in Chapter 1, the observed deflection angle depends on the total mass of the deflector, and on the mutual distances between the observer, lens, and source, hence on their redshifts. These can be measured with spectrographs, which are classified into two main categories: multi-object spectographs and integral-field units (IFUs). In the first case, a set of targets on the field of view (FoV) of the instrument is defined before observations take place, and slits or fibres are placed in correspondence with their positions. In the second case, the spectrum is spatially resolved across the instrument FoV. Integral-field spectroscopy allows for a blind search of multiple images, unlike multi-

unit spectroscopy. This results in a significant increase of the number of multiple images that can be detected: as a matter of fact, some emission-line multiply-imaged objects, such as Lyman-α high-redshift sources, may not have an optical counterpart to be detected. Nonetheless, IFUs have a considerably smaller FoV with respect to imaging instruments, which therefore limits the observations to a relatively narrow region of the cluster, typically its core, where most SL features are observed.

A significant step forward has been done with the advent of the Multi Unit Spectroscopic Explorer (MUSE, Bacon et al. 2010) at the Very Large Telescope, installed in 2014. MUSE has a modular structure composed of 24 identical IFUs spanning the wavelength range from $4750\,\text{Å}$ to $9350\,\text{Å}$ with a constant sampling of $1.25\,\text{Å}/\text{pix}$. The instruments operates in two modes: the Wide and Narrow Field modes. The Wide Field Mode (WFM) covers a $1' \times 1'$ FoV, with a spatial sampling of $0.2''/\text{pix}$, and has a spatial resolution FWHM of approximately $0.4''$ at $\lambda = 700\,\text{nm}$. The Narrow Field Mode (NFM) is characterized by a FoV of $\sim 7.5'' \times 7.5''$, with a spatial sampling of $0.025''/\text{pix}$ and a spatial resolution FWHM of approximately $0.06'' - 0.08''$. MUSE can allow for the simultaneous identification and study of cluster members and multiply imaged background sources out to $z \sim 6.6$. Its capabilities have been demonstrated by several detailed lens models based on its data (see, e.g., Richard et al. 2015; Grillo et al. 2016; Bergamini et al. 2021).

As far as space-based spectroscopy, here we recall the spectrographs installed in the *Euclid* and the JWST telescopes, whose data have been used to perform the analyses described in this Thesis. The *Euclid* telescope is equipped with a slitless spectrograph on the NISP instrument (see Chap. 4 for further details, and Euclid Collaboration: Jahnke et al. 2024; Euclid Collaboration: Gillard et al. 2025). Differently from IFUs and multi-object spectrographs, a slitless spectrograph measures spectra without a small slit. This methodology works best in sparsely populated fields, as it spreads each point source out into its spectrum, and crowded fields, including galaxy clusters, can be too confused: close-by sources tend not to be discriminated, and their spectra can blend, resulting in potential contaminations. Furthermore, as far as the *Euclid* pipeline for spectra extraction is concerned, it is not possible to extract spectra in a automatic way: given the limitation mentioned above, in a crowded field like a galaxy cluster, it is necessary to proceed manually. Finally, the wavelength range covered by the *Euclid* spectrograph in NISP runs from 920 nm to 1850 nm. Given the Hα emission line, which is one of the most prominent features used to measure the redhift of sources,this range corresponds to a redshift range $0.40 \leq z \leq 1.82$, hence only lensed background sources lying within this interval may be detected.

A further step has been done thanks to the launch of the JWST: indeed, among its instruments, it hosts the Near INfrared Spectrograph (NIRSpec, Jakobsen et al. 2022; Böker et al. 2023), a multi-object spectrograph. More details about the characteristics of this instrument are deferred to Chap. 6.

CHAPTER 3

Lens modelling

Nowadays, there exists a wide variety of algorithms that allow for the reconstruction of the total mass distribution of a galaxy cluster by means of SL. Regardless of the specific method adopted, the purpose of SL modelling is to find a representation of the projected mass distribution on the lens plane that yields the smallest scatter between the observed and model-predicted lensing observables. Typically, SL modelling algorithms use as input constraints the positions of the multiple images of the same background sources (referred to as families, or systems), but, in some cases, one includes also luminosity, time delay, and surface brightness measurements.

Lensing algorithms fall within two main categories, according to how the deflectors are described: parametric and free-form algorithms. Parametric methods consist in representing the total mass distribution of the lens as a set of physically-motivated density profiles, each of which is described by analytic functional forms depending on a set of parameters (see, e.g., Jullo et al. 2007; Oguri 2010a; Suyu & Halkola 2010; Lombardi 2024). The aim of this class of methods is to find the suitable set of parameters minimizing the scatter between the observed and model-predicted positions of the multiple images. On the other hand, free-form (or gridded) methods are also available: in this case, the deflector is not described in terms of a predetermined mass density profile, but is subdivided into a pixelised grid, and the mass of each pixel is optimised (see, e.g., Diego et al. 2005; Cha & Jee 2022). Alternatively, lenses may be described in terms of base functions, including shapelets, Fourier components, or something else (see later). Depending on the method, the number of grid cells can range between a few dozen and many thousands. A regularization terms is introduced as to avoid discontinuities between adjacent cells. In this case, the value of the mass element of each pixel is optimized, thus resulting in a number of free parameters which is one or two orders of magnitude higher than parametric methods. A brief overview of some of the principal SL algorithms is presented in Table 3.1.

Parametric algorithms are currently the most widely used for SL reconstruction of massive galaxy clusters (Grillo et al. 2015; Jauzac et al. 2015; Acebron et al. 2022; Bergamini et al. 2019, 2023a). They are conceptually motivated by cosmological simulations of structure formation, according to which cluster-scale masses are observed to be composed of large- and small-scale DM halos that are gravitationally bound. In addition, they more easily avoid the over-fitting problems that might affect free-form lensing modelling, given the extremely high number of free parameters the latter approaches require with respect to the limited number of lensing observables (Meneghetti et al. 2017), and can naturally accommodate for astrophysically-motivated priors on the parameters that describe the physical properties of the cluster and its member galaxies (Jullo et al. 2007). Differently from parametric methods, free-form approaches can be used to compare cluster properties, e.g., the radial slope of the projected total mass density, against theoretical

Table 3.1: List of some of the most commonly used SL algorithms. They are grouped according to whteher they are parametric or free-form methods. A reference for each of them is also given.

Typology	Algorithm	Reference
Parametric	`LensTool`	Kneib et al. (1996); Jullo et al. (2007)
	`Light-Traces-Mass`	Broadhurst et al. (2005)
	`GLAFIC`	Oguri (2010a)
	`GLEE`	Suyu & Halkola (2010)
	`GRAVLENS`	Keeton (2010)
	`Gravity.jl`	Lombardi (2024)
Free-form	`PixeLens`	Williams & Saha (2004)
	`WSLAP+`	Diego et al. (2005, 2007)
	`SWUnited`	Bradač et al. (2006)
	`Grale`	Liesenborgs et al. (2006)
	`MARS`	Cha & Jee (2022)
	`relensing`	Torres-Ballesteros & Castañeda (2023)

predictions, and have the flexibility to uncover substructure that may be potentially not be associated with light Ghosh et al. (2023). Models that do not include a prior assumption about the correlation between mass and light are particularly useful for investigating to what extent does mass follow light. In the following, we will refer to parametric modelling.

3.1 Overview on SL modelling techniques

3.1.1 Optimization schemes

As anticipated, SL algorithms aim at finding a proper representation of the total mass distribution of the lens by minimizing the scatter between the observed and model-predicted positions of the multiple images. This objective can be reached by means of two main optimization schemes: source- and image-plane schemes.

Source-plane scheme. The observed images are mapped to the source plane by directly applying the ray-tracing equation in Eq. (1.15). That is, given N observed multiple images of the same family, the corresponding background source position $\boldsymbol{\beta}_i$ is computed for each image i using

$$\boldsymbol{\beta}_i = \boldsymbol{\theta}_i - \boldsymbol{\alpha}_i \,, \tag{3.1}$$

with $\boldsymbol{\theta}_i$ the observed position of that image, and $\boldsymbol{\alpha}_i = \boldsymbol{\alpha}(\boldsymbol{\theta}_i)$ the scaled deflection angle evaluated in that position. This method does not require to include the true unlensed source positions as additional parameters in the optimization, thus resulting in a reduction of the dimensionality of the sampling space (which may be significant in the case of a lensing clusters, with dozens or more systems of multiple images). In addition, since this approach does not involve the inversion of the lens equation, this method is computationally faster.

Image-plane scheme. The sources are fully modelled (i.e., their positions are additional free parameters included in the optimization) and the corresponding images

are evaluated with a computational inversion of the lens equation. With respect to the previous approach, this method is more time-consuming and slower, yet more robust and accurate, since, differently from the other, involves less approximations (Oguri 2010b). In this scheme, the model-predicted multiple images (through the inversion of the lens mapping) are directly compared to the observed ones.

3.1.2 Optimization methodology

The optimization process typically requires the minimization of a χ^2 function, or, complementarily, the maximization of a likelihood function.

Chi square: χ^2. When optimizing on the source plane, Eq. (3.1) is applied to compute the predicted position of the background source of the ith family of multiple images, given a set of parameters $\boldsymbol{p}$: $\boldsymbol{\alpha}_i = \boldsymbol{\alpha}_i(\boldsymbol{p})$. Given $\boldsymbol{\beta}_i^{\rm true}$ the true position of the ith source, for each image k of the system the corresponding $\boldsymbol{\beta}_{k,i}$ is computed, and the $\chi^2_{\rm sp}$ on the source plane is

$$\chi^2_{\rm sp} = \sum_{j=1}^{N_{\rm s}} \sum_{k=1}^{N_i} \left(\frac{|\boldsymbol{\beta}_i^{\rm true} - \boldsymbol{\beta}_{k,i}|}{\sigma_k} \right)^2 , \tag{3.2}$$

with σ_k the measurement uncertainty on the position of the kth image of source i mapped on the source plane[1], N_i the number of multiple images of system i, and $N_{\rm s}$ the number of background sources. The positions of the sources $\boldsymbol{\beta}^{\mathbf{true}}$ are unknown, therefore are model parameters. By minimizing the chi square $\chi^2_{\rm sp}$, we look for the minimal scatter between the source points leading to the observed images. Conversely, when optimizing on the image-plane, for each image l the observed position $\boldsymbol{x}_l^{\rm ob}$ is directly compared with the model-predicted position $\boldsymbol{x}_l^{\rm pr}$ through

$$\chi^2_{\rm ip} = \sum_{l=1}^{N} \left(\frac{|\boldsymbol{x}_l^{\rm ob} - \boldsymbol{x}_l^{\rm pr}|}{\sigma_l} \right)^2 , \tag{3.3}$$

with the sum running over all the observed images.

Bayesian techniques. Alternatively, the optimization can be performed by means of a Bayesian approach. Bayes' theorem is used to compute the probability $P(\boldsymbol{p}|\boldsymbol{d}, M)$ of a set of parameters $\boldsymbol{p}$ of a model M given the observed data $\boldsymbol{d}$ as

$$P(\boldsymbol{p}|\boldsymbol{d}, M) = \frac{\mathcal{L}(\boldsymbol{d}|\boldsymbol{p}, M) P(\boldsymbol{p}|M)}{P(\boldsymbol{d}|M)} . \tag{3.4}$$

where $\mathcal{L}(\boldsymbol{d}|\boldsymbol{p}, M)$ is the likelihood of the data given the parameters, $P(\boldsymbol{p}|M)$ is the prior, i.e., the a priori knowledge of the parameters, and $P(\boldsymbol{d})$ is a normalisation that does not depend on $\boldsymbol{p}$, called evidence. $P(\boldsymbol{p}|\boldsymbol{d}, M)$ is called the posterior, and it is the probability distribution SL codes aim at sampling. The evidence is a normalization factor that ensures that the posterior is a proper probability distribution,

$$P(\boldsymbol{d}|M) = \int \mathcal{L}(\boldsymbol{d}|\boldsymbol{p'}, M) P(\boldsymbol{p'}|M) \mathrm{d}\boldsymbol{p'} , \tag{3.5}$$

Differently from the Chi square technique, computing the posterior distribution in a Bayesian framework allows for the reconstruction of the whole probability distribution of the parameters of the model, given the data, instead of yielding only the set of parameters minimising the χ^2 (or, equivalently, maximising the likelihood).

[1] Please refer to Lombardi (2024) for further details.

3.1.3 A note on background sources

For simplicity, background sources (and the corresponding observed images) are typically modelled as point-like, which are then characterized by their position on the source plane only. This results, when explicitly including the sources positions in the optimization, in the inclusion of a limited number of additional parameters. However, real astronomical sources (especially multiply-lensed galaxies by a galaxy cluster) are not point-like, rather they are characterized by an extended surface brightness distribution. Hence, it would be possible to exploit the observed brightness as additional constraint in lensing modelling. To do so, there are two main approaches.

Parametric extended sources. Parametric extended sources can be used to describe the light distribution of lensed sources with an analytic expression, depending on a given set of parameters, or with a linear combination of them.

Non-parametric extended sources. In this case, no parametric profile is assumed to describe the surface brightness distribution of the source, rather the surface brightness $f(\boldsymbol{\theta})$ is expressed as a linear superposition of basis functions $b_n(\boldsymbol{\theta})$,

$$f(\boldsymbol{\theta}) = \sum_n c_n b_n(\boldsymbol{\theta}) \,, \tag{3.6}$$

with $\boldsymbol{\theta}$ the position on the source plane and $\{c_n\}$ the coefficients of the linear combination. It is possible to perform inference on those without including them in the inference algorithm. There are various ways to model this sources. They may be described in terms of a regular grid of pixels, with one weight for each of them. In this case, the surface brightness of the source can be interpolated using a suitable interpolation kernel, e.g., a 1st order B-spline (i.e., a top-hat kernel), or a 2nd order B-spline (a linear interpolation). Alternatively, one may describe the surface brightness in terms of non-local basis functions, like rectangular or circular shapelets.

The surface brightness of observed sources differs from the original surface brightness because of gravitational lensing and of the effects of the point spread function (PSF). Hence, both these issues have to be properly taken into account. Non-parametric extended modelling of background sources has been applied on galaxy- and cluster-scale (Acebron et al. 2024) systems.

3.2 SL modelling with `Gravity.jl`

All the SL analyses presented in the present Thesis are performed with the parametric SL modelling code `Gravity.jl` (Lombardi 2024). Written in the Julia language (Bezanson et al. 2014), `Gravity.jl` allows for the reconstruction of the total mass distribution of a galaxy cluster by means of a Bayesian approach. Among the main features (and specifics) of this software, here we recall the following.

Julia-based

Julia is a high-level and high-performance programming language for technical computing. To the user, Julia is an interpreted language, similar to Python, and it allows one to use multiple dispatches (i.e., a function may accept multiple argument types). Julia also adopts just-in-time compilation (JIT) techniques: the first time a function is called with some specific parameter types, Julia compiles it to machine code, and then caches the

result. As a consequence, Julia can achieve performance comparable to that of C or Fortran while maintaining the flexibility and ease of use of an interpreted language. Julia is also designed to be easy to use for parallel and distributed computing, as well as for GPU-based computing.

Multiplane gravitational lensing

`Gravity.jl` can perform analyses of lens systems composed of multiple lensing planes at different distances (i.e., redshifts). As shown in literature (see, e.g., Seitz & Schneider 1992; Hilbert et al. 2009) the lensing equations can be written iteratively. A sketch of multiplane lensing, and its development within `Gravity.jl` is given in Figure 3.1. Let us denote with δ_i the vector representing the intersection of the extension of the ith light path segment with the plane containing the observer. We have $\delta_1 = 0$. Calling $\boldsymbol{\xi}_i$ the angular position of the intersection of the light path with the ith lensing plane, as seen from the observer, we have

$$\delta_{i+1} = \delta_i + d_i \hat{\alpha}(\boldsymbol{\xi}_i)\,, \tag{3.7}$$

$$\boldsymbol{\xi}_{i+1} = \boldsymbol{\xi}_i - \rho_i \delta_{i+1}\,. \tag{3.8}$$

Here, $\hat{\alpha}$ is the deflection angle, d_i the distance to the ith lensing plane, and $\rho_i = d_{i,i+1}/d_i d_{i+1}$ is the ratio of the distance between the ith plane and the next $(i+1)$th plane, and the distances of the ith and $(i+1)$th planes to the observer.

The differential of previous equations gives the Jacobian matrix of the lensing equation. After defining

$$\Delta_1 = \begin{pmatrix} 0 & 0 \\ 0 & 0 \end{pmatrix}\,, \tag{3.9}$$

and

$$A_1 = \begin{pmatrix} 1 & 0 \\ 0 & 1 \end{pmatrix}\,, \tag{3.10}$$

the null and identity matrices, respectively, we can write

$$\Delta_{i+1} = \Delta_i + d_i \frac{\partial \hat{\alpha}(\boldsymbol{\xi}_i)}{\partial \boldsymbol{\xi}_i} A_i\,, \tag{3.11}$$

and

$$A_{i+1} = A_i - \rho_i \Delta_{i+1}\,, \tag{3.12}$$

where A_i is the Jacobian matrix estimated at the ith lens plane

Image measurements

As anticipated, the purpose of parametric SL modelling is to recover the set of parameters of the density profiles used to model the total mass distribution of the deflector giving the smallest difference between the observed and model-predicted lensing constraints. In the analyses presented in this Thesis, the positions of the multiple images, treated as point-like sources, represent the observables employed in constraining the lens models. We can therefore build a statistical model as follows. Image measurements are assumed to have Gaussian errors in `Gravity.jl`: hence, the probability of observing an image at the position $\boldsymbol{x}^{\rm ob}$ given the model-predicted position $\boldsymbol{x}^{\rm pr}$ can be expressed as a bivariate normal distribution with covariance matrix Σ,

$$P(\boldsymbol{x}^{\rm ob}|\boldsymbol{x}^{\rm pr}) = (2\pi)^{-1}\,{\rm det}\Sigma^{-1/2}\,{\rm exp}\left\{-\frac{1}{2}(\boldsymbol{x}^{\rm ob}-\boldsymbol{x}^{\rm pr})^{\rm T}\,\Sigma^{-1}\,(\boldsymbol{x}^{\rm ob}-\boldsymbol{x}^{\rm pr})\right\}\,. \tag{3.13}$$

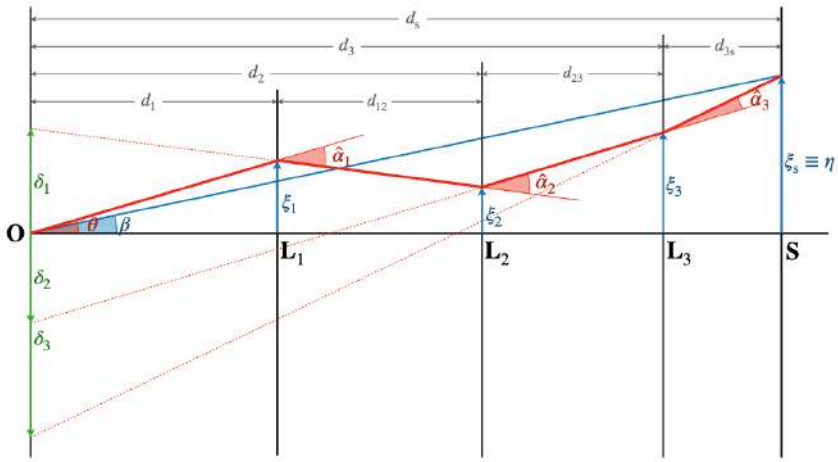

Figure 3.1: Schematic representation of a multiplane gravitational lens system. The observer ($\mathbf{O}$) is on the left, the source ($\mathbf{S}$) on the right. The lens is composed of multiple lensing planes, $\mathbf{L_i}$. A light ray (red) emitted by the source plane is deflected by the lensing planes and the associated image is formed at the observer's position along the direction $\boldsymbol{\theta}$. The blue line in the direction $\boldsymbol{\beta}$ is the position that the source would have in the absence of lensing. The deflection angles $\boldsymbol{\alpha}_i$ are computed at the angular positions $\boldsymbol{\xi}_i$ of the images. The mutual distances between the planes are marked at the top of the figure. Image from Lombardi (2024).

We assume that all image measurements are independent: therefore, the joint probability to observe a set of images $\{\boldsymbol{x}_i^{\rm ob}\}$ given the corresponding model-predicted positions $\{\boldsymbol{x}_i^{\rm pr}\}$, namely the likelihood, is

$$\mathcal{L}(\{\boldsymbol{x}_i^{\rm ob}\}|\{\boldsymbol{x}_i^{\rm pr}\}) = \sum_{i=1}^{N} P(\boldsymbol{x}_i^{\rm ob}|\boldsymbol{x}_i^{\rm pr})\,, \tag{3.14}$$

where the sums run over the N observed multiple images.

Optimization schemes

`Gravity.jl` allows for the sampling of the likelihood in three different ways, or schemes: the above mentioned source- and image-planes, and the additional *simplified image-plane*. This is an hybrid mode. Sources are still mapped to the source plane with Eq. (1.15), and a fiducial source position is computed by taking into account the mapped uncertainties. The sources are then mapped back to the lens plane, where the likelihood is computed. This approach requires the explicit inversion of the lens equation, but, differently from the image-plane scheme, avoids the explicit use of source parameters in the sampling, hence keeping the same number of free parameters as the source-plane mode. More specifically, we may classify the parameters $\boldsymbol{p}$ of the lens model as in Eq. (3.4) into source $\boldsymbol{s}$ (namely, their positions) and lens parameters $\boldsymbol{l}$: $\boldsymbol{p} = (\boldsymbol{s}, \boldsymbol{l})$. Since we are interested in $\boldsymbol{l}$, we may marginalize over $\boldsymbol{s}$ and express the posterior as

$$P(\boldsymbol{l}|\boldsymbol{d}) = \int P(\boldsymbol{l}, \boldsymbol{s}|\boldsymbol{d})\mathrm{d}\boldsymbol{s} = \frac{P(\boldsymbol{l})\int \mathcal{L}(\boldsymbol{d}|\boldsymbol{l}, \boldsymbol{s})P(\boldsymbol{s})\mathrm{d}\boldsymbol{s}}{\int \mathrm{d}\boldsymbol{l}' P(\boldsymbol{l}')\int \mathcal{L}(\boldsymbol{d}|\boldsymbol{l}', \boldsymbol{s}')P(\boldsymbol{s}')\mathrm{d}\boldsymbol{s}'}\,. \tag{3.15}$$

Here, the likelihood depends on the lens parameters only, and is expressed as a marginalization over $\boldsymbol{s}$, namely,

$$P(\boldsymbol{l}|\boldsymbol{d}) = \int \mathcal{L}(\boldsymbol{d}|\boldsymbol{l}, \boldsymbol{s})P(\boldsymbol{s})\mathrm{d}\boldsymbol{s}\,, \tag{3.16}$$

which allows us to rewrite Bayes' theorem as usual,

$$P(\boldsymbol{l}|\boldsymbol{d}) = \frac{\mathcal{L}(\boldsymbol{d}|\boldsymbol{l})P(\boldsymbol{l})}{P(\boldsymbol{d})} = \frac{\mathcal{L}(\boldsymbol{d}|\boldsymbol{l})P(\boldsymbol{l})}{\int \mathrm{d}\boldsymbol{l}'\mathcal{L}(\boldsymbol{d}|\boldsymbol{l}')P(\boldsymbol{l}')}\,. \tag{3.17}$$

This marginalization corresponds to the computation of a partial evidence over the source position.

Sampling algorithms

To sample the posterior distributions of the lens models, `Gravity.jl` allows the user to choose from a wide variety of algorithms. The principal ones are the following:

Emcee. This is an affine-invariance Markov Chain Monte Carlo (MCMC) algorithm (Goodman & Weare 2010). This method is particularly efficient in exploring the parameter space in case the posterior distribution is unimodal.

Hamiltonian Monte Carlo (HMC). The Hamiltonian Monte Carlo (HMC) algorithm (Neal 2011; Betancourt 2017) is a sampling technique based on the introduction of a fictitious moment variable, allowing for a more efficient exploration of the parameters' space.

Nested sampling. This method (Skilling 2004; Chopin & Robert 2008) is very efficient in computing the evidence and sampling from a multimodal posterior distribution. It is based on the idea of transforming the integral over the parameters' space into a sum of integrals over the likelihood, and then sampling from the likelihood.

Parallel tempering (PT). The parallel tempering (PT) algorithm (Syed et al. 2019; Surjanovic et al. 2022, 2023) generalizes the Metropolis-Hastings one by running in parallel several chains, each at a different *temperature* β ($0 \leq \beta \leq 1$), i.e., each one obtaining samples from the modified distribution $\mathcal{L}(\boldsymbol{d}|\boldsymbol{p}, M)^{\beta}\, P(\boldsymbol{p}|M)^{1-\beta}$. When $\beta = 0$, the corresponding chain explores the prior, whereas for $\beta = 1$ the chain explores the posterior distribution. The algorithm alternates between a *local* exploration phase, where the chains are run independently, and a *global* exploration phase, in which the chains are coupled and the states (the temperatures) are exchanged between them. This algorithm is particularly efficient in exploring the parameter space when the posterior distribution is multimodal.

Figures of merit

In order to quantify the goodness of the lens models, we adopt two main figures of merit. First, the root mean square (rms), which is a measure of the scatter between the observed and model-predicted positions of the multiple images, defined as

$$\Delta_{\rm rms} = \sqrt{\frac{1}{N_{\rm im}} \sum_{i=1}^{N_{\rm im}} \left|\boldsymbol{\Delta}_i\right|^2} = \sqrt{\frac{1}{N_{\rm im}} \sum_{i=1}^{N_{\rm im}} \left|\boldsymbol{x}_i^{\rm ob} - \boldsymbol{x}_i^{\rm pr}\right|^2}\,, \tag{3.18}$$

where $\boldsymbol{\Delta}_i$ is the difference between the observed ($\boldsymbol{x}_i^{\rm ob}$) and model-predicted ($\boldsymbol{x}_i^{\rm pr}$) position of the ith image, and $N_{\rm im}$ is the total number of multiple images considered in the model.

Secondly, we estimate the evidence of the Bayes' theorem, which allows us to compare alternative modelling choices, i.e., different total mass parametrizations (hence, different number of free parameters) and/or different sets of multiple images. Indeed, the probability $P(M|\boldsymbol{d})$ that the model M is correct, given the data, can be estimated by using Bayes' theorem again: we can write

$$P(M|\boldsymbol{d}) = \frac{P(\boldsymbol{d}|M)P(M)}{P(\boldsymbol{d})}\,. \tag{3.19}$$

Here, $P(M)$ is a prior over M, that is, our belief that M is the correct model before accessing the data. To compute the normalization term $P(\boldsymbol{d})$, one would need to marginalize over all possible models, which is generally impossible. Nevertheless, we can estimate the ratio $P(M|\boldsymbol{d})/P(M'|\boldsymbol{d})$, where M' is an alternative model,

$$\frac{P(M|\boldsymbol{d})}{P(M'|\boldsymbol{d})} = \frac{P(\boldsymbol{d}|M)P(M)}{P(\boldsymbol{d}|M')P(M')}\,. \tag{3.20}$$

3.3 Mass models

The choice of the class of models best suited to describe the total mass distribution of a given lens is a crucial part of the lens modelling. When the deflector is not point-like, but an extended mass, e.g. a galaxy or a galaxy cluster, it may be convenient to

begin with a simple model for its mass distribution. A good starting point is given by axisymmetric lenses, i.e., mass density distributions invariant with respect to rotations about the optical axis: $\Sigma(\boldsymbol{\xi}) = \Sigma(|\boldsymbol{\xi}|) = \Sigma(\xi)$. In this case, the scaled deflection angle $\boldsymbol{\alpha}$ is parallel to $\boldsymbol{\xi}$, and thus to $\boldsymbol{\beta}$: hence, the ray-tracing equation is one-dimensional, $\beta = \xi - \alpha(\xi)$. Under this condition, given Gauss' theorem, the deflection experienced by a light ray with impact parameter ξ is the same due to a point-mass $M = M(< \xi)$, i.e., the total mass enclosed within ξ. The scaled deflection angle is thus

$$\alpha(\theta) = \frac{M(< D_{\rm d}\theta)}{\pi D_{\rm d}^2 \Sigma_{\rm c} \theta} = \frac{2}{\theta} \int_0^{\theta} \theta' \kappa(\theta') {\rm d}\theta' = \theta \bar{\kappa}(\theta) \,, \tag{3.21}$$

with $\bar{\kappa}(\theta)$ the average value of the convergence within a distance θ from the lens centre. The lens equation can thus be rewritten as

$$\beta = \theta(1 - \bar{\kappa}(\theta)) \,. \tag{3.22}$$

Hence, a source in $\beta = 0$, i.e., behind the centre of the lens, is mapped into a ring-like image, where the average enclosed surface mass density is equal to the critical density. This configuration is called *Einstein ring*, and it has been observed in several galaxy-scale lens systems. The results obtained above for axisymmetric lensesGolse & Kneib (2002) generalized in case of oblate ellipsoid mass models.

In the following, we will briefly overview the principal density profiles adopted in the analyses presented this Thesis to model the different mass components (extended DM halos and cluster members) of the galaxy clusters studied.

3.3.1 The Singular Isothermal Sphere (SIS)

A simple mass profile often used in lens modelling is the so-called *singular isothermal sphere* (SIS). This model describes the distribution of an ideal gas confined by a spherically symmetric gravitational potential at thermal and hydrostatic equilibrium. In the astrophysical context, these may be stars within a galaxy or galaxies inside a galaxy cluster. The three-dimensional mass density profile $\rho(r)$ is

$$\rho(r) = \frac{\sigma_{\rm v}^2}{2\pi G r^2} \,, \tag{3.23}$$

with r the three-dimensional distance from the centre of the deflector and $\sigma_{\rm v}$ the velocity dispersion along the line of sight. The total mass enclosed within a sphere of radius r is

$$M(< r) = 4\pi \int_0^r r'^2 \rho(r') {\rm d}r' = \frac{2\sigma_{\rm v}^2 r}{G} \,, \tag{3.24}$$

whereas the projected bi-dimensional total mass profile $\Sigma(R)$ and the corresponding total mass $M(< R)$ enclosed within a circle of radius R can be derived by projecting ρ along the line of sight,

$$\Sigma(R) = 2 \int_R^{\infty} {\rm d}r \rho(r) \frac{r}{\sqrt{r^2 - R^2}} = \frac{\sigma_{\rm v}^2}{2GR} \,, \tag{3.25}$$

$$M(< R) = 2\pi \int_0^R R' \Sigma(R') {\rm d}R' = \frac{\pi \sigma_{\rm v}^2 R}{G} \,. \tag{3.26}$$

By introducing the *Einstein* radius

$$\theta_{\rm E} = 4\pi \left(\frac{\sigma_{\rm v}}{c}\right)^2 \frac{D_{\rm ds}}{D_{\rm s}}\,, \tag{3.27}$$

we can rewrite the lens equation as

$$\beta = \theta - \theta_{\rm E}\,{\rm sgn}(\theta)\,. \tag{3.28}$$

where sgn is the sign function. It follows that, if a source is located at $\beta \geq \theta_{\rm E}$, then only one image is produced at $\theta_+ = \beta + \theta_{\rm E}$. Vice versa, for $\beta < \theta_{\rm E}$, two images are produced, located at $\theta_\pm = \beta \pm \theta_{\rm E}$.

The SIS mass density profile can be easily generalized to an elliptical mass density profile, the Singular Isothermal Ellipsoid (SIE). Let q be the axis ratio between the semi-major and the semi-minor axes of the projected ellipse. We can generalize the expression for the surface mass density $\Sigma(R)$ by substituting the projected radius R with the elliptical radius $\hat{R}$,

$$R^2 \rightarrow \hat{R}^2 = x^2 + y^2/q^2\,, \tag{3.29}$$

with x and y the the coordinates along the semi-major and semi-minor axes, respectively. It is worth underlying that this substitution cannot be applied to generalize the deflection angle and the lensing potential: these quantities have to be computed differently. In addition, given the divergence of the profile for $r \rightarrow 0$, it is possible to introduce a core radius $r_{\rm c}$, i.e.,

$$r^2 \rightarrow r^2 + r_{\rm c}^2\,, \tag{3.30}$$

to avoid it. In this case, we obtain the non-singular isothermal sphere (NIS) or ellipsoid (NIE).

3.3.2 The dual pseudo-isothermal mass distribution (dPIE)

The projected total mass $M(R)$ for the SIS, NIS, SIE, and NIE density profiles does not converge to a finite value. To avoid these two non-physical behaviours, an alternative is given by the dual pseudo-isothermal ellipsoid (dPIE, Limousin et al. 2005; Elíasdóttir et al. 2007) density profile. This mass distribution generalizes the SIS profile by introducing a core radius $r_{\rm c}$, to avoid the divergence at small radii, and a truncation radius $r_{\rm t}$ that guarantees a finite total mass. Its spherical case has the following density profile,

$$\rho(r) = \frac{\rho_0}{(1 + r^2/r_{\rm c}^2)(1 + r^2/r_{\rm t}^2)}\,, \tag{3.31}$$

with

$$\rho_0 = \frac{\sigma_{\rm v}^2}{2\pi G}\frac{r_{\rm c} + r_{\rm t}}{r_{\rm c}^2 r_{\rm t}}\,. \tag{3.32}$$

This density profile shows an isothermal behaviour for small radii, whereas $\rho \propto r^{-4}$ for $r \rightarrow \infty$. The total mass enclosed within a sphere of radius r, the projected surface mass density $\Sigma(R)$, and the enclosed mass within a bi-dimensional radius R for a spherical dPIE are

$$M(<r) = \frac{2\sigma_{\rm v}^2}{G}\frac{r_{\rm t}}{r_{\rm t} - r_{\rm c}}\left[r_{\rm t}\arctan\left(\frac{r}{r_{\rm t}}\right) - r_{\rm c}\arctan\left(\frac{r}{r_{\rm c}}\right)\right], \tag{3.33}$$

$$\Sigma(R) = \frac{\sigma_{\rm v}^2}{2G}\frac{r_{\rm t}}{r_{\rm t} - r_{\rm c}}\left(\frac{1}{\sqrt{R^2 + r_{\rm c}^2}} - \frac{1}{\sqrt{R^2 + r_{\rm t}^2}}\right), \tag{3.34}$$

$$M(<R) = \frac{\pi\sigma_{\rm v}^2}{G}\frac{r_{\rm t}}{r_{\rm t}-r_{\rm c}}\left(\sqrt{R^2+r_{\rm c}^2}-r_{\rm c}-\sqrt{R^2+r_{\rm t}^2}+r_{\rm t}\right). \tag{3.35}$$

As anticipated, differently from the SIS profile, the dPIE profile yields a finite total mass in the limit $r \to \infty$, namely $M_{\rm lim} = \pi\sigma_{\rm v}^2 r_{\rm t}/G$.

As for the SIS density profile, Eq. (3.34) can be generalized for an elliptical total mass density profile: the projected radius R has to be substituted with the elliptical radius $\hat{R}$ defined above in the previous equations.

The dPIE mass distribution in `Gravity.jl` and `LensTool`

The dPIE mass density profile is implemented in different ways in `LensTool` (Kneib et al. 1996; Jullo et al. 2007) and `Gravity.jl`. Therefore, it is necessary to provide conversion functions to pass from the set of parameters of one code to the other one. This mass distribution is characterised by 5 parameters[2], namely the velocity dispersion of the lens, its core and truncation radii, its ellipticity and its position angle. Let $\{\sigma_{\rm LT}, r_{\rm core}^{\rm LT}, r_{\rm cut}^{\rm LT}, \varepsilon_{\rm LT}, \theta_{\rm LT}\}$ denote the set of parameters of the PIEMD model in `LensTool` (LT) and $\{\sigma_{\rm g}, r_{\rm core}^{\rm g}, r_{\rm cut}^{\rm g}, q_{\rm g}, \theta_{\rm g}\}$ the equivalent set in `Gravity.jl` (g). Then, the conversion functions are the following.

In `LensTool`, angles are measured anti-clockwise from the east axis (positive x-semiaxis), whereas in `Gravity.jl`, they are measured clockwise from the north axis (positive y-semiaxis). additionally, in `LensTool` angles are measured in degrees, whereas in `Gravity.jl` they are measured in radians. Thus, the relation between $\theta_{\rm LT}$ and $\theta_{\rm g}$ is

$$\theta_{\rm g} = (90^\circ - \theta_{\rm LT})\,\frac{\pi}{180^\circ}\,. \tag{3.36}$$

In `Gravity.jl`, the ellipticity is defined as the ratio between the semi-minor and semi-major axes of the projected ellipticity, differently from `LensTool`. The relation between the two definitions $q_{\rm g}$ and $\varepsilon_{\rm LT}$ is

$$\varepsilon_{\rm LT} = \frac{1-q_{\rm g}^2}{1+q_{\rm g}^2}\,, \tag{3.37}$$

or

$$q_{\rm g} = \sqrt{\frac{1-\varepsilon_{\rm LT}}{1+\varepsilon_{\rm LT}}}\,. \tag{3.38}$$

Both the core and the truncation radii are subject to the same conversion, which follows from a different implementation of the elliptical radius in the two softwares. The relation between them is

$$r_{\rm cut}^{\rm g} = 2\,r_{\rm cut}^{\rm LT}\,\frac{\sqrt{q_{\rm g}}}{1+q_{\rm g}}\,, \tag{3.39}$$

and

$$r_{\rm core}^{\rm g} = 2\,r_{\rm core}^{\rm LT}\,\frac{\sqrt{q_{\rm g}}}{1+q_{\rm g}}\,, \tag{3.40}$$

where $q_{\rm g}$ is related to $\varepsilon_{\rm LT}$ through Eq. (3.38).

[2]except for the position of the lens, which does not change for one code to the other one

The relation between $\sigma_{\rm g}$ and $\sigma_{\rm LT}$ follows a different implementation of both the elliptical radius and the normalisation term of the dPIE mass distribution in the two codes. The relation is

$$\sigma_{\rm g} = \sigma_{\rm LT} \sqrt{\frac{3}{2}} \sqrt{\frac{r_{\rm cut}^{\rm LT}}{r_{\rm cut}^{\rm LT} - r_{\rm core}^{\rm LT}}} \sqrt{\frac{2\sqrt{q_{\rm g}}}{1+q_{\rm g}}} \,. \tag{3.41}$$

3.3.3 External perturbations

Many lenses are not isolated, but may be embedded in crowd environments with one or more angularly-close mass elements, which are not part of the main deflector (e.g., galaxies belonging to a specific galaxy cluster) but may still introduce perturbations to the gravitational potential of the lens. Similarly, several lenses may be characterised by a so-called hierarchy of mass elements: the largest mass elements, also called macro-lenses, that are responsible for the the largest-scale lensing effects, and the smallest mass clumps within the macro-lenses, called *substructures*, which act as perturbers. Multi-modality in the mass distribution of gravitational lenses is of particularly importance in the context of galaxy clusters, since they form through accretion of smaller-scale structures. It has been shown that multi-modal mass distributions are very efficient deflectors, with the shear of each mass component causing the critical curves and the caustics of the main lens to extend into regions of low convergence (Torri et al. 2004; Meneghetti et al. 2010a). In addition, substructures may significantly affect the appearance and the positions of the multiple images of the sources lensed by the principal lens. It may then be sometimes necessary to embed the main lens into an external shear field. We can model it by introducing a deflection potential ψ_γ that has the form (in polar coordinates, see Meneghetti 2022)

$$\psi_\gamma(r,\theta) = \frac{|\gamma|}{2} r^2 \cos[2(\theta - \theta_\gamma)] \,, \tag{3.42}$$

with $|\gamma|$ the modulus of the shear and θ_γ the position angle on the lens plane, which yields the direction of the shear perturbation.

3.4 Parametrising the total mass distribution of galaxy clusters

Galaxy clusters are complex systems, being composed of several constituents (galaxies, ICM and DM). However, SL is a linear phenomenon, meaning that, as already pointed out in Chapter 1, the lensing deflection of a system of point masses (or of a continuous mass distribution) can be obtained as the sum (the integral) of the contributions of each element. Similarly, we can dissect the total mass distribution of a galaxy cluster into its mass components, at the different scales. The total mass of clusters is typically decomposed into extended cluster- and galaxy-scale (sub-) halos. The former represent both the diffuse DM clumps hosting clusters and the hot gas content. The latter are used to parametrize the total mass enclosed within the cluster member galaxies. In addition, perturbation terms, such as foreground or background objects, and shear terms, are sometimes introduced, to take into account the lensing effect of mass structures nearby or along the line of sight.

We can express the the total gravitational potential ϕ of a galaxy cluster as

$$\phi = \sum_{i=1}^{N_{\rm h}} \phi_i^{\rm halo} + \sum_{j=1}^{N_{\rm gas}} \phi_j^{\rm gas} + \sum_{j=1}^{N_{\rm g}} \phi_j^{\rm gal} + \phi^{\rm shear}\,, \tag{3.43}$$

where $\phi_i^{\rm halo}$ is the gravitational potential corresponding to the ith extended DM halo (out of $N_{\rm h}$ halos), $\phi_i^{\rm gas}$ is the gravitational potential of the ith extended gas halo (out of $N_{\rm gas}$ halos), and $\phi_i^{\rm gal}$ is the gravitational potential of the ith galaxy (out of $N_{\rm g}$ cluster members). $\phi^{\rm shear}$ is the term taking into account external perturbations (see Sect. 3.3.3).

The density profiles describing the mass distribution associated with the ICM are kept fixed (i.e., with fixed parameters) by measuring, when available, their X-ray luminosity distribution, following the prescriptions by Bonamigo et al. (2017, 2018). Having fixed this component, which represents the major baryonic constituent of galaxy clusters, it is then possible to disentangle between the galactic and DM contributions to the total mass budget of a cluster.

The DM extended halos used to parametrize the total mass distribution of the clusters discussed in this Thesis are described with either NIE or dPIE density profiles. As recalled in Chapter 2, cosmological simulations suggest that DM settles in a mass distribution well fitted by a NFW density profiles over different mass scales. This density profile, however, increases significantly the computation time required to optimize a lens model. The superposition of a few dPIEs has been shown to be, in projection, very well fit by a two-dimensional NFW profile (Bonamigo et al. 2018): hence the use of dPIE density profiles.

The total mass distribution of cluster members is typically modelled using spherical dPIE profiles, with a vanishing core radius, centred in the luminosity centres of the member galaxies, resulting in two free parameters for each sub-halo, namely the velocity dispersion and the truncation radius. Each galaxy cluster hosts up to few hundreds of members that are used in lens modelling, leading to a number of free parameters exceeding the number of available observable constraints. To deal with this issue and reduce the number of free parameters, two power-law scaling relations are often introduced, in which the central velocity dispersion $\sigma_{{\rm gal},i}$ and truncation radius $r_{{\rm cut},i}$ of the ith cluster member are scaled according to the corresponding luminosity L_i,

$$\sigma_{{\rm gal},i} = \sigma_{\rm ref} \left(\frac{L_i}{L_0}\right)^{\alpha}\,, \tag{3.44}$$

and

$$r_{{\rm cut},i} = r_{\rm cut,ref} \left(\frac{L_i}{L_0}\right)^{\beta}\,, \tag{3.45}$$

where L_0 is a reference luminosity, and $\sigma_{\rm ref}$ and $r_{\rm cut,ref}$ the corresponding parameter values. Eq. (3.44) is a generalization of the Faber-Jackson relation (Faber & Jackson 1976). Following the prescriptions of Bergamini et al. (2019, 2021), the values of the slope α and the normalization term $\sigma_{\rm ref}$ can be fitted in case the measurements of the stellar velocity dispersion for a subset of cluster members are available (please refer to the following Chapter for more details). The value of β can instead be derived by assuming a fixed scaling relation between the total mass $M_{{\rm tot},i}$ of the ith cluster member and its luminosity, i.e., $M_{{\rm tot},i}/L_i \propto L_i^{\gamma}$. For a spherical dPIE mass density profile, the total mass for the ith cluster member is $M_{{\rm lim},i} \propto \sigma_{{\rm v},i}^2 r_{{\rm t},i} \propto L_i^{2\alpha} L_i^{\beta}$. Under this assumption, we obtain

$$\beta = \gamma - 2\alpha + 1\,, \tag{3.46}$$

with $\gamma = 0.2$ to be consistent with the observed Fundamental Plane relation (Dressler et al. 1987; Djorgovski & Davis 1987; Bender et al. 1992).

3.4.1 A brief note on ellipticals in galaxy clusters

As mentioned in Chapter 2, galaxies populating galaxy clusters are mainly early-type (elliptical) galaxies, in particular in their inner regions. These galaxies are characterized by relations that connect their luminosities, which depend on their stellar population, to their stellar velocity dispersions, which in turn are associated with their total masses. A first relation was found in 1976 by Sandra Faber and Roger Jackson Faber & Jackson (1976): the central velocity dispersion σ_0 is proportional to the luminosity L according to

$$L \propto \sigma_0^4 \,. \tag{3.47}$$

Here, σ_0 is measured within a circle of radius $R_\mathrm{e}/8$, with R_e the effective (or half-light) radius, the radius of the circle enclosing half of the total luminosity L of the galaxy. Almost a decade later, another relation was found for ellipticals, the so-called *Fundamental Plane* (FP, Dressler et al. 1987; Djorgovski & Davis 1987; Bender et al. 1992). We can provide a quick intuitive derivation of this law as follows. The effective radius of ellipticals R_e has been observed to be related to the average surface brightness within it $\langle I \rangle_\mathrm{e}$ through the relation (see, e.g., Bender et al. 1992)

$$R_\mathrm{e} \propto \langle I \rangle_\mathrm{e}^{-0.83} \,. \tag{3.48}$$

From this, it follows that

$$L = 2\pi R_\mathrm{e}^2 \langle I \rangle_\mathrm{e} \propto R_\mathrm{e}^2 \langle I \rangle_\mathrm{e} \propto \langle I \rangle_\mathrm{e}^{-0.66} \,. \tag{3.49}$$

Given the Faber-Jackson relation in Eq. (3.47), we can derive

$$R_\mathrm{e} \propto \sigma_0^{1.4} \langle I \rangle_\mathrm{e}^{-0.85} \,, \tag{3.50}$$

We can express this relation in logarithmic form as

$$\log R_\mathrm{e} = 1.4 \log \sigma_0 + 0.34 \langle \mu \rangle_\mathrm{e} + \gamma \,, \tag{3.51}$$

where $\langle \mu \rangle_\mathrm{e}$ is the average surface brightness within R_e, related to $\langle I \rangle_\mathrm{e}$ through $\langle \mu \rangle_\mathrm{e} = -2.5 \log \langle I \rangle_\mathrm{e}$, and γ is a constant. Eq. (3.51) defines a plane in a three-dimensional space, one projection of which is the Faber-Jackson relation.

We may derive the FP starting from the virial theorem. Indeed, according to the latter, the mass $M \propto \sigma_0^2 \, R_\mathrm{e}$. If we apply Eq. (3.49), we find

$$R_\mathrm{e} \propto \frac{\sigma_0^2}{\langle I \rangle_\mathrm{e}} \frac{L}{M} \,, \tag{3.52}$$

which is consistent with Eq. (3.50) given

$$\frac{\sigma_0^2}{\langle I \rangle_\mathrm{e}} \frac{L}{M} \propto \frac{\sigma_0^{1.4}}{\langle I \rangle_\mathrm{e}^{0.85}} \,, \tag{3.53}$$

i.e.,

$$\frac{M}{L} \propto \frac{\sigma_0^{0.6}}{\langle I \rangle_\mathrm{e}^{0.15}} \propto \frac{M^{0.3}}{R_\mathrm{e}^{0.3}} \frac{R_\mathrm{e}^{0.3}}{L^{0.15}} \,. \tag{3.54}$$

Thus, the FP derives from the virial theorem provided that

$$\left(\frac{M}{L}\right) \propto M^{0.2}\,, \tag{3.55}$$

or

$$\left(\frac{M}{L}\right) \propto L^{0.15}\,, \tag{3.56}$$

i.e., the total mass-to-light ratio slightly increases with the total mass or luminosity of a galaxy.

Part II

Strong Lensing in the Euclid era

CHAPTER 4

SL analysis of the *Euclid* ERO galaxy cluster Abell 2390

In addition to the surveys cited in Chapter 2, there are several other on-going and planned ones aimed at obtaining larger and larger samples of cluster lenses. Despite these are expected to be shallower than the HST and JWST cluster lens samples discussed above, the majority of them stands to detect clusters and exploit weak gravitational lensing to study them. Among these, there is the *Euclid* Wide Survey (EWS, Euclid Collaboration: Scaramella et al. 2022) with the *Euclid* satellite. Launched in 2023, *Euclid* (Euclid Collaboration: Mellier et al. 2024) is an European Space Agency (ESA) 1.2-metre space telescope dedicated to the study of the imprint of dark energy and gravity through two complementary cosmological probes: weak lensing and galaxy clustering (via baryonic acoustic oscillations and redshift space distortion). At the end of the operations, *Euclid* will have observed approximately 14,050 deg^2 of the extragalactic sky (see Fig. 4.1), through two main surveys: the above-mentioned EWS, and the Euclid Deep Survey (EDS). The former will cover about 14,000 deg^2 of the sky (more than a third of the total sky), while the latter will monitor about 50 deg^2 (which is about the same area that HST observed in total in the past 35 years), with the instruments observing three fields (the yellow dots in Fig. 4.1) with an exposure time much longer than the rest of the sky to capture fainter galaxies. Overall, these surveys will last 6 years, which is Euclid's nominal mission time.

The telescope is equipped with two main instruments: the VISible camera (VIS, Euclid Collaboration: Cropper et al. 2024) and the Near-Infrared Spectrometer and Photometer (NISP, Euclid Collaboration: Jahnke et al. 2024). VIS is a large-format imager with a FoV of 0.54 deg^2 sampled at $0.1''$/pixel, operating in a single passband (VIS/$I_{\rm E}$, wavelength range 530 – 920 nm). The VIS detectors are CCDs, and each CCD has 4132×4096 pixels organised in a 6×6 configuration, such that VIS images comprise 6.09×10^8 pixels. Complementary, NISP provides multiband photometry and slitless grism spectroscopy in the wavelength range ∼920−2020 nm. Its FoV covers 0.57 deg^2 sampled at $0.3''$/pixel. It is composed of of a 4×4 grid of detectors, with 2048×2048 pixels. The NISP photometric channel consists of three passbands: NISP/$Y_{\rm E}$ (wavelength range ∼950 – 1212 nm), NISP/$J_{\rm E}$ (∼1168 – 1567 nm), and NISP/$H_{\rm E}$ (∼1521 – 2020 nm). As far spectroscopy is concerned, the NISP spectroscopic channel enables the simultaneous acquisition of slitless spectra for thousands of objects across the FoV.

Euclid is expected to detect ∼60,000 galaxy clusters in the redshift range $0.2 \lesssim z \lesssim 2.0$ (Euclid Collaboration: Mellier et al. 2024). It is forecast that ∼50,000 of them will have background galaxy densities greater than 15 galaxies per square arcmin, allowing accurate determination of cluster masses from weak lensing studies. In addition to these, *Euclid* is expected to increase the number of currently known SL systems by nearly two orders of magnitude, by observing $\sim 170,000$ galaxy-scale strong lenses (Collett 2015; Acevedo Barroso et al. 2024), $\sim 2,000$ lensed quasars, and thousands of SL features in

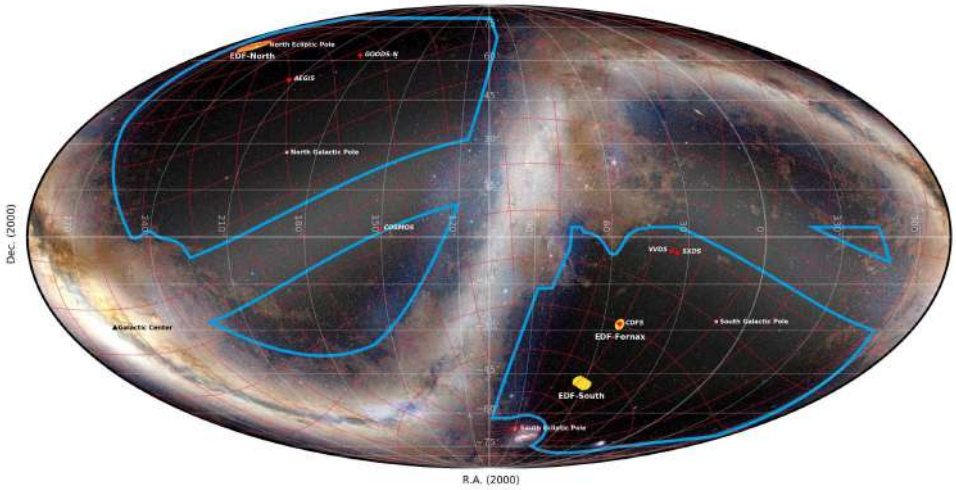

Figure 4.1: Euclid region of interest (RoI) in an all-sky Mollweide projection. The blue borders enclose the 15,000 deg^2 RoI that contains the observed sky of the EWS+EDS surveys. The RoI excludes the Galactic and ecliptic planes. The three Euclid Deep Fields are marked in yellow, and auxiliary fields in red. From Euclid Collaboration: Mellier et al. (2024). Credits: Euclid Consortium Survey Group/J.-C. Cuillandre.

galaxy clusters distributed in the same redshift range $0.2 \lesssim z \lesssim 2.0$ (Euclid Collaboration: Mellier et al. 2024; Boldrin et al. 2012, 2016). These estimates are consistent with the number of SL clusters found in the first Quick data release Q1 of the telescope (Euclid Collaboration: Bergamini et al. 2025): out of 1,260 galaxy clusters identified over 63 deg^2, 83 of them were indeed classified as potential lensing clusters. These observations will help providing accurate total mass profiles of such systems from the kiloparsec to the megaparsec scales, thanks to the ability of the telescope to combine strong and weak lensing measurements in galaxy clusters (Meneghetti et al. 2010b, 2014; Merten et al. 2015; Umetsu et al. 2014, 2020) and better understanding the assembly history of these objects. These findings will also further test the predictions of the standard cosmological ΛCDM model and alternative dark matter models.

It is in this context that the Early Release Observations (ERO) program Magnifying Lens (Atek et al. 2024) stands. This project targeted two galaxy clusters, Abell 2390 (see Fig. 4.2) and Abell 2764, with the aim to showcase the science questions that *Euclid*'s observations of galaxy clusters will be able to address. In particular, the ERO program was designed to collect data that could be used for different studies, including those focused on the primordial Universe, galaxy evolution, and active galactic nuclei, as well as strong and weak lensing, and galaxy cluster physics. In addition, the observations collected are meant to provide a first glimpse of the *Euclid* imaging data: the early investigation of the dataset will help reveal and address challenges and limitations for a full scientific exploitation of the prime mission survey data.

The first ERO target was the galaxy cluster Abell 2390 (hereafter A2390, redshift $z = 0.231$). Located at (RA $= 328.4034183°$, Dec $= 17.6954744°$, J2000.0), it is one of the richest systems in the Abell galaxy cluster sample (Pello et al. 1991; Le Borgne et al. 1991), that was first selected in a search for arcs on the basis of its bright X-ray emission (Fort 1990; Boehringer et al. 1998; Allen et al. 2001). Indeed, this cluster has a luminosity

Table 4.1: Limiting magnitudes at 5σ reached in each *Euclid* filter of the A2390 field. The depth measurements assume an aperture diameter of $0.6''$ and $0.3''$ for NISP and VIS, respectively.

$I_{\rm E}$	$Y_{\rm E}$	$J_{\rm E}$	$H_{\rm E}$
27.01	25.18	25.22	25.12

$L_X \sim 2.7 \times 10^{45}\,{\rm erg\,s^{-1}}$ in the 0.1–2.4 keV range (Boehringer et al. 1998). This system is also characterized by elongated arcs (Mellier et al. 1990; Feix et al. 2010; Olmstead et al. 2014; Richard et al. 2021) and has an estimated mass M_{200}[1]$\simeq 1.06 \times 10^{15}\,{\rm M_\odot}$ obtained through a weak lensing analysis (Okabe & Smith 2016). This cluster was previously subject to several SL studies based on ground and HST imaging (Pierre et al. 1996; Pelló et al. 1999; Swinbank et al. 2006). It is with the motivations outlined above that we performed the first high-precison parametric SL analysis of the galaxy cluster Abell 2390 using *Euclid* imaging, combined with archival deep spectroscopy obtained with MUSE at the VLT.

4.1 Imaging and spectroscopy

4.1.1 Imaging

The lens cluster A2390 was targeted on November 28th, 2023 as part of the performance-verification (PV) phase of the mission. Three reference observing sequences (ROS, Euclid Collaboration: Scaramella et al. 2022) were obtained, implying three times the nominal EWS exposure time. Each ROS had a duration of 70.2 minutes, for a total exposure time of ~ 3.30 hours. A standard 4-point dither pattern, with an offset of $120'' \times 220''$, was applied for each ROS. Additionally, a $3' \times 3'$ dither was adopted between the individual ROS to maximize the depth. The observations were performed in all *Euclid*'s four filters: the limiting magnitudes for each filter are reported in Table 4.1. The full data reduction pipeline is described in detail in Cuillandre et al. (2024). A photometric catalogue was extracted from the imaging with the public software `SourceXtractor++` (Kümmel et al. 2022; Bertin et al. 2022). A more in-depth description of the photometric measurements is given in Atek et al. (2024). The astrometric calibration was carried out with the software `SCAMP` (Bertin 2006): the reference catalogue used for the calibration of the ERO data was *Gaia* Data Release 3 (Gaia Collaboration: Vallenari et al. 2023).

We also used archival multi-band HST imaging of this cluster obtained with the Wide Field and Planetary Camera 2 (WFPC2) within the CYCLE4 HIGH HST Program 5352 (P.I.: Fort, Bezecourt & Soucail 1997). The lens cluster A2390 was observed by HST on December 10th, 1994 for a total exposure time of 2100 seconds.

4.1.2 Spectroscopy

We made use of archival VLT/MUSE data of A2390, which was observed in the WFM for a total integration time of 2 hours in September, 2014 within the 120 GTO Program 094.A-0115 (P.I.: Richard, Richard et al. 2021). We employed the datacube available on the European Southern Observatory (ESO) Science portal, that was reduced by the Quality Control Group at ESO. The reduction consisted in the removal of instrument signatures,

[1] M_{200} is the total mass enclosed within a sphere with a radius inside which the total mass density of the cluster is 200 times the critical density of the Universe, at the redshift of the cluster.

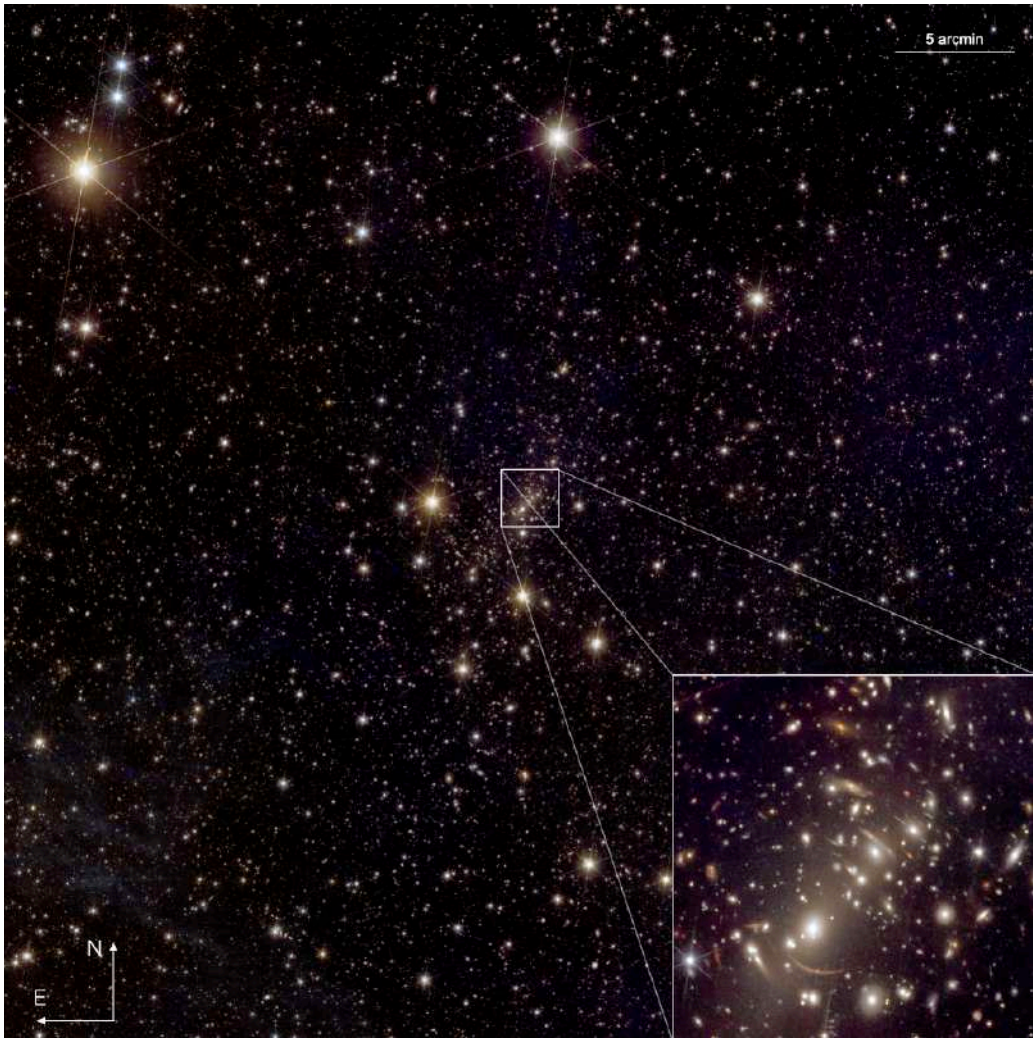

Figure 4.2: Euclid colour-composite image of the A2390 field. The blue channel is the $I_{\rm E}$ image; green is $Y_{\rm E}$, and red is $H_{\rm E}$. The whole field covers about 0.5 deg^2. The inset is centered on A2390 and covers the central $2' \times 2'$ region displaying SL features. From Atek et al. (2024).

the subtraction of the sky, and the combination of the two Observing Blocks (OBs) as the latest step. Additionally, we enhanced the background sky subtraction by means of the Zurich Atmosphere Purge (ZAP, Soto et al. 2016) tool. The MUSE footprint is shown in red in Fig. 4.3. The resulting datacube spans the wavelength range from 4750 Å to 9350 Å, with a constant sampling of 1.25 Å/pix, and covers a $1' \times 1'$ FoV, with a spatial sampling of $0.2''$/pix. It has a median point-spread-function (PSF) FWHM of approximately $0.83''$. We registered the astrometry with respect to the HST/F814W image of the cluster.

We built a spectroscopic catalogue of the sources in the MUSE FoV following the procedure adopted in Caminha et al. (2019). We considered a cutout of the HST/F814W image corresponding to the MUSE pointing imprint, and applied the software `SExtractor` (`v2.28.0`, Bertin & Arnouts 1996) to identify all the included sources. We used the detected positions as the centres of circular apertures with radius of $0.8''$, within which we extracted the spectrum. This aperture was chosen as to include the majority of the flux of the corresponding source, while reducing at the same time potential contamination of angularly close-by objects. We also added in this catalogue those sources that did not show a HST/F814W continuum, but clear emission lines. These were identified through visual and automatic inspection, using the Cube Analysis and Rendering Tool for Astronomy (`CARTA`, Comrie et al. 2021) tool. We extracted their spectra within circular apertures with the same radius, $0.8''$, centred on the luminosity peak detected in narrow-line images obtained collapsing the datacube around the wavelengths of the detected lines.

We measured the redshift values for the objects in the catalogue with use of the `Marz` (Hinton et al. 2016) software, by identifying spectral features, including emission and absorption lines, and continuum breaks with both automatic and visual analyses. We labelled each redshift measurement with a quality flag (QF), defined to be equal to 1 for non-possible measurements, equal to 2 for possible measurements based on faint spectral features, equal to 3 for secure measurements based on multiple features, and equal to 9 for measurements based on a single emission line. In some cases, if it was possible to characterize the single emission line (like, for instance, by observing a doublet or the typical asymmetric shape of the $\mathrm{Ly}\alpha$ line), we converted QF=9 objects to QF=3. The final MUSE catalogue contains 96 objects with a QF > 2 redshift measurement, divided into 6 stars or galactic objects, 36 potential cluster members, and 54 background objects, including 25 multiple images from 10 background sources.

Since the MUSE pointing is only restricted to the core of the galaxy cluster (see Fig. 4.3 and the insert of Fig. 4.2), we also considered ancillary archival spectroscopic measurements from several catalogues obtained with other instruments in order to complement the MUSE one: specifically, we used the catalogues by Sohn et al. (2020), based on the SDSS Data Release 14 (Abolfathi et al. 2018) and the 6.5m Multiple Mirror Telescope (MMT) Hectospec spectrograph (Fabricant et al. 2005), and the catalogue by Abraham et al. (1996), based on the Multi Object Spectograph (MOS) and the Subarcsecond Imaging Spectrograph (SIS) at the 3.6m Canada-France-Hawaii Telescope (CFHT). We cross-matched these catalogues in order to produce a final spectroscopic sample. When a source was present in more than one catalogue, we gave priority (if possible) to the redshift measurements obtained through our reduction of the MUSE datacube.

The final full spectroscopic catalogue consists of 592 sources within an effective FoV of approximately $\sim 40' \times 20'$: 36 are foreground galaxies/objects ($z \leq 0.211$), 405 are potential cluster members (i.e., lying in the redshift range $0.211 \leq z \leq 0.251$; see Sect. 4.2.1 for a detailed description of the selection of the cluster members), and 151 are background galaxies ($z \geq 0.251$), including 25 multiple images.

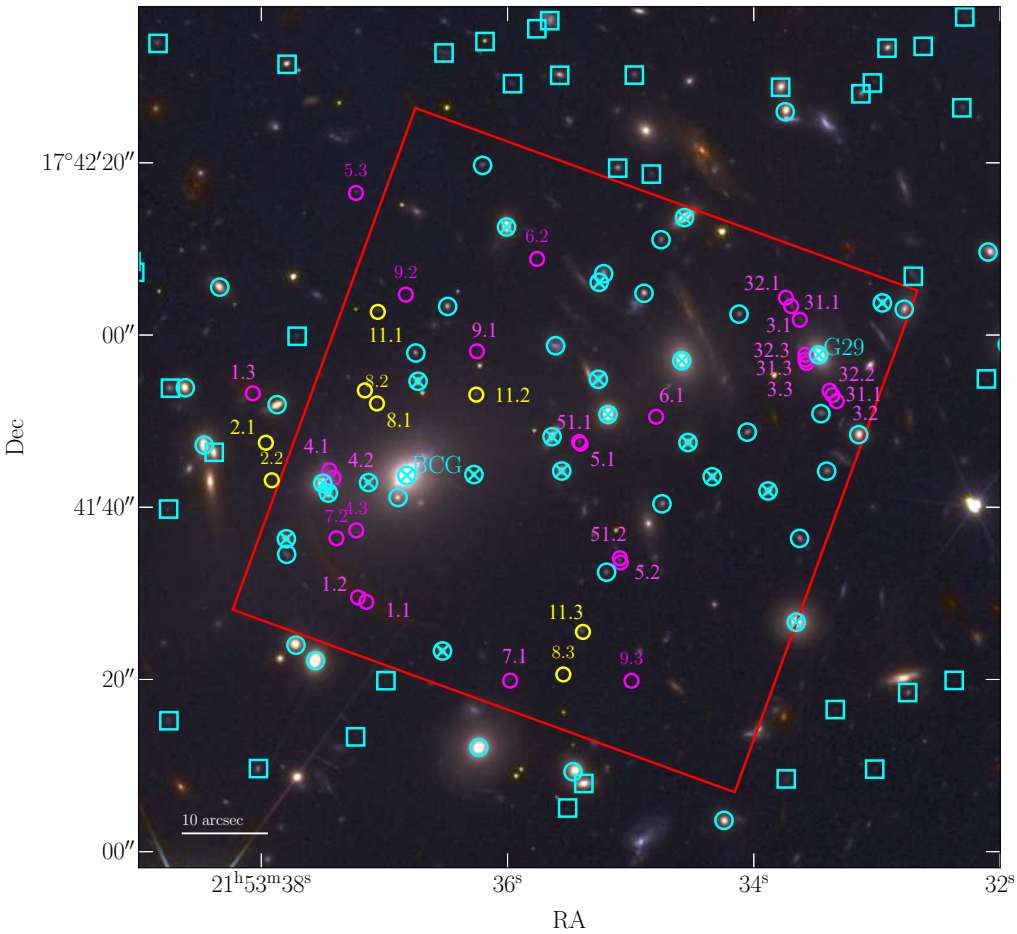

Figure 4.3: Colour-composite Euclid image (red: $H_{\rm E}$, green: $H_{\rm E}$+$I_{\rm E}$, blue: $I_{\rm E}$) of the galaxy cluster A2390. The MUSE footprint is shown in red. The spectroscopic (photometric) cluster members are represented with cyan circles (boxes). The 22 cluster members for which we measured the stellar velocity dispersion are further marked with cyan crosses. The spectroscopically-confirmed (photometric) multiple images included in our analysis are also shown in magenta (yellow). The multiple images are also labeled with their ID. The positions of the BCG and galaxy G29 are also marked. From Abriola et al. (2025)

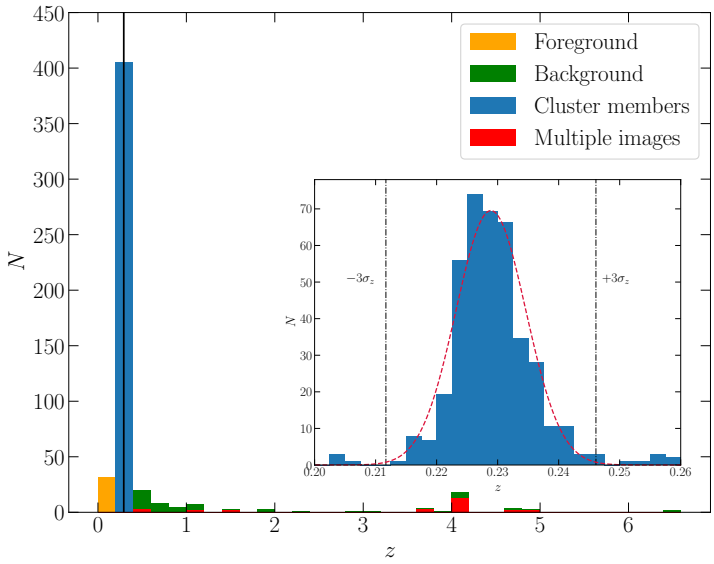

Figure 4.4: Spectroscopic redshift distribution of the objects in our final spectroscopic catalogue. Cluster members (i.e., lying in the redshift range $0.211 \leq z \leq 0.251$) are in blue, whereas foreground and background objects are in orange and green, respectively. Multiple images are depicted in red. The vertical black line locates the redshift of the galaxy cluster. The insert shows the cluster members selection illustrated in Sect. 4.2.1. The red dashed line identifies the best-fit Gaussian distribution, whereas the vertical black dotted lines define an interval of $\pm 3\sigma_z$ around the median cluster redshift. From Abriola et al. (2025)

4.2 Building the strong lensing models

We performed the SL analysis of A2390 using the above-mentioned software `Gravity.jl` (Lombardi 2024). We explored 11 total mass models, characterized by the same set of cluster members and multiple images but a different total mass parametrization. We label these total mass models as M1 to M11. We present in Table 4.2 a more detailed description of each of them. To sample the posterior distribution of the models explored in our work, we employed the NRPT algorithm implementation in the software. All the optimizations of the lens models were carried out in the simplified image-plane configuration.

4.2.1 Cluster members

Cluster members were selected by exploiting both spectroscopic (see Sect. 4.1.2) and multi-band *Euclid* photometric (Sect. 4.1.1) information. We first identified a sample of spectroscopically-confirmed cluster members starting from our spectroscopic catalogue, as follows. First, we restricted to those galaxies lying within $1.5'$ from the centre of the cluster, assumed to be the brightest cluster galaxy (BCG, marked in Fig. 4.3). This choice is motivated by the fact that SL features (i.e., multiple images and giant arcs) are observed within 50 arcseconds from the BCG. Secondly, we fitted the redshift distribution of these galaxies with a Gaussian distribution, with mean and standard deviation values $\hat{z} \pm \sigma_z = 0.231 \pm 0.005$, as depicted in the insert of Fig. 4.4. We thus identified 65 cluster members (cyan circles in Fig. 4.3), defined as those lying within $\pm 3\sigma_z$ from $\hat{z}$ (this corresponds to $\simeq \pm 3700\,\mathrm{km\,s^{-1}}$ around the cluster mean velocity). The magnitude distribution of these galaxies is represented with the orange solid line in Fig. 4.6.

We completed the spectroscopic sample by adding 114 further photometric (cyan boxes in Fig. 4.3), bright ($m_\mathrm{H} < 23$) members by studying the distribution of the galaxies in a colour-magnitude $I_\mathrm{E} - H_\mathrm{E}$ vs. H_E diagram, as shown in Fig. 4.5. To evaluate their colours, we considered magnitudes measured within a radius of $0.5''$, and restricted, as before, to the galaxies lying within $1.5'$ from the BCG. We fitted the red cluster sequence (RCS, see Chap 2) defined by the above-mentioned 65 spectroscopically-confirmed cluster members by means of a weighted linear regression. To do so, we used the Python package `ltsfit` (Cappellari et al. 2013), which performs a least square regression by iteratively clipping outliers (Rousseeuw & Van Driessen 2006). The result is presented in Fig. 4.5. We imposed a 3σ clipping, and thus discarded 4 members from the fit (represented by the blue crosses in Fig. 4.5; the red dots are the galaxies we employed for the fit). Given the best-fit, we extended our sample to comprise those galaxies (the green dots in Fig. 4.5) within $\pm\,\sigma_\mathrm{RCS} \simeq 0.1$ (the bold red dotted lines) from the RCS best-fit line (the solid red line), with σ_RCS the intrinsic scatter of the data-points around the best fit RCS.

Following the procedure presented in Granata et al. (2023, 2024), we measured the line-of-sight stellar velocity dispersion σ_gal for several cluster members from the MUSE data (their magnitude distribution is given by the red solid line in Fig. 4.6). The velocity dispersion measurements were obtained using the spectral fitting code `penalized PiXel-Fitting` (pPXF, Cappellari & Emsellem 2004; Cappellari 2023) to fit the observed spectra to a combination of 463 stellar spectral templates from the X-shooter Spectral Library (XSL) DR2 (Gonneau et al. 2020), convolved with a Gaussian line-of-sight velocity distribution. Following the methods of Cappellari & Emsellem (2004) and Granata et al. (2024), we assessed the statistical uncertainty on the velocity dispersion values by generating 10,000 synthetic MUSE spectra and finding a relation between the statistical

Table 4.2: Description of the different lens models explored to parametrize the total mass distribution of A2390.

Model	Description
M1	One cluster-scale DM halo 179 sub-halo components
M2	One cluster-scale DM halo 179 sub-halo components An external shear-like term
M3	One cluster-scale DM halo 179 sub-halo components The BCG excluded from the scaling relations
M4	One cluster-scale DM halo 179 sub-halo components The BCG excluded from the scaling relations An external shear-like term
M5	Two cluster-scale DM haloes 179 sub-halo components
M6	Two cluster-scale DM haloes 179 sub-halo components An external shear-like term
M7	Two cluster-scale DM haloes 179 sub-halo components The BCG excluded from the scaling relations
M8	Two cluster-scale DM haloes 179 sub-halo components The BCG excluded from the scaling relations An external shear-like term
M9	One cluster-scale DM halo 179 sub-halo components An external shear-like term Galaxy G29 excluded from the scaling relations (modelled as spherical dPIE density profile)
M10	One cluster-scale DM halo 179 sub-halo components An external shear-like term Galaxy G29 excluded from the scaling relations (modelled as elliptical dPIE density profile)
M11	Three cluster-scale DM haloes 179 sub-halo components An external shear-like term

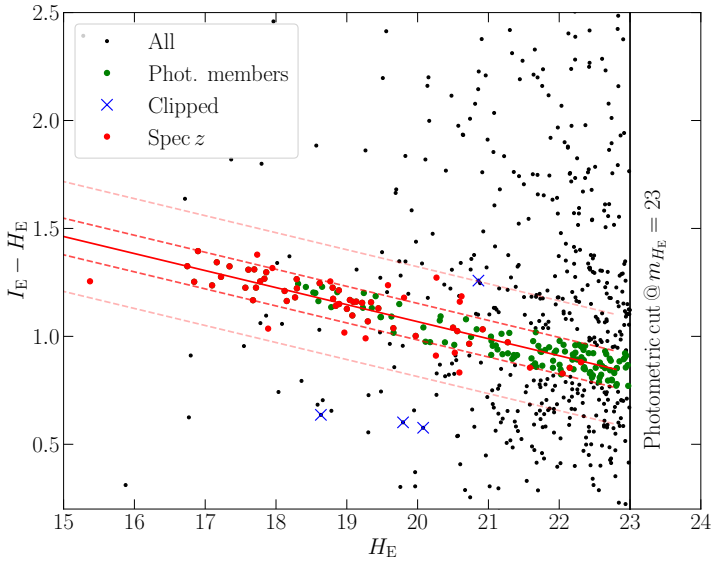

Figure 4.5: Colour-magnitude $I_{\rm E} - H_{\rm E}$ vs. $H_{\rm E}$ diagram. The red dots represent the 60 spectroscopically-confirmed cluster members that we employed to fit the RCS, whereas the 4 cluster members we discarded due to the clipping are in blue. The green dots are the photometric galaxies added to our cluster member sample. The solid red line is the best-fit RCS, while the dotted ones define a range of $\pm\sigma_{\rm RCS}$ (used for the selection of the cluster members) and $\pm 3\sigma_{\rm RCS}$ (used for the clipping) around the line, respectively. From Abriola et al. (2025)

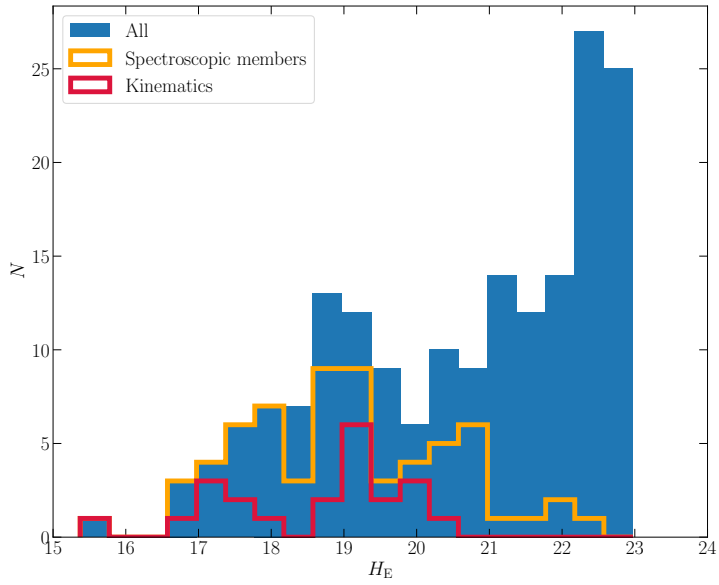

Figure 4.6: H_E magnitude distribution of the 179 cluster members included in our models (blue). The 65 spectroscopically-confirmed cluster members are enlightened in orange, whereas the sub-sample of the 22 galaxies for which we measured the central stellar velocity dispersion are in red. From Abriola et al. (2025)

error on $\sigma_{\rm gal}$ and signal-over-noise ratio $\langle S/N \rangle$. We required a spectral $\langle S/N \rangle \geq 10$ to ensure reliable velocity dispersion measurements, as shown by Bergamini et al. (2019) and Granata et al. (2024).

To measure the central stellar velocity dispersion of the cluster galaxies in their central regions, MUSE pixels were weighted by the surface brightness of the members in the *Euclid* I_E band, degraded and re-binned to match the MUSE PSF. Spectra were extracted within $1.5'$ circular apertures centered on each galaxy, which significantly improved the spectral $\langle S/N \rangle$. Light-weighting the cube results in values of the velocity dispersion approximately equivalent to those that would be measured within an aperture corresponding to the effective radius of each galaxy. Our final sample of cluster members with measured stellar velocity dispersion, presented in Table 4.3, includes a total of 22 MUSE member galaxies (we also measured the stellar velocity dispersion for a background galaxy). These are also marked with cyan crosses in Fig. 4.3. Three of the galaxies for which we measured $\sigma_{\rm gal}$ showed a spectrum potentially affected by light blending from nearby objects. Hence, for these galaxies we used the unweighted MUSE cube, and extracted the spectrum from a fixed $0.6''$ aperture, in order to reduce the contamination. These objects are marked in Table 4.3 with an asterisk. The H_E magnitude distribution of the 179 cluster members included in our models is given in Fig. 4.6.

4.2.2 Multiple image systems

Our SL models comprise 35 multiple images from 13 background sources, that were identified thanks to *Euclid* and archival HST imaging. Of these, 25 (corresponding to 10 families) are spectroscopically confirmed through our reduction of the MUSE datacube, spanning a redshift range between $z = 0.535$ and $z = 4.877$. These are represented with

Table 4.3: Catalogue of measured velocity dispersion values.

ID	R.A. [deg]	Dec. [deg]	$z_{\rm spec}$	$\sigma_{\rm gal}$ [$\rm km\,s^{-1}$]	$\delta\sigma_{\rm gal}$ [$\rm km\,s^{-1}$]	$\langle S/N \rangle$
1	328.403418	17.695474	0.2301	276.8	13.8	81.1
3	328.395241	17.693922	0.5212	114.1	4.4	28.0
5*	328.406259	17.695223	0.2280	183.4	3.6	45.2
8	328.402209	17.689812	0.2262	197.8	10.0	19.2
13	328.396608	17.697441	0.2317	233.3	2.6	77.7
15	328.407495	17.693431	0.2422	135.2	5.3	24.3
21*	328.406071	17.694906	0.2275	181.7	4.9	32.6
22	328.398174	17.695619	0.2316	96.0	4.0	23.0
23	328.394113	17.699178	0.2301	195.5	2.2	77.5
27	328.391192	17.694975	0.2299	136.7	5.3	24.0
28*	328.404712	17.695246	0.2313	174.5	8.3	18.8
29	328.389480	17.699362	0.2243	237.3	2.7	81.0
32	328.393082	17.695434	0.2268	95.7	5.1	17.6
33	328.398502	17.696725	0.2346	126.8	3.4	32.7
34	328.393902	17.696538	0.2278	93.7	3.9	24.4
35	328.401145	17.695504	0.2318	147.4	12.2	12.7
41	328.396935	17.698578	0.2201	90.3	5.0	21.8
48	328.403036	17.698513	0.2260	215.0	7.1	33.3
58	328.400041	17.703490	0.2317	230.0	3.4	56.3
59	328.396907	17.701705	0.2411	81.4	6.3	18.6
61	328.387322	17.701042	0.2246	99.4	6.1	17.2
65	328.394020	17.703793	0.2263	195.1	3.2	49.5
136	328.390237	17.690741	0.2279	159.1	11.9	10.1

Notes. We identify the galaxies included in this catalogue with their ID. We report the redshift of the galaxy $z_{\rm spec}$ (fourth column), its measured velocity dispersion value with $\sigma_{\rm gal}$ (fifth column) and its uncertainty with $\delta\sigma_{\rm gal}$ (sixth column), and the spectral $\langle S/N \rangle$ (seventh column). We mark the members potentially affected by light blending, for which we used a smaller aperture ($0.6''$ in radius, see Sect. 4.2.1) for the spectral extraction, with *.

magenta circles in Fig. 4.3. Systems 1 and 5 are both composed of three multiple images, of which only two had a spectroscopic confirmation, whereas the remaining (1.3 and 5.3, respectively) had been recognized as counter-image. Two families (8 and 11), despite being inside the MUSE footprint, do not show any prominent secure feature that allows us to determine their redshift. An additional family of multiple images (family 2) lies outside the footprint. The redshifts of these 3 multiple-image systems (families 2, 8 and 11) are then optimized in our lens models as additional parameters with uninformative flat priors between $z = 0.24$ and $z = 10$. These photometric multiple images are shown with yellow circles in Fig. 4.3. The specifics of the multiple images included in our models are given in Table 4.4. For each image we report its coordinates, as well as, if possible, its redshift as estimated through the reduction of the MUSE datacube and the corresponding MUSE quality flag (we follow the same assignment legend introduced previously). In our work, the positions of the multiple images represent the observables for our lens models.

4.2.3 Total mass parametrization

We parametrize the total mass distribution of the lens cluster A2390 as in Eq. (3.43), by modelling it as the sum of $N_{\rm h}$ extended haloes, representing the contribute of dark matter, $N_{\rm g}$ subhaloes, describing the galactic component, and a shear-like term which accounts for the presence of structures in the outskirts of the system and line-of-sight mass elements. The total gravitational potential ϕ of the deflector can thus be expressed as

$$\phi = \sum_{i=1}^{N_{\rm h}} \phi_i^{\rm halo} + \sum_{j=1}^{N_{\rm g}} \phi_j^{\rm gal} + \phi^{\rm shear} \,. \tag{4.1}$$

Dark matter mass distribution

The large-scale haloes representing the dark matter component are modelled as not-singular isothermal ellipsoids (NIEs, see Sect. 3.3.1). This density profile is characterized by six free parameters: the position on the sky (x, y), the axis ratio q, defined as before as the ratio between the semi-minor and semi-major axes of the projected ellipse, the position angle θ (computed clockwise from the North axis in `Gravity.jl`), the central velocity dispersion $\sigma_{\rm v}$ and the core radius $r_{\rm c}$. We explored total mass parametrizations including either one (models M1−M4 and M9−M10), two (models M5−M8), or three (model M11) extended dark matter haloes.

Galaxy-scale mass distribution

The cluster member galaxies (the sub-halo component of the galaxy cluster) are modelled in terms of spherical dPIE profiles (see Sect. 3.3.2). Fixing the positions of the cluster members to the measured values, for each galaxy this model is described by only three parameters: the central velocity dispersion σ_v, and the core and truncation radii, $r_{\rm c}$ and $r_{\rm t}$, respectively. We further reduced the number of free parameters by introducing the scaling relations given by Eq. (3.44) and Eq. (3.45). We used the total $H_{\rm E}$ magnitudes in the previous equations and, as reference luminosity, we adopted that of the BCG. The total $H_{\rm E}$ magnitude of the BCG is $m_{H_{\rm E}}^{\rm BCG} = 15.37$. Following the prescription in Bergamini et al. (2019, 2021), we benefited from the measured stellar velocity dispersion for 22 cluster members to fit the values of the normalization term $\sigma_{\rm ref}$ and the slope α of Eq. (3.44). In fitting, we also included an additional free parameter, the

Table 4.4: Coordinates and spectroscopic redshifts, with the corresponding MUSE quality flag, of the multiple image systems used to build our models.

ID	$z_{\rm spec}$	QF	R.A. [deg]	Dec. [deg]
1.1	1.038	3	328.404788	17.691397
1.2	1.038	3	328.405068	17.691541
1.3	1.038	–	328.408628	17.698124
2.1	–	–	328.408188	17.696531
2.2	–	–	328.407988	17.695320
3.1	4.048	3	328.390118	17.700497
3.2	4.048	3	328.388868	17.697870
3.3	4.048	3	328.389928	17.699370
31.1	4.048	3	328.390408	17.700937
31.2	4.048	3	328.389008	17.698067
31.3	4.048	3	328.389928	17.699210
32.1	4.048	3	328.390588	17.701209
32.2	4.048	3	328.389108	17.698210
32.3	4.048	3	328.389888	17.699100
5.1	4.048	3	328.397588	17.696557
5.2	4.048	3	328.396178	17.692668
5.3	4.048	–	328.405138	17.704588
51.1	4.048	3	328.397538	17.696498
51.2	4.048	3	328.396208	17.692806
4.1	0.535	3	328.406038	17.695641
4.2	0.535	3	328.405898	17.695396
4.3	0.535	3	328.405235	17.693915
6.1	1.465	3	328.395096	17.697592
6.2	1.465	3	328.399096	17.702482
7.1	4.877	3	328.399918	17.688857
7.2	4.877	3	328.405798	17.693449
8.1	–	–	328.404838	17.698218
8.2	–	–	328.404428	17.697798
8.3	–	–	328.398120	17.689056
9.1	3.653	3	328.401036	17.699392
9.2	3.653	3	328.403273	17.701490
9.3	3.653	3	328.395725	17.688863
11.1	–	–	328.404398	17.700751
11.2	–	–	328.401066	17.698081
11.3	–	–	328.397456	17.690428

Notes. System 2 could not be detected within the MUSE pointing, whereas families 8 and 11 did not display any secure feature, hence their spectroscopic redshifts and quality flags are not assigned. Images 1.3 and 5.3 do not have spectroscopic confirmation, thus we do not assign them a quality flag.

intrinsic scatter $\Delta\sigma_{\rm ap}$ of the measured velocities around the scaling relation. We adopted the same Bayesian approach presented in Bergamini et al. (2019): to sample the posterior distribution, we used the Python package `emcee` (Foreman-Mackey et al. 2013), and considered 12 walkers performing 10,000 steps each. We considered the following uni-

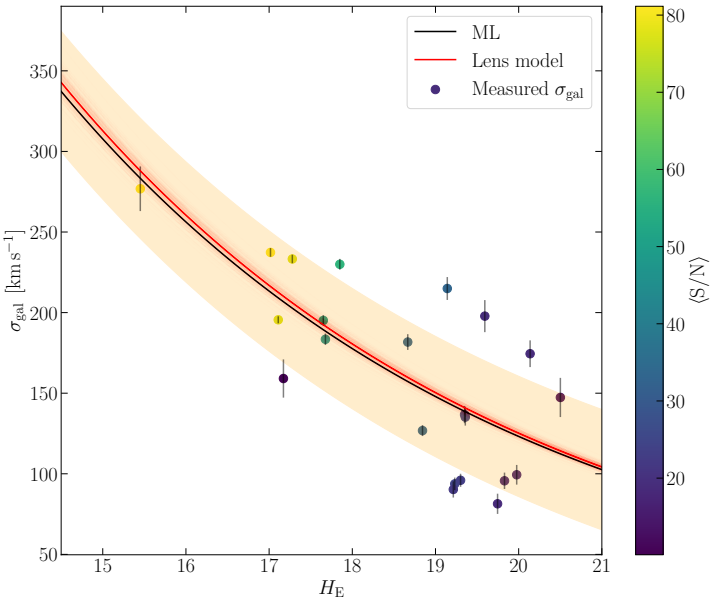

Figure 4.7: Measured stellar velocity dispersions of 22 MUSE spectroscopically-confirmed cluster members as a function of their *Euclid* $H_{\rm E}$ magnitudes. Their colours encode the mean signal-to-noise ratio of galaxy spectra, $\langle S/N \rangle$. The black solid line is the best-fit (maximum likelihood, ML) of the scaling relation in Eq. (3.44). The light orange band corresponds to the best-fit mean scatter $\Delta\sigma_{\rm ap}$ around the best-fit relation. The red solid curve corresponds the relation in Eq. (3.44) as obtained with the best fit parameters of our reference model. The light red area is estimated from 300 random values of $\sigma_{\rm ref}$ extracted from the Bayesian Markov chain Monte Carlo realizations of the reference model. From Abriola et al. (2025)

form priors for the three free parameters: $[\alpha_{\rm min}, \alpha_{\rm max}] = [0.0, 1.0]$, $[\sigma_{\rm ref,min}, \sigma_{\rm ref,max}] = [100\,{\rm km\,s^{-1}}, 600\,{\rm km\,s^{-1}}]$, and $[\Delta\sigma_{\rm ap,min}, \Delta\sigma_{\rm ap,max}] = [0\,{\rm km\,s^{-1}}, 100\,{\rm km\,s^{-1}}]$. The result of the fit is shown in Fig. 4.7: the black solid line is the best-fit scaling relation (obtained with the set of values maximizing the likelihood, labelled ML), while the light orange band represents the best-fit mean scatter $\Delta\sigma_{\rm ap}$ around the relation. The marginalized posterior distributions of the three parameters are instead shown in Fig. 4.8. With respect to previous works by Bergamini et al. (2019, 2021), where the same approach was followed for different lens galaxy clusters, we find a lower median value of α: $\alpha = 0.21 \pm 0.04$, whereas Bergamini et al. (2019, 2021) found values of $\alpha \sim 0.27 - 0.30$. Adopting $\alpha = 0.21$, it follows, given Eq. (3.46), $\beta = 0.78$.

For each sub-halo (galactic) component, the value of the core radius is kept fixed to $0.005''$. Given the results of the fit of the generalized Faber-Jackson relation described above, in our models we adopt for $\sigma_{\rm ref}$ a Gaussian prior with mean $285\ {\rm km\,s^{-1}}$ and standard deviation $41\ {\rm km\,s^{-1}}$, whereas an uninformative flat prior is assumed on $r_{\rm cut,ref}$. In models M3−M4 and M7−M8, the BCG is excluded from the scaling relations, and described independently in terms of a spherical dPIE profile, with both the velocity dispersion and the truncation radius as free parameters. In a similar manner, in models M9 and M10 galaxy G29 (see Fig. 4.3) is excluded from the scaling relations and modeled either with a spherical (M9) or an elliptical (M10) dPIE mass density profile.

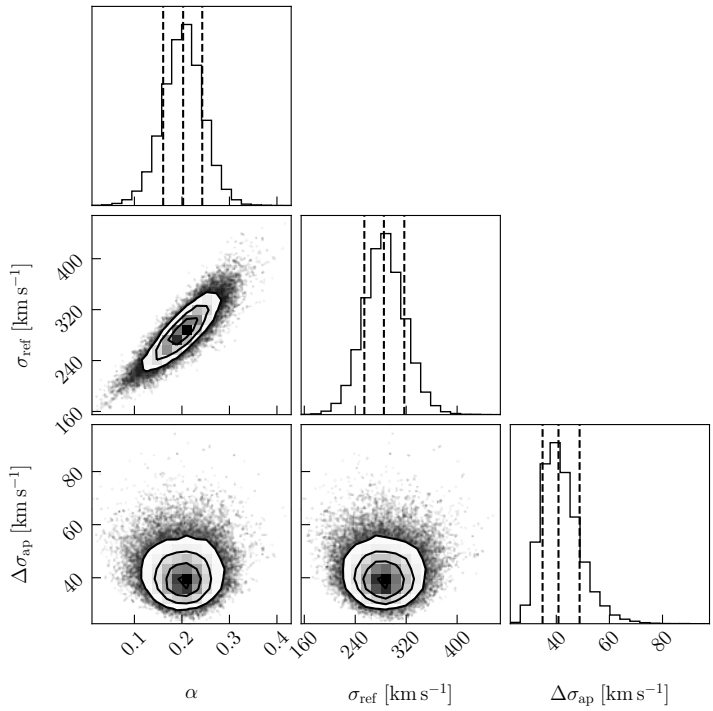

Figure 4.8: Posterior probability distribution for the Faber-Jackson relation calibration using the measurements of the velocity dispersion of 22 spectroscopically-confirmed cluster members. The 16th, 50th and 84th percentiles of the marginalized distributions for the slope (α), normalization ($\sigma_{\rm ref}$) and scatter around the scaling relation ($\Delta\sigma_{\rm ap}$) are displayed and shown as vertical dashed lines. From Abriola et al. (2025)

4.3 Results and discussion

In Table 4.5 we briefly summarize the main properties of the eleven lens models explored in this work, M1 to M11, by showing the principal figures of merit adopted to quantify their goodness: the root-mean-square displacement $\Delta_{\rm rms}$ between the positions of observed and model-predicted multiple images, defined as in Eq. (3.18), and the evidence of Bayes' theorem for each model.

Table 4.5: Figures of merit adopted to compare the total mass parametrizations explored. $N_{\rm par}$ and d.o.f. are the number of model free-parameters and the degrees-of-freedom, respectively. $\Delta_{\rm rms}$ is the root-mean-square displacement between the positions of observed and model-predicted multiple images. log$E$ is the natural logarithm of the evidence of Bayes' theorem for each model.

Model	$N_{\rm par}$	d.o.f.	$\Delta_{\rm rms}$ [$''$]	$-\log E$
M1	11	33	0.52	592
M2	13	31	0.40	476
M3	13	31	0.53	651
M4	15	29	0.39	479
M5	17	27	0.41	445
M6	19	25	0.31	379
M7	19	25	0.41	461
M8	21	23	0.34	393
M9	15	29	0.32	397
M10	17	27	0.32	399
M11	19	25	0.27	363

We first explored models (M1 to M4) comprising one single extended cluster-scale DM halo, then we added a second one (models M5 to M8). We also studied the impact of the inclusion (models M2, M4, M6, and M8) or exclusion (models M1, M3, M5, and M7) of an external shear term, as well as the removal of the BCG from the scaling relations (models M3, M4, M7, and M8). As can be seen from Table 4.5, the inclusion of an external shear term does help to significantly increase the accuracy of the models, by reducing the scatter between the observed and model-predicted positions of the multiple images by $\sim 0.1''$. On the other hand, the exclusion of the BCG from the scaling relations does not critically affect the figures of merit adopted. M6 stands out as the best model, being the one with the lowest value of $\Delta_{\rm rms}$ and highest evidence. Yet, it predicts the second DM halo to lie $\sim 50''$ north-west to the BCG, in a region with no clear concentration of galaxies. This halo lies in projection close to galaxy G29 (MUSE ID 29, see also Fig. 4.3 and Table 4.3), which is surrounded by the elongated arc where families 3, 31, and 32 of multiple images are observed. Furthermore, model M6 predicts for the second DM halo a velocity dispersion value of $\sim 300\,{\rm km/s}$, which is more consistent with that of a cluster member rather than a cluster-scale halo. These considerations motivated us in modelling galaxy G29 independently from the other cluster members, by removing it from the scaling relations. Hence, we explored two more models, M9 and M10, where we described galaxy G29 separately in terms of a spherical (model M9) or elliptical (model M10) dPIE mass density profile. We also tested a final model, M11, characterized by three cluster scale dark matter haloes, which, despite the values of $\Delta_{\rm rms}$ and log-evidence, can be discarded as well. Indeed, similarly to model M6, the second dark matter halo is predicted to lie in the same region $\sim 50''$ north-west to the BCG, with a velocity dispersion still

consistent with that of a typical member galaxy. The third halo is $\sim 21''$ north-west to the BCG, again in a region with no observed cluster members. Hence, according to the figures of merit adopted, M9 stands out as the best-fit model: it is the most physically plausible model and can be considered as the reference one of this Thesis. We decided to keep in the analyses those models predicting extended dark matter halos centred on observed galaxies despite the possibility of having substructures potentially not associated with light (see Chap. 3).

Model M9 is characterized by a precision of $\Delta_{\rm rms} = 0.32''$ in reproducing the observed positions of the 35 multiple images used to build the lens models. The model-predicted positions of the multiple images are shown as green boxes in Fig. 4.9, which displays the observed spectroscopically-confirmed (photometric) images as magenta (yellow) circles. Fig. 4.9 also shows the critical lines evaluated at the redshift of families 3, 31, and 32, at $z = 4.048$, namely, the multiple-image systems lying around G29. The bottom-right insert shows a zoom-in around this galaxy. The natural extension of the model would be to improve the number of constraints by modelling the surface brightness distribution of the arc where the above-mentioned families are observed. The marginalized posterior distributions of the free parameters included in model M9 are given in Fig. 4.13. The median value of $\sigma_{\rm ref}$, quoted in Table 4.6, is consistent with the value recovered by calibrating the Faber-Jackson relation with the kinematics data. In Fig. 4.7, the red solid curve is the relation obtained by considering the results of M9. Note the difference between the shaded areas: the light orange band represents the intrinsic scatter $\Delta\sigma_{\rm ap}$ around the relation, whereas the light red one is obtained by randomly extracting 300 values of $\sigma_{\rm ref}$ from the Markov chain Monte Carlo (MCMC) realizations for M9. Additionally, the best-fit value of the velocity dispersion of G29 is in very good agreement with our measurement (see Table 4.3). Interestingly, the values of the redshifts for families 8 and 11 are consistent with their tentative MUSE spectroscopic measurements.

4.3.1 Total mass distribution

We show in Fig. 4.10, for better visualization, the average cumulative projected total surface mass density profiles of the cluster as a function of the distance from the BCG for the reference model of this work, M9, in black, and for the other models explored. We find that the cumulative total mass profiles from the 11 parametrizations are in excellent agreement with each other. This is expected, since Meneghetti et al. (2017) showed that the total mass measured within the region where multiple images are observed is the quantity evaluated with better precision. We find a projected total mass value of $M(< 40 \text{ kpc}) = (1.40 \pm 0.01) \times 10^{13}\, M_{\odot}$ within the projected distance of the multiple images from the BCG at which we found the lowest uncertainty (refer to Fig. 4.11). The upper and lower limits represent the statistical uncertainty, evaluated as the 84th and 16th percentiles, respectively, estimated by generating 500 total mass profiles from 500 sets of parameters randomly extracted from the MCMC realizations of M9. Thanks to the exploration of the other models, we are able to quantify the systematic uncertainty arising from our modelling choices. We generate, for each model, including M9, 500 realizations of the total mass profile, similarly to the procedure followed for M9 only. The result, displaying the relative impact of statistical and systematic uncertainties, is shown in Fig. 4.11, where the blue (green) band corresponds to the interval [16th, 84th] percentiles associated with the total statistical+systematic (statistical only) uncertainty. As visible, the uncertainty budget on the cluster total mass is mainly dominated by systematic effects: the total systematic+statistical uncertainty (blue band) can be as large as 8% in the outermost SL region (where the most distant multiple images are observed),

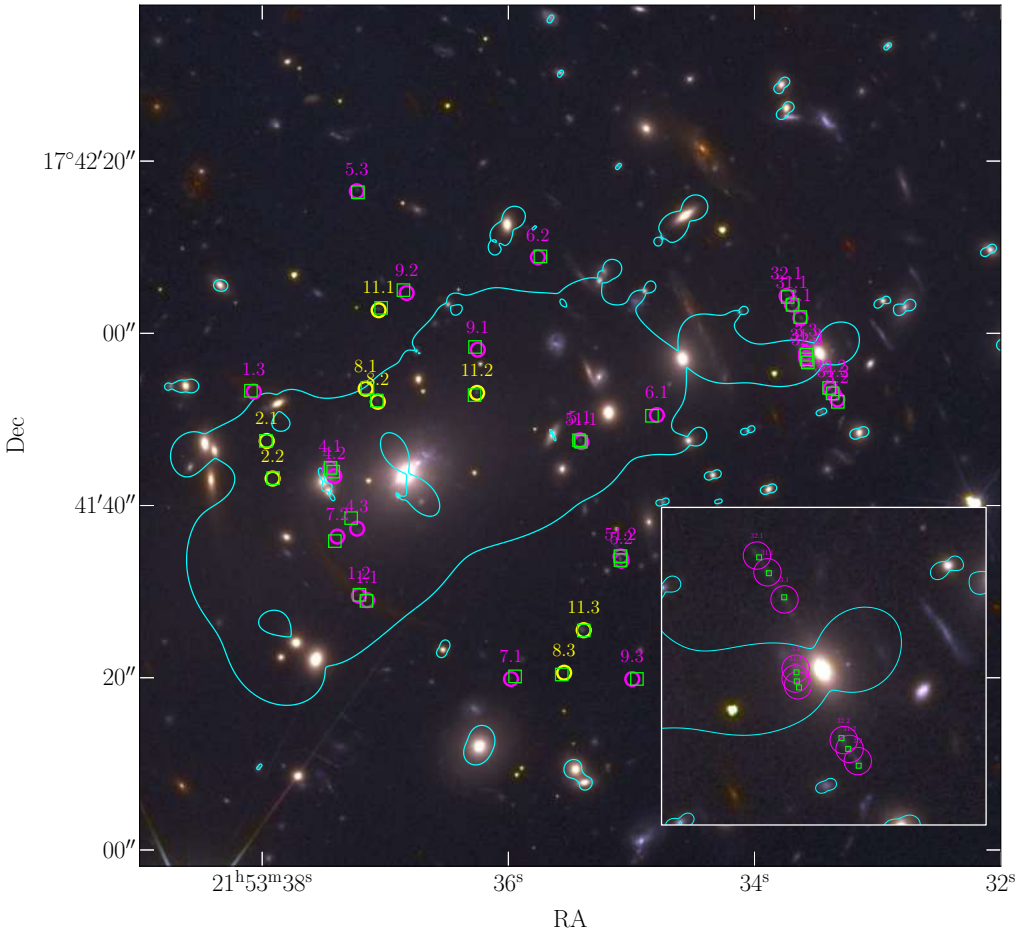

Figure 4.9: Colour-composite Euclid image (red: $H_{\rm E}$, green: $H_{\rm E}$+$I_{\rm E}$, blue: $I_{\rm E}$) of the galaxy cluster A2390 with overlaid in cyan the critical lines from the reference model M9 evaluated for a source at redshift $z_{\rm s}$ = 4.048 (families 3, 31, and 32). The spectroscopically-confirmed (and photometric) multiple images included in our analysis are also shown in magenta (and yellow, respectively). Green boxes denote the predictions of the reference model. From Abriola et al. (2025)

Table 4.6: Input and optimized parameter values of the reference lens model (M9) for the galaxy cluster A2390. The first column reports the mass component. The second column contains the parameters of the density profile used to describe the corresponding mass component. The third column shows the prior distributions adopted. When a flat prior on a free parameter value is considered, the boundaries of the prior separated by the $\div$ symbol are reported. In case of a Gaussian prior, the notation $a \pm b$ is adopted, with a the mean and b the standard deviation of the distribution, respectively. The x and y coordinates are measured with respect to the position of the BCG ($\mathrm{RA} = 328.4034183^{\circ}$, $\mathrm{Dec} = 17.6954744^{\circ}$, J2000.0). In the last column, we quote the median value, the 16th, and 84th percentiles of the marginalized posterior distribution (see Fig. 4.13).

Mass component	Free parameter	Prior	Posterior
Cluster halo	x_{DM} [arcsec]	0 ± 100	2.76 ± 0.08
	y_{DM} [arcsec]	0 ± 100	$1.20^{+0.06}_{-0.05}$
	q_{DM}	$0.25 \div 1.0$	0.73 ± 0.01
	θ_{DM} [rad]	$0 \div \pi$	1.1 ± 0.1
	σ_{DM} [km s^{-1}]	$500 \div 1500$	1195 ± 12
	$r_{\mathrm{core,DM}}$ [arcsec]	$0.01 \div 30.0$	16.7 ± 0.4
G29	σ_{G29} [km s^{-1}]	$50 \div 500$	233^{+5}_{-3}
	$r_{\mathrm{cut,G29}}$ [arcsec]	$0.05 \div 25.0$	$18.2^{+4.3}_{-4.1}$
External shear	$\lvert\gamma\rvert$	$0.0 \div 0.3$	0.17 ± 0.01
	θ_{γ} [rad]	$0 \div \pi$	2.22 ± 0.01
Scaling relations	σ_{ref} [km s^{-1}]	285 ± 41	288 ± 5
	$r_{\mathrm{cut,ref}}$ [arcsec]	$0.05 \div 30.0$	$16.1^{+1.3}_{-0.9}$

with the statistical one (green band) counting up to 0.8%. This systematic uncertainty was estimated by taking into account all the models studied, with no weighing applied according to their rms or evidence. Nevertheless, if we restrict to the best three models (according to these figures of merit), namely, models M6, M9, and M11, the systematic effects drastically reduce to roughly 1.5% (see the orange band in Fig. 4.11).

4.3.2 Comparison with weak lensing

To validate the results we obtained, we compared our work with the joint strong and weak lensing (WL) analysis first presented in Atek et al. (2024), and then developed in Schrabback et al. (2025) and Diego et al. (2025), obtained with the free-form software WSLAP+ (Diego et al. 2005, 2007), based on the same Euclid imaging. In addition to the observed positions of the multiple images, this analysis adopts as further observables to constrain the lens models the measured slight distortions induced by the gravitational potential of the deflector on the shape of background sources (see Bartelmann & Schneider 2001, for a nice overview on WL by galaxy clusters). Differently from ours, the study by Diego et al. (in prep.) relies on a free-form approach, and exploits a different set of multiple images to reconstruct the cluster total mass distribution. In addition, WSLAP+ relies on a source-plane approach, thus avoiding the inversion of the lens equation required in the other optimization schemes (see Section 3.2). Furthermore, being based on a free-form approach, the lens model presented by Diego et al. (2025) is given by a linear combination of a higher number of free parameters. In Fig. 4.12, we compare

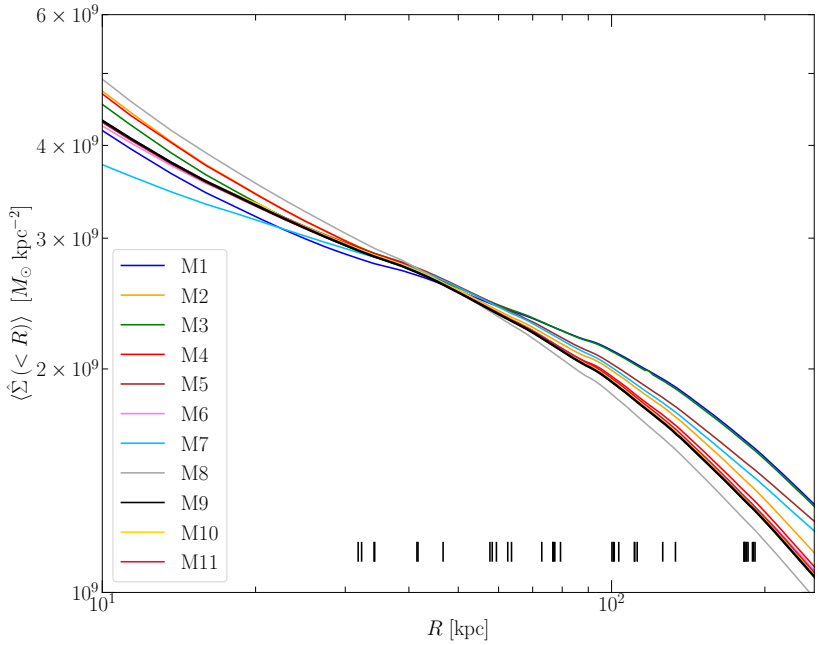

Figure 4.10: Average cumulative projected total surface mass density profile of A2390 from the reference (M9, in black) and the other models explored, as a function of the projected distance from the BCG. The vertical black lines in the bottom part of the plot are the projected distances from the BCG of the 35 multiple images included in our models. From Abriola et al. (2025)

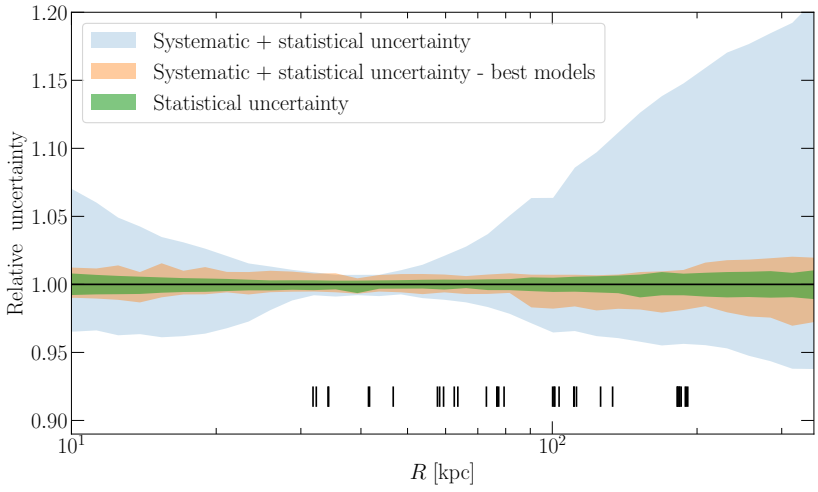

Figure 4.11: Relative statistical (green) and total systematic+statistical (blue and orange) uncertainty with respect to the cumulative total mass profile from the reference model. The total error is estimated by considering either all the 11 models explored (in blue) or the three best ones (in orange), according to the figures of merit adopted in this work, namely, M6, M9, and M11. From Abriola et al. (2025)

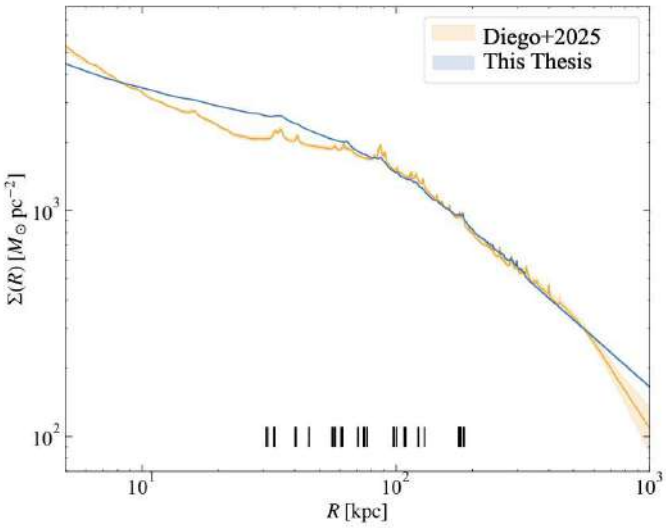

Figure 4.12: Surface mass density profile of A2390 as a function of the distance from the BCG. The blue (orange) solid line corresponds to this work (the lens model by Diego et al. (2025)). The light blue area is estimated from 300 random values of the profile obtained by randomly extracting sets of model parameters from the Bayesian Markov chain Monte Carlo realizations of the reference model of this work. The light orange area is estimated as described in Diego et al. (2025). The vertical black lines in the bottom part of the plot are the projected distances from the BCG of the 35 multiple images included in our models. Modified from Abriola et al. (2025)

the surface mass density profile obtained in our work (blue curve) with the results from Diego et al. (2025) (orange curve). For a fair comparison, we restrict to the region where multiple images (represented with black vertical lines) are observed. In the outer regions of the cluster, where no SL features are present, the extrapolation of our reference model becomes indeed less robust. We find a nice agreement in the region between approximately 60 kpc and 500 kpc from the BCG. The discrepancy observed between the two total surface mass density profiles in the innermost (few tens of kpc from the BCG) and outermost (few hundreds of kpc) regions may be ascribed to the lack of SL features, namely the multiple images. In particular, in the innermost SL regime, we think that the disagreement (which amounts up to 27%) can be mainly attributed to the different approach adopted to reconstruct the total mass distribution of the cluster. Indeed, since the study by Diego et al. (2025) includes also WL constraints, these inevitably affect the result in the SL region as well. As stated in Chap. 3, Meneghetti et al. (2017) have found that parametric models are generally more accurate and precise in reconstructing the projected total mass density of a lens cluster, as long as NFW density profiles represent well the outcomes of cosmological simulations.

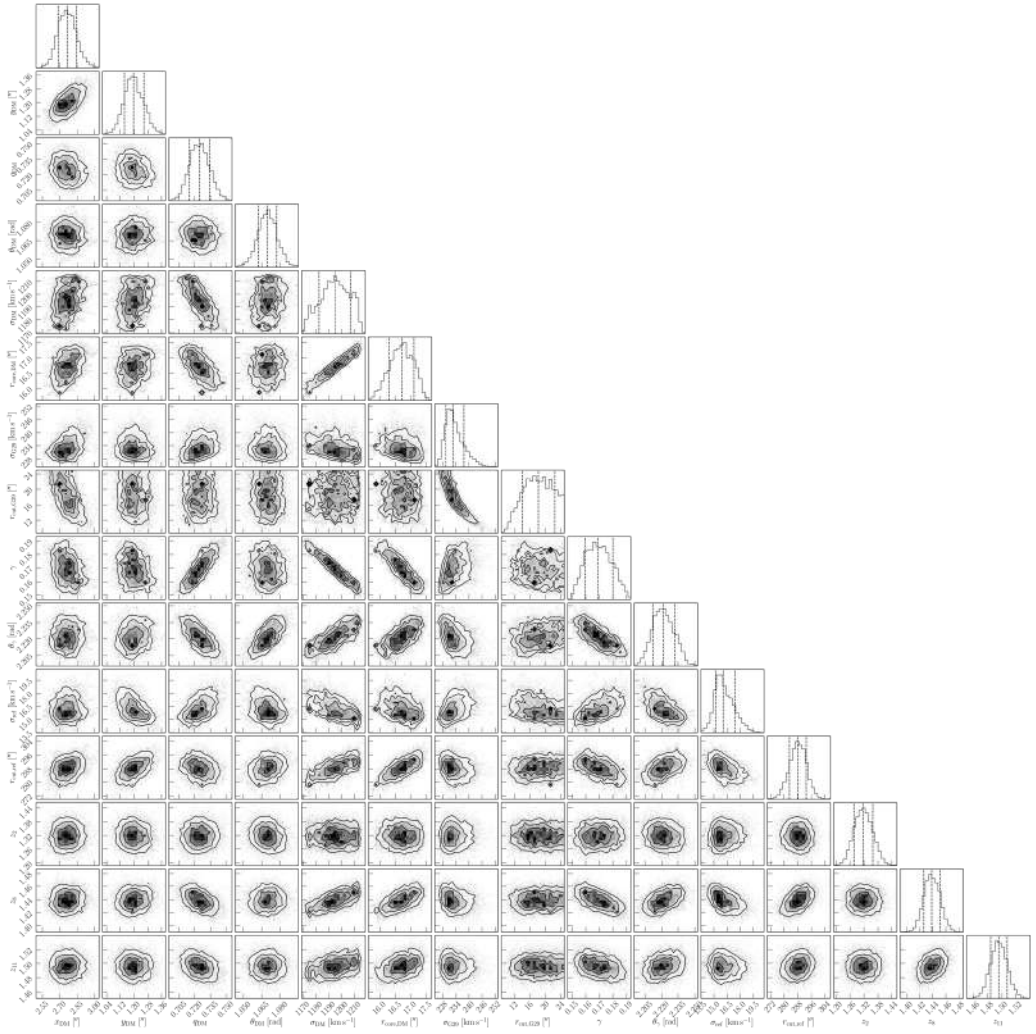

Figure 4.13: Marginalized posterior distributions of the parameters of the reference model of this work, M9. The 16th, 50th and 84th percentiles of the marginalized distributions are shown as vertical dashed lines. From Abriola et al. (2025)

CHAPTER 5

Strong lensing in the *Euclid* era: a statistical approach

As anticipated, the number of galaxy clusters displaying SL features is expected to increase significantly from the few tens of currently known lens clusters thanks to current and planned surveys, including the EWS with the *Euclid* telescope and the upcoming Legacy Survey of Space and Time (LSST, Ivezić et al. 2019) at the Vera Rubin observatory. Thousands of galaxy-scale SL events in galaxy clusters are expected to be observed within the LSST. All of them will be monitored with a cadence of a few days to a few weeks, enabling the detailed study of lensed transients, which represent a crucial tool for probing cosmology. Nevertheless, with respect to high-precision observations with the James Webb Space Telescope (JWST) and ERO-like observations (like Abell 2390, see Chap. 4 and Abriola et al., sub., Diego et al., in prep., and Shrabback et al., in prep.), a typical *Euclid*-like cluster will be characterized by wider but shallower imaging, resulting in the detection of less families of multiple images and cluster members, as well as the potential lack of spectroscopic follow-up, which is a crucial ingredient to securely confirm multiple images and hence build robust SL models. Complementarily, the absence of spectroscopic coverage will prevent the measurement of the line-of-sight stellar velocity dispersions for the brightest cluster members, which has been shown to reduce degeneracies between the different cluster mass components. Furthermore, in case no X-ray information would be available, it will not be possible to properly disentangle between the baryonic (cluster members, hot gas) and non-baryonic (dark matter) cluster components, resulting in a less robust dark matter distribution reconstruction (Bonamigo et al. 2017, 2018). These issues will impact lensing-derived quantities of interest, including the total mass and the magnification maps, which are fundamental for SL applications.

These motivations led us to explore and quantify the impact these limitations will have on future SL studies, specifically the limited number of multiple images detectable and the absence of the spectroscopic confirmation of multiple images. We face this issue by means of a statistical approach, by optimizing different lens models of a specific galaxy cluster with a varying number of constraints. To do so, we consider the lens galaxy cluster Abell S1063 (hereafter A1063, redshift $z = 0.348$), chosen due to its rather regular morphology. A1063 was first identified by Abell et al. (1989), and, despite its regular shape, it appears to have recently undergone an off-axis merger, as claimed by Gómez et al. (2012) and Rahaman et al. (2021) using X-ray data, and by Mercurio et al. (2021) from the dynamics of its members. The cluster is a bright X-ray source, with luminosity $L_X \sim 2.5 \times 10^{45}\,\mathrm{erg\,s^{-1}}$ in the $0.1 - 2.4$ keV band (Rahaman et al. 2021). It was also identified as RXJ 2248.7-4431 in the ROSAT All-Sky Survey (De Grandi et al. 1999; Guzzo et al. 1999).

5.1 Imaging and spectroscopy

A1063 was observed with HST in 16 broad band filters, from UV to near-IR, as part of the CLASH and CLASH-VLT programs (see Sect. 2.5.1). The HFF survey provided further imaging data by adding deep exposures in seven HST filters (F435, F606W, F814W, F105W, F125W, F140W, and F160W). A colour-composite HST image of the galaxy cluster is displayed in Fig. 5.1. As far as spectroscopy is concerned, A1063 was targeted with MUSE in the nights of June 25th, 2014 and June 29th, 2014. MUSE data consist of two pointings (Karman et al. 2015, 2017). The south west pointing (ID 60.A-9345, P.I.: K. Caputi and C. Grillo) was characterized by an exposure of 3.1 hours and a seeing of $\approx 1.1''$, while the north east pointing (ID 095.A-0653, P.I.: K. Caputi) had an exposure of 4.8 hours and seeing of $0.9''$. The cluster was also one of the targets of the CLASH-VLT Large Program spectroscopic campaign with the VIsible Multi Object Spectrograph (VIMOS) spectrograph, which yielded more than 4,000 redshifts over an area of $\sim 25 \times 25\,\mathrm{arcmin}^2$. These data allowed for the identification of approximately over 1,200 cluster members (Mercurio et al. 2021).

5.2 Methodology

To face the issues mentioned above, we adopted the following statistical approach. We started from the reference lens model presented in Bergamini et al. (2019), hereafter B19. This lens model is characterized by the inclusion of 222 cluster members and 55 spectroscopically confirmed multiple images, corresponding to 20 background sources (see also Caminha et al. 2016; Bonamigo et al. 2018). With respect to the model in B19, we simplify the total mass parametrization (see later for a more detailed description), and adopt different sets of multiple images for each lens model we built. Once again, the optimization is performed with `Gravity.jl`, and all the models explored are studied in the simplified image-plane configuration scheme.

5.2.1 Total mass parametrization

We adopt the same total mass parametrization of B19, but, in order to simplify the analysis and simulate a realistic scenario, we do not include the contribution of the ICM. Thus, our mass parametrizations are constituted only by the extended dark matter halos and the galaxy-scale mass components.

Extended dark matter halos

As in B19, we introduce two extended cluster-scale halos to describe the distribution of dark matter in the galaxy cluster, the main and the secondary halos. The main one (DM1) is modelled with a dPIE density profile, which, as discussed in the previous Chapter, is characterized by six free parameters: the position on the sky (x, y), the axis ratio q, the position angle θ, the central velocity dispersion $\sigma_{\rm v}$, and the core radius $r_{\rm c}$. To mimic an isothermal behaviour at large radii, we set the truncation radius equal to 2×10^3 arcsec. Vice versa, the secondary dark matter halo (DM2) is modelled in terms of a spherical dPIE mass density profile, and, as such, is described in terms of just three free parameters: the position in the sky and the central velocity dispersion. Also in this case, we fix the truncation radius equal to 2×10^3 arcsec. For the parameters of the two extended halos are the same as in B19.

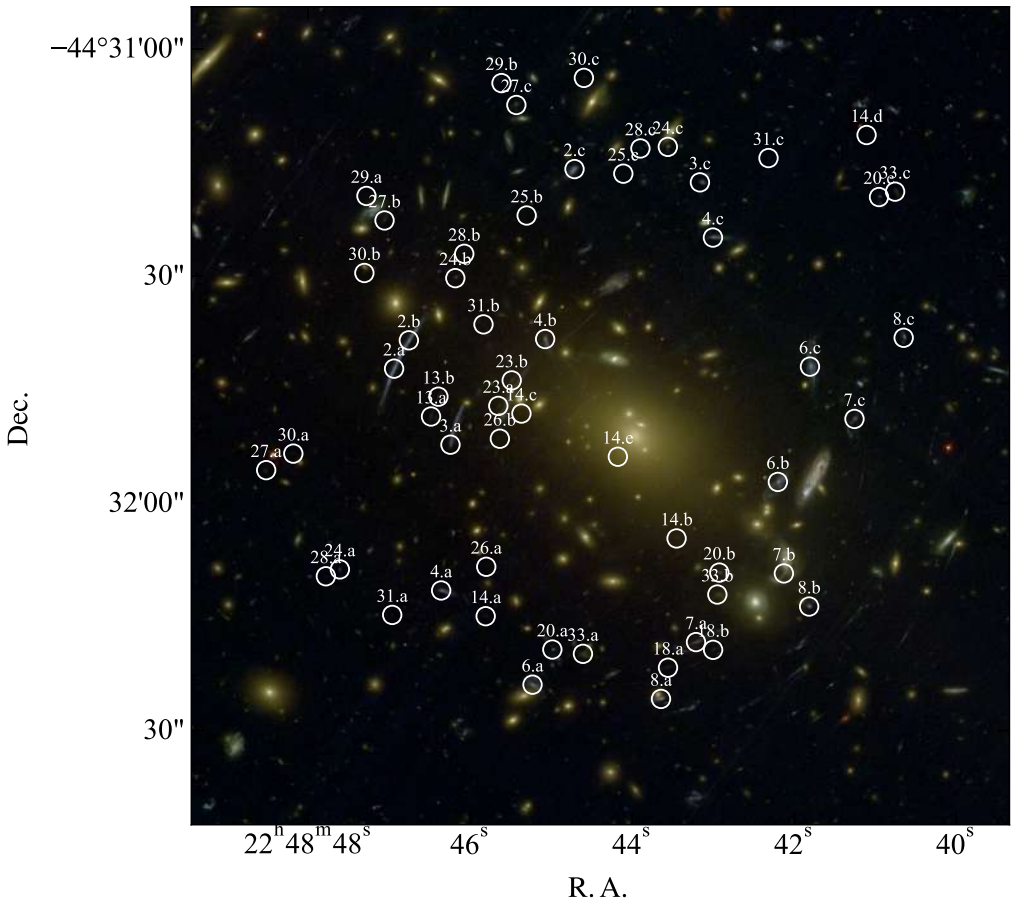

Figure 5.1: Color-composite HST image of the galaxy cluster Abell S1063. The multiple images considered in this work are displayed with white circles: each of them is named according to the nomenclature of Bergamini et al. (2019).

Cluster members

We include in our models all the 222 cluster members used in B19. The galaxies are modelled in terms of spherical dPIE profiles, with the core fixed to $0.05''$. We adopt the same scaling relations given by Eq. (3.44) and Eq. (3.45): the central velocity dispersion $\sigma_{\mathrm{gal},j}$ and the truncation radius $\sigma_{\mathrm{t},j}$ of the j-th cluster member scale with its luminosity L_j, according to

$$\sigma_{\mathrm{gal},j} = \sigma_{\mathrm{ref}} \left(\frac{L_j}{L_0} \right)^{\alpha} , \tag{5.1}$$

and

$$r_{\mathrm{cut},j} = r_{\mathrm{cut,ref}} \left(\frac{L_j}{L_0} \right)^{\beta} , \tag{5.2}$$

with L_0 a reference luminosity, chosen to be that of the brightest cluster galaxy (BCG). As in B19, we adopt the HST/F160W Kron magnitudes in the above scaling relations. The Kron magnitude of the BCG in this band is $m_{\mathrm{ref}}^{F160W} = 16.18$. Based on the galaxy kinematics measurements for 37 out of 222 cluster members presented in B19, we fix $\alpha = 0.27$. We determine the value of β assuming a scaling relation between the total mass $M_{\mathrm{tot},j}$ of the j-th cluster member and its luminosity $M_{\mathrm{tot},j}/L_j \propto L_j^{\gamma}$, with $\gamma = 0.2$ to be consistent with the observed Fundamental Plane relation. Since for the dPIE total mass profile $M_{\mathrm{tot},j} \propto \sigma_{\mathrm{gal},j}^2 \, r_{\mathrm{cut},j}$, we derive

$$\beta = \gamma - 2\alpha + 1 \, , \tag{5.3}$$

which then implies $\beta = 0.66$. Differently from B19, in order to simulate the potential lack of spectroscopic follow-up and hence the impossibility of measuring the stellar kinematics for a subset of cluster members, we do not take advantage of the calibrated Faber-Jackson relation (see Eq. 3.47). Thus, we do not impose the same Gaussian prior on σ_{ref} as in B19, but rather opt for an uninformative uniform probability distribution on that parameter. Similarly, a uniform prior is imposed for $r_{\mathrm{cut,ref}}$.

5.2.2 Multiple images

The original model of B19 includes 55 spectroscopically-confirmed multiple images, corresponding to 20 background sources, distributed over a wide range of redshifts, from $z = 0.73$ to $z = 6.11$. In our work, we build and explore 400 lens models of A1063, characterized by the same total mass parametrization described in the previous section, but a different number of multiple images, as follows.

Models 5f We build 100 lens models by including in each of them a randomly extracted subset of 5 out of 20 families of multiple images. This results in lens models having the same number of background sources being lensed, but a different number of multiple images.

Models 5f-1h. As before, we explore 100 lens models by including in each of them a randomly extracted subset of 5 out of 20 families of multiple images. Differently from the previous ensamble of models, in this case we modify the total mass distribution: as a matter of fact, we include only the main dark matter halo, and exclude the secondary one. These models are built in correspondence with those with two halos: namely, each set of multiple images is included both in a model with one and two cluster-scale halos.

Models 10f. Similarly, we build 100 lens models by including in each of them a randomly extracted subset of 10 out of 20 families of multiple images. For these models, we include two dark matter haloes in the parametrisation of the total mass distribution.

Models 15f. Finally, we optimize 100 lens models obtained by including in each of them a randomly extracted subset of 15 out of 20 families of multiple images. For these models, we include two dark matter haloes in the parametrisation of the total mass distribution.

A brief description of the main specifics of each of these lens models is given in Table 5.1. All multiple images are treated as point-like sources. To each of them we assigned the same measurement uncertainty of the best model in B19, namely $\sim 0.48''$. Each image is given its spectroscopic redshift presented in B19.

Table 5.1: Brief description of the lens models explored. For each column, we report the number of background sources included $N_{\rm src}$, the average number of multiple images included $\bar{N}_{\rm imgs}$, and the number of free parameters $N_{\rm par}$.

Model	$N_{\rm src}$	$\bar{N}_{\rm imgs}$	$N_{\rm par}$
5f	5	14.06	11
5f-1h	5	14.06	8
10f	10	27.54	11
15f	15	41.14	11

5.3 Results

In this Section we summarize the main results of this study: we first analyse the figures of merit adopted to quantify the goodness of the lens models, then we explore the impact of the reduced number of multiple images on the lens parameters, the total mass distribution of the cluster, and the magnification maps.

5.3.1 Figures of merit

As done for the analysis of Abell 2390, we adopt as figure of merit the mean scatter between the model-predicted and observed multiple images, namely the rms. However, since the models are characterized by a different number of multiple images (and a different total mass parametrization in case of models 5f-1h), we compute instead a *reduced* rms, given by

$$\begin{aligned}\Delta_{\rm rms,RED} &= \sqrt{\frac{1}{N_{\rm im}-N_{\rm src}-N_{\rm dof}/2}\sum_{i=1}^{N_{\rm im}}\left|\boldsymbol{\Delta}_i\right|^2} = \\ &= \sqrt{\frac{1}{N_{\rm im}-N_{\rm src}-N_{\rm dof}/2}\sum_{i=1}^{N_{\rm im}}\left|\boldsymbol{x}_i^{\rm ob}-\boldsymbol{x}_i^{\rm pr}\right|^2}\,,\end{aligned} \tag{5.4}$$

where $N_{\rm im}$ is the number of images, $N_{\rm src}$ the number of corresponding sources, and $N_{\rm dof}$ is the number of degrees of freedom for each model of each class. $\Delta_{\rm rms,RED}$ is related to

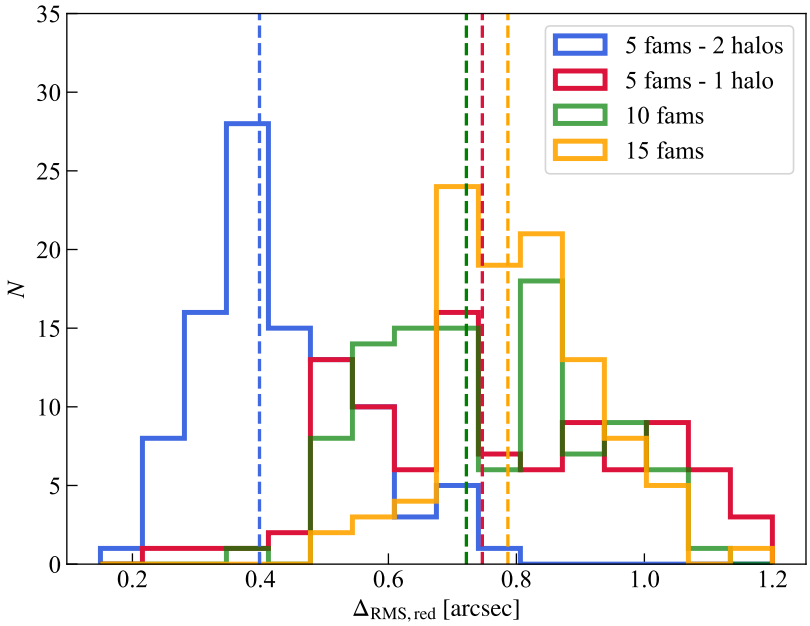

Figure 5.2: The *reduced* rms $\Delta_{\mathrm{RMS,red}}$ distribution for the models 5f (blue), 5f-1h (red), 10f (green), and 15f (orange). The vertical dashed lines indicate the median value of the corresponding distribution.

the definition of the rms Δ_{rms} given in Eq. (3.18) through

$$\Delta_{\mathrm{rms,RED}} = \Delta_{\mathrm{rms}} \sqrt{\frac{N_{\mathrm{im}}}{N_{\mathrm{im}} - N_{\mathrm{src}} - N_{\mathrm{dof}}/2}} \,. \tag{5.5}$$

In Figure 5.2 we display the distribution of $\Delta_{\mathrm{RMS,red}}$ for the different models. The vertical dashed lines indicate (with the same colour correspondence) the median value of such distribution. Models 5f-1h have a broad distribution, ranging from 0.2 arcsec to approximately 1.2 arcsec. On the other hand, the class of models 5f, despite having the same constraints as models 5f-1h, is characterized by a narrower distribution, peaked at lower values (around ~ 0.4 arcsec). Models 10f and 15f have distributions peaked around $\sim 0.7 - 0.8$ arcsec, reflecting the higher number of constraints available. Models 5f and 5f-1h display a similarity in the distribution of their evidences, which, as mentioned in Chapter 3, is a key figure to compare different lens models within a Bayesian framework. Since for each same subset of 5 families of multiple images there is a model with both a single extender cluster-scale halo and two halos, we can compare the specific lens models. The distributions of the evidences overlap nicely, and there are no major differences in their ratio. Given Eq. (3.20), this suggests that, for each subset of multiple images, the models are equally good. A major difference in models 5f-1h and 5f is best appreciated when studying the lensing-derived quantities of interest.

Complementarily, we quantify the reduced χ^2, χ^2_{red}, which weights the χ^2 of each lens model according to the correspondent number of degrees of freedom. Given $N_{\mathrm{dof},i}$

the number of degrees of freedom for the ith model, its χ^2_i is given by

$$\chi^2_i = \sum_{j=1}^{N^i_{\rm imgs}} \left(\frac{\boldsymbol{x}^{\rm ob}_{j,i} - \boldsymbol{x}^{\rm pr}_{j,i}}{\sigma_{j,i}} \right)^2 , \tag{5.6}$$

where $N^i_{\rm imgs}$ is the number of multiple images included in model i, $\boldsymbol{x}^{\rm ob}_{j,i}$ ($\boldsymbol{x}^{\rm pr}_{j,i}$) is the observed (model-predicted) position of the jth image, and $\sigma_{j,i}$ the uncertainty on its position. Hence, $\chi^2_{\rm red}$ can be evaluated as

$$\chi^2_{{\rm red},i} = \frac{\chi^2}{N_{{\rm dof},i}} . \tag{5.7}$$

We plot in Figure 5.3 the distributions of the reduced $\chi^2_{\rm red}$ for the different classes of models. The vertical dashed lines indicate the median value of the corresponding distribution. The distribution corresponding to models 5f-1h (orange histogram) is broad over a vast range of values. The other classes of models (5f, 10f, and 15f), having the same total mass parametrization, show more compact distributions, which shrink as more constraints are added, with median values consistent with one another. As can be seen, the majority of the models in these three classes is characterized by a reduced chi square less than the unity, implying an overestimate of the position uncertainty of the multiple images. This can be easily explained by considering that we adopted the same measurement errors of the reference model by B19, which is based on the complete set of 55 multiple images. In addition, in the best-fit model of B19, the measurement uncertainties had been already properly scaled as to achieve a chi square similar to the number of degrees of freedom.

5.3.2 Lens parameters

We then quantify the goodness of the lens models by studying the marginalized posterior distributions (pdf's) of the lens parameters for each model. These curves are displayed in Figure 5.4, 5.5, 5.6, and 5.7. In each plot, the coloured curves correspond to a specific model, and curves of the same colour belong to the same set: 5f-1h (red), 5f (blue), 10f (green), or 15f (orange). To make a first qualitative comparison with the reference scenario, each panel contains the marginalized pdf of the corresponding parameter of the complete model in black. It is evident how the curves tend to shrink as we add more constraints, resulting in more precise results. In addition, they tend to get closer to the black reference curve, suggesting more precise optimizations.
More in detail, as far as the scaling relations are concerned, it is evident how the reference truncation radius is not properly constrained: the systematics reflect the multimodality observed in the marginalized pdfs (first row of Figure 5.4). Indeed, for all the classes of models, some pdfs were peaked at low values of this parameter, whereas others were peaked at higher values. This trend is evident especially in models 5f-1h and 5f, whereas the behaviour becomes less pronounced in the other sets of models. As we will show later, this impacts the recovered total mass distribution. Moreover, models with only 5 families of multiple images tend to prefer for the velocity dispersion of the scaling relations a value higher than the reference, despite no clear correlation with the core radius (i.e., a more or less compact mass distribution for the sub-halo components) is observed. When analysing the marginalized pdfs of the DM1 halo, we can observe how its position is the the least constrained, with models 5f-1h mostly preferring a position north-east of the reference scenario. We can see how some models, in particular, do not

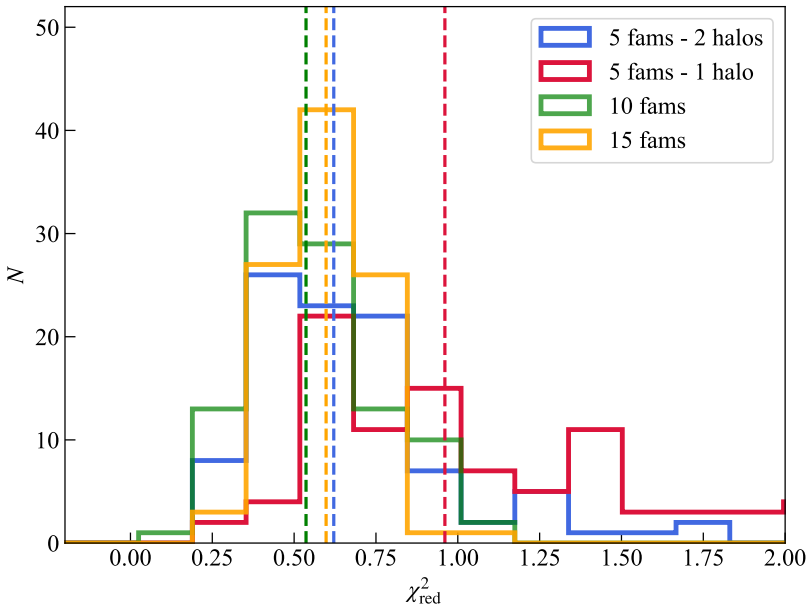

Figure 5.3: $\chi^2_{\rm red}$ distribution for the models 5f (blue), 5f-1h (red), 10f (green), and 15f (orange). The vertical dashed lines indicate the median value of the corresponding distribution.

show any preferred solution within the prior assigned. If we look at the second dark matter halo, DM2, it emerges how its position is badly constrained in the case of models 5f and, partly, 10f. This result motivated us in exploring the set 5f-1h, and is also evident in the reconstruction of the critical curves (see later).

We can then estimate the total statistical+systematic uncertainty associated with the various lens modelling choices (different total mass parametrizations, in the case of models 5f-1h with respect to the others, and/or the inclusion of different subsets of multiple images). To do so, we proceed as follows. For each parameter, we extract the best-fit values of the corresponding marginalized pdf for all the same set of 100 models, namely those maximizing the corresponding posterior distribution. Of these values, we extract the median value, and evaluate the interval corresponding to the [16th, 84th] quantiles. The result of these evaluations is given in Table 5.2. For a first quantitative analysis, we also quote the median values resulting from 100 random extractions of the Markov Chain Monte Carlo of the reference model. Each value of the last column is accompanied by the statistical uncertainty on the corresponding parameter estimated on those 100 extractions. It is clear how the systematic uncertainty reduces when passing from models 5f-1h to 15f, as more information is added. Models 5f-1h are characterized by a mean relative uncertainty of $\sim 79\%$, which, as emerges from Table 5.2, is mainly dominated by the uncertainty on the position of the cluster halo DM1. Indeed, if we neglect these parameters, the median error drops to $\sim 13\%$. The mean uncertainty reduces to 46% in the models 5f, and 21% if we exclude the uncertainty on the postion of the first dark matter halo. In this case, the total error budget is dominated by the uncertainty on the parameters of the second extended halo. Models 10f are characterized by a mean uncertainty of 20%, which further reduces to 8% for models 15f. The results of the different

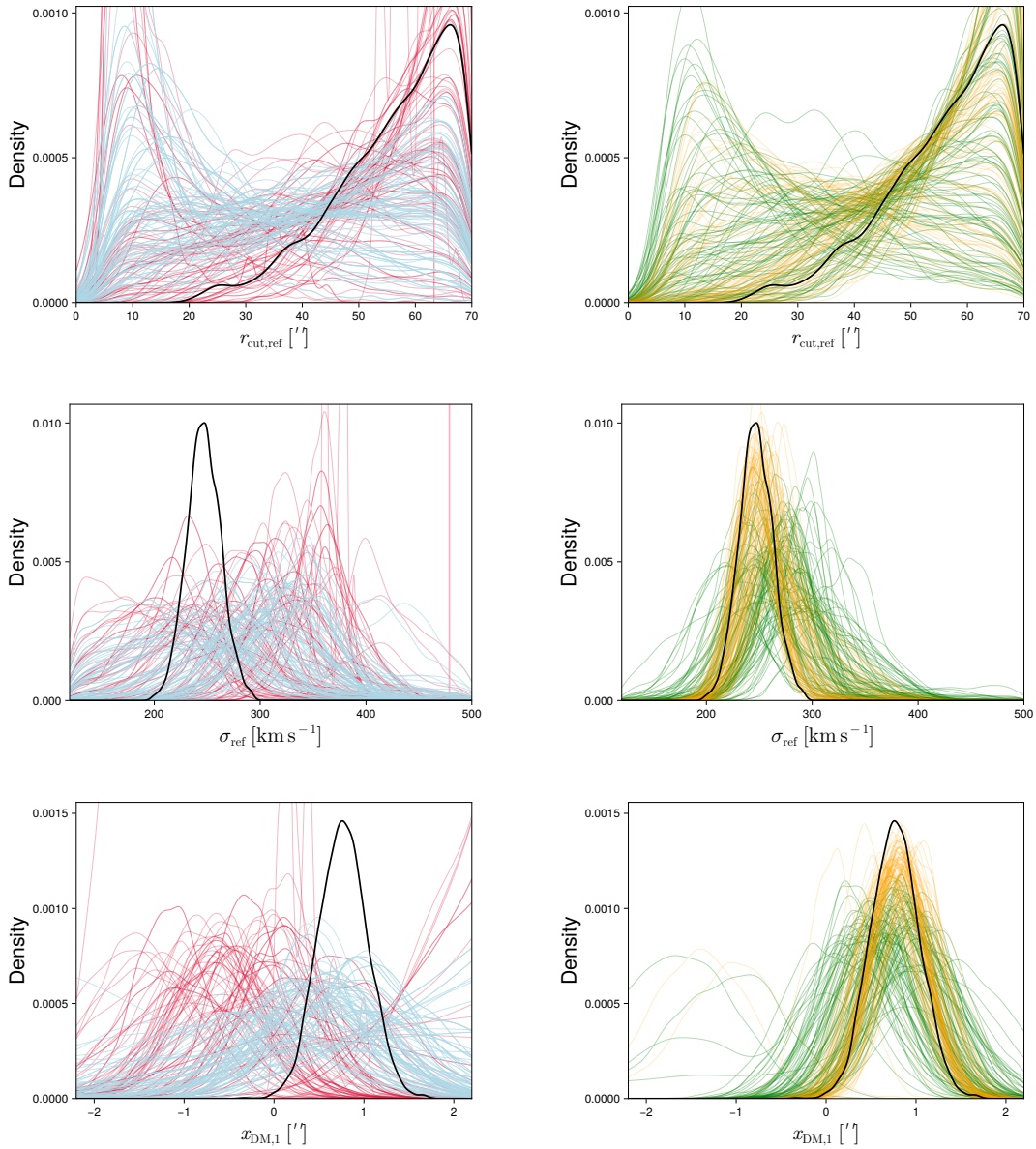

Figure 5.4: Marginalized posterior distributions of the parameters of the lens models for all the sets of models explored: models 5f-1h (red) and 5f (blue) in the left column, models 10f (green) and 15f (orange) in the right column. The black curves denote the marginalized posterior distributions for the reference model.

sets of models are globally consistent with each other, suggesting a robust lens model.

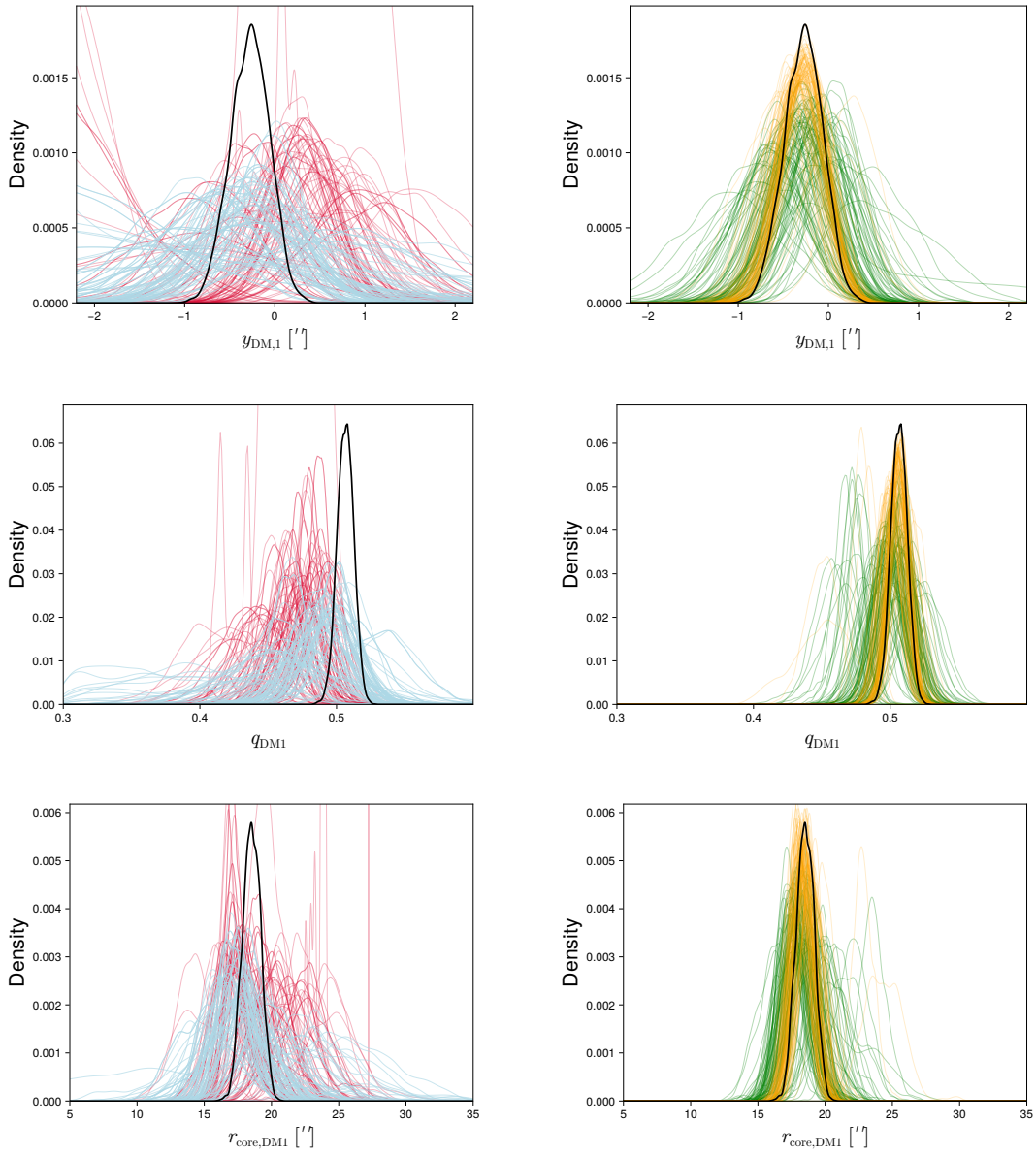

Figure 5.5: Continued.

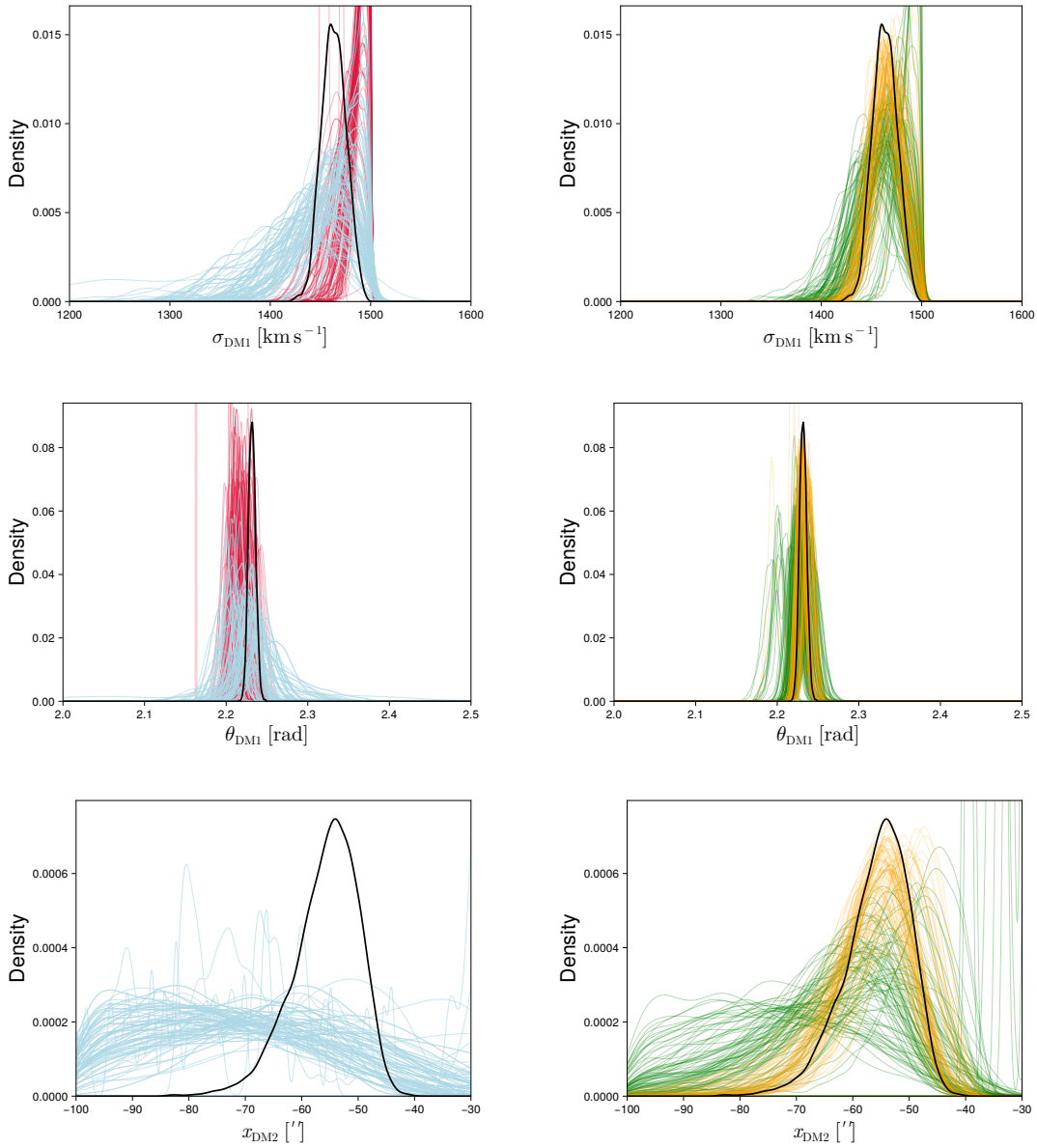

Figure 5.6: Continued.

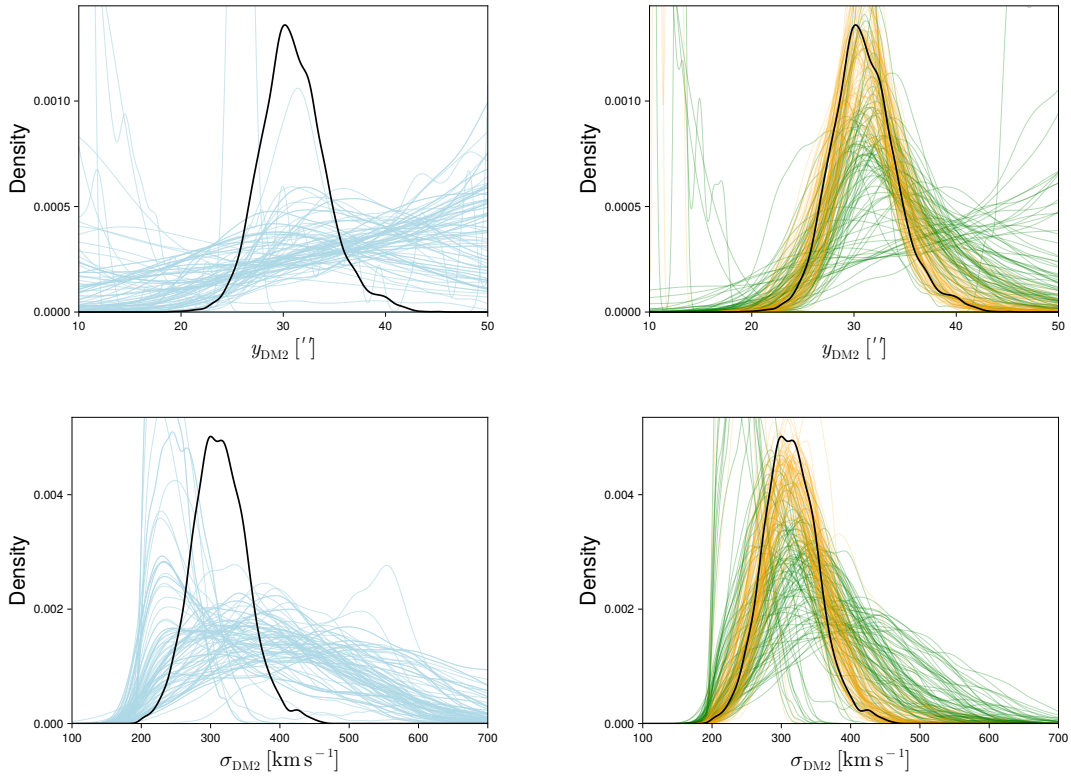

Figure 5.7: Continued.

Table 5.2: Optimized lens parameters and the corresponding systematic uncertainty for models 5f-1h (third column), 5f (fourth), 10f (fifth), and 15f (sixth). The last column displays the expected value from the reference model with the statistical uncertainty. For columns 2 to 6, the first uncertainty refers to the statistical one, the second error is the systematic one.

	Parameter	5f-1h	5f	10f	15f	Reference*
Galaxies	$\sigma_{\rm ref}$ [km s^{-1}]	$293 \pm 18 \pm 90$	$291 \pm 25 \pm 75$	$269 \pm 22 \pm 34$	$256 \pm 17 \pm 19$	245 ± 14
	$r_{\rm cut,ref}$ [arcsec]	$48.9 \pm 7.7 \pm 27.3$	$37.9 \pm 12.3 \pm 20.4$	$47.4 \pm 10.0 \pm 21.4$	$53.9 \pm 7.8 \pm 19.4$	59.0 ± 10.3
DM1	x [arcsec]	$-0.29 \pm 0.28 \pm 1.15$	$0.58 \pm 0.74 \pm 0.88$	$0.69 \pm 0.33 \pm 0.43$	$0.79 \pm 0.21 \pm 0.19$	0.82 ± 0.25
	y [arcsec]	$0.20 \pm 0.15 \pm 1.08$	$-0.35 \pm 0.51 \pm 0.85$	$-0.29 \pm 0.21 \pm 0.40$	$-0.31 \pm 0.17 \pm 0.12$	-0.34 ± 0.21
	σ [km s^{-1}]	$1489 \pm 10 \pm 11$	$1455 \pm 27 \pm 26$	$1464 \pm 18 \pm 15$	$1466 \pm 14 \pm 9$	1465 ± 14
	q	$0.47 \pm 0.01 \pm 0.03$	$0.49 \pm 0.02 \pm 0.03$	$0.50 \pm 0.01 \pm 0.01$	$0.51 \pm 0.01 \pm 0.01$	0.50 ± 0.01
	θ [rad]	$2.22 \pm 0.02 \pm 0.02$	$2.23 \pm 0.01 \pm 0.02$	$2.23 \pm 0.01 \pm 0.02$	$2.23 \pm 0.01 \pm 0.01$	2.22 ± 0.01
	$r_{\rm core}$ [arcsec]	$18.9 \pm 0.3 \pm 3.6$	$17.9 \pm 1.3 \pm 2.4$	$18.3 \pm 0.7 \pm 1.3$	$18.4 \pm 0.6 \pm 0.7$	18.5 ± 0.6
DM2	x [arcsec]	–	$-65.70 \pm 13.45 \pm 51.99$	$-59.33 \pm 10.51 \pm 12.99$	$-55.24 \pm 7.30 \pm 3.63$	-56.87 ± 5.58
	y [arcsec]	–	$38.01 \pm 11.04 \pm 32.82$	$33.00 \pm 8.42 \pm 7.60$	$31.11 \pm 9.51 \pm 1.42$	30.78 ± 3.26
	σ [km s^{-1}]	–	$376 \pm 93 \pm 105$	$330 \pm 61 \pm 61$	$317 \pm 51 \pm 19$	312 ± 39

Notes. The uncertainty on the lens parameters of the reference model is statistical. It was estimated by randomly extracting 100 points from the Markov Chain, and quantifying the 16th and 84th quantiles.

5.3.3 Total mass distribution

In lensing analyses we are mainly interested in derived quantities, including the total mass distribution and the magnification maps. Hence, we first reconstruct the total mass distribution of A1063 for all the lens models explored, and estimate both the statistical and total statistical+systematic uncertainty following a methodology similar to what done for the single lens parameters. First, for each set, we reconstruct all the 100 cumulative total mass profiles, using for each of them the corresponding set of parameters maximizing the posterior distribution. We quantify the systematic uncertainty for each set by considering the interval corresponding to the [16th, 84th] quantiles. Then, to estimate the total systematic+statistic error, we proceed as follows: given a lens model, we randomly extract 100 sets of parameters from the Monte Carlo Markov chains, and for each of them we reconstruct the cumulative total mass profile. We repeat the same operation for all the 100 models of the same class. We can therefore estimate the total uncertainty by evaluating once again the interval corresponding to the [16th, 84th] quantiles. For each set, the total mass enclosed within a circle whose radius is the median distance of all the 55 multiple images from the BCG ($159\,\mathrm{kpc}$) is given in Table 5.3. The first uncertainty quoted refers to the statistical one, whereas the second error is the systematic one (after subtraction from the total error budget). As can be seen, all the values are consistent with each other and with the estimate obtained with the reference model.

Table 5.3: Total mass of Abell S1063 estimated for all the classes of models explored in this work, and the reference case. Each value corresponds to the total mass enclosed within a circle whose radius is the median distance of all the 55 multiple images from the BCG. The first uncertainty quoted refers to the statistical one, whereas the second error is the systematic one (see text).

Model	**Mass** $[10^{14}\,M_{\odot}]$
5f	$1.549 \pm 0.016 \pm 0.013$
5f-1h	$1.551 \pm 0.017 \pm 0.011$
10f	$1.558 \pm 0.010 \pm 0.008$
15f	$1.559 \pm 0.007 \pm 0.004$
Reference*	1.558 ± 0.006

Notes. The uncertainty on the total mass of the reference model is statistical. It was estimated by evaluating 100 total mass profiles obtained by randomly extracting 100 points from the Markov Chain, and then quantifying the 16th and 84th quantiles.

To better understand potential differences between the different sets of models, we estimate the relative uncertainty on the total mass and the ratio between the total mass profiles. The radial dependence of the relative uncertainty (estimated as the semi-difference between the 84th and 16th quantiles) is shown in Figure 5.8. As expected, for all the models, the error is at its lowest in the SL region defined by the presence of the multiple images (see the vertical bars in the Figure). In all scenarios, the uncertainty keeps below 2%, with the set of models 15f having the lowest uncertainty (below 1% in the SL regime). As less constraints are available (models 5f, 5f-1h, and 10f), the uncertainty arises. We show the ratios between the median cumulative total mass profiles of the different sets of models and the reference scenario in Figure 5.9. In the innermost SL region, differences are greater than few percent, as expected: indeed, that is a region

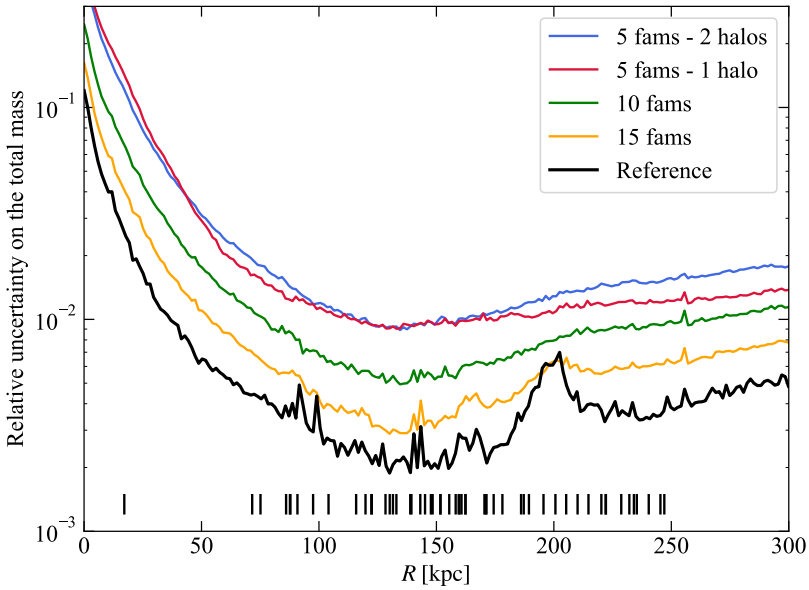

Figure 5.8: Relative uncertainty on the cumulative total mass distribution for the different sets of models explored in this Thesis as a function of the distance from the BCG. The vertical black bars denote the positions of the multiple images.

with no SL constraints, hence it is an extrapolation of the lens models. Models 5f-1h and 5f underestimate the total mass, as compared to the reference case. Complementarily, models 10f and 15f are in excellent agreement with the reference scenario. We explain this accordance since, by averaging over the spatial distribution of the multiple images in each of the 100 models per set, the SL region is properly sampled (on average, each 15f model has 41 multiple images over a total of 55). Since the position of the multiple images constrain the total mass enclosed within a sphere of that radius, the mass profiles result robustly reconstructed.

Dark matter mass distribution

We further explore how the total mass of the cluster is distributed between the dark matter and the baryonic components. Similarly to Figure 5.9, we display in Figure 5.10 the ratio between the the median cumulative DM-only mass profiles for the different classes of models and the reference case. Once again, models 15f predict values that are in excellent agreement with the reference case, despite a slight overestimate of the mass by $\sim 1\%$ in the innermost SL region. Models 10f also predict a systematically higher value of the DM mass distribution, by a factor of less than $\sim 2\%$. Models 5f systematically disagree with the reference case (with a difference of more than $\sim 4\%$ in the SL region). Finally, models 5f-1h underestimate the DM-only mass distribution by less than $\sim 2\%$. It is noteworthy to underline that all these reconstructed DM mass profiles are biased by the fact that the hot intracluster gas component has not been separately modelled, rather it is included in the DM-only mass budget (Bonamigo et al. 2017, 2018). Despite this, we can see in Figure 5.11 how the ratio DM-to-total mass for the different sets of models explored keeps consistent with the reference scenario. We notice a slight discrepancy for

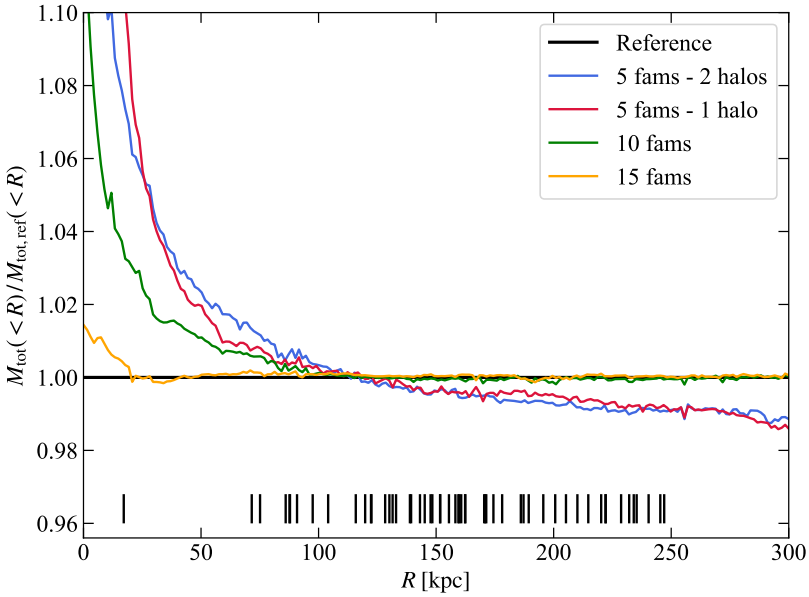

Figure 5.9: Ratio between the cumulative total mass profiles for the sets of models explored in this Thesis and the reference model, as a function of the distance from the BCG. The vertical black bars denote the positions of the multiple images.

models 5f-12h in the innermost SL region (less than 50 kpc from the BCG). As expected, models 5f-1h are characterized by a systematically higher (less than $\sim 1\%$) value of this fraction, due to the different total mass redistribution between the DM- and baryonic components.

5.3.4 Critical curves and magnification maps

Another lensing-derived quantity of interest are the critical curves, namely the set of points on the lens plane where the magnification factor ideally diverges. These lines are of crucial importance to search for and study faint or distant sources, which would not be detectable otherwise. We display in the left column of Figure 5.12 50 realizations of the critical curves estimated at the median value of the redshift distribution of the multiply-lensed sources, namely $z = 3.145$, obtained by randomly choosing half of the models for each subset. The top panel displays the critical curves for 50 lens models of the class 5f, the middle one refers to models 10f, whereas the bottom plot corresponds to models 15f. We exclude models 5f-1h being these characterized by a different total mass parametrization. In each panel, the blue crosses denote all the 55 multiple images included in the reference case, whereas the red ones are those included in one specific model of the corresponding set (namely, in the top panel the red crosses are the multiple images included in one of the lens models of the set 5f, and similarly for the other two panels). It is evident how the critical curves get better constrained as more and more observables are added. This is particularly evident for the north-east region, where, due to the lack of multiple images, the critical curves are not constrained at all in the 5f scenario, but are better reconstructed in the two other sets of models. The right column of Figure 5.12 displays instead the relative uncertainty on the magnification maps, estimated as follows.

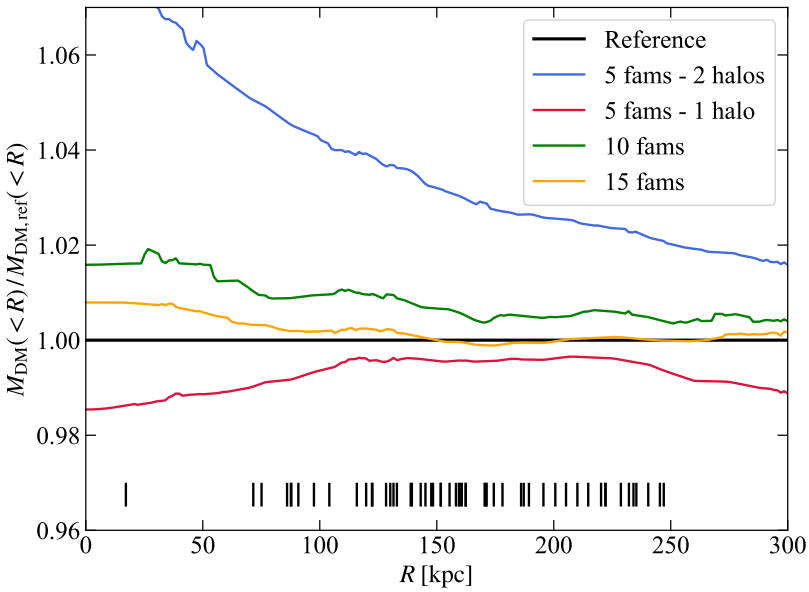

Figure 5.10: Ratio between the cumulative DM-only mass profiles for the sets of models explored in this work and the reference model, as a function of the distance from the BCG. The vertical black bars denote the positions of the multiple images.

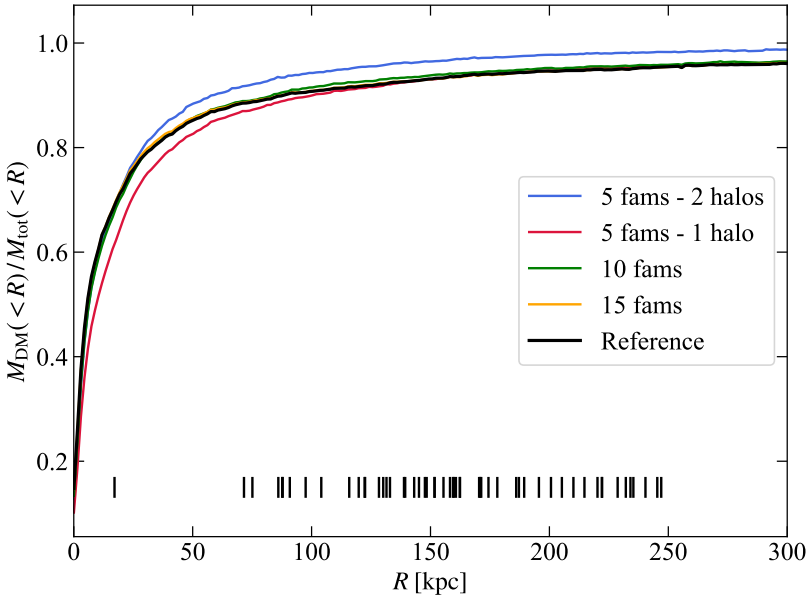

Figure 5.11: Radial profiles of the fraction of cumulative projected total mass in the diffuse halo components for the different sets of models explored in this work. The vertical black bars denote the positions of the multiple images.

For each set, we evaluate the magnification map at the same redshift $z = 3.145$ for all the 100 models using the corresponding set of best-fit values (namely, those maximizing the posterior distribution). We evaluate the median value in each pixel, whereas the uncertainty is once again estimated from the 16th and 84th percentiles of the magnification distributions in each pixel. It is evident how the uncertainty reduces as more constraints are added. This is particularly evident when passing from 5f to 10f, with the critical curves being better constrained. We can also visualize this in Figure 5.13, which displays the flattened distribution of the relative uncertainties shown in the right column of Figure 5.12. It is evident how the distributions shrink when passing from models 5f to models 10f and 15f. In addition, they get peaked at lower values of the relative uncertainty. This behaviour is also reflected in the flattened distribution of the relative uncertainties for those pixels having an absolute value of the magnification greater than 100, hence those hosting critical curves, displayed in Figure 5.14. The distribution for models 5f is characterized by a broad distribution with a high tail for uncertainties greater than 120%. Models 10f have instead relative uncertainties peaked at 100%, and a long tail for higher values. Finally, models 15f are peaked around 30%, despite a broad tail extending to higher values.

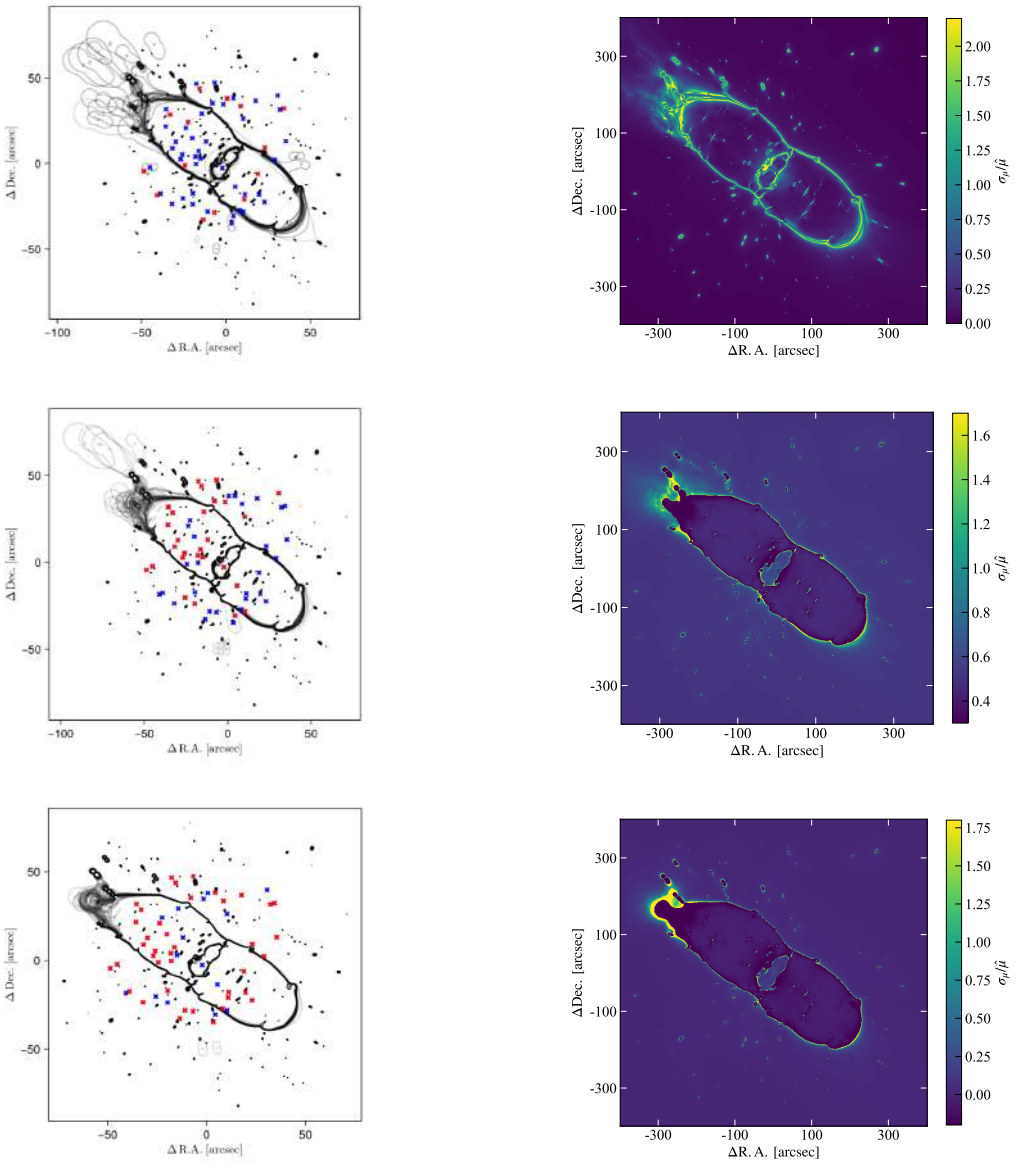

Figure 5.12: *Left*: 50 realizations of the critical curves estimated at the median value of the redshift distribution of the multiply-lensed sources ($z = 3.145$), obtained by randomly choosing half of the models for each subset. From top to bottom: models 5f, 10f, and 15f. The blue crosses denote all the 55 multiple images included in the reference case, whereas the red ones are those included in one specific model of the corresponding set. *Right*: relative uncertainty on the magnification maps. Similarly, from top to bottom: models 5f, 10f, and 15f.

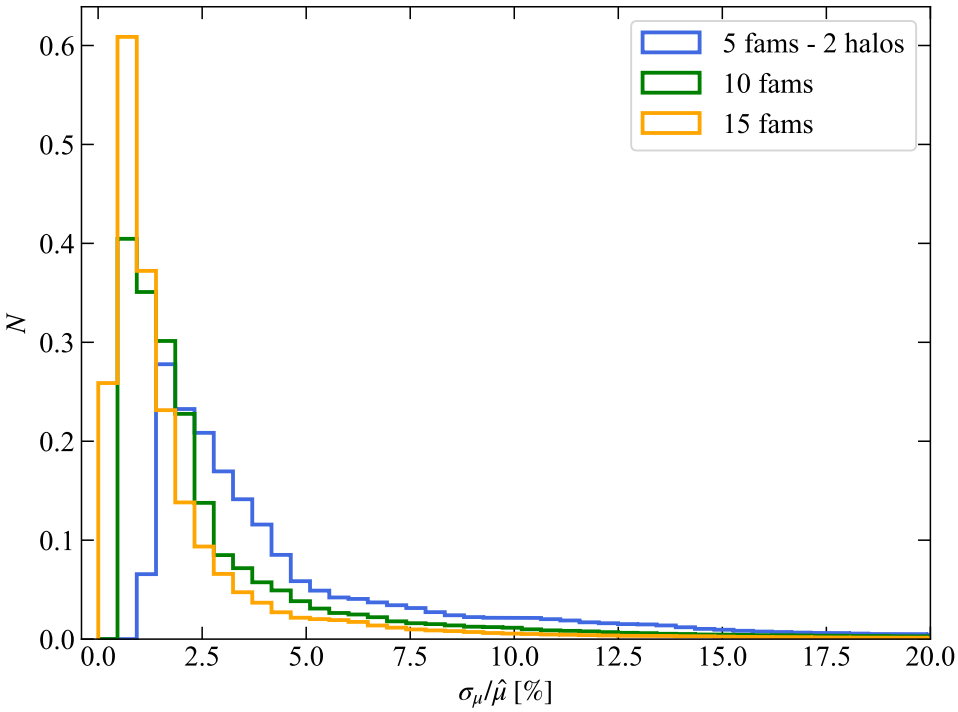

Figure 5.13: Distribution of the relative uncertainty on the magnification value μ. Each colour corresponds to a different set of lens models: 5f (blue), 10f (green), and 15 f(orange).

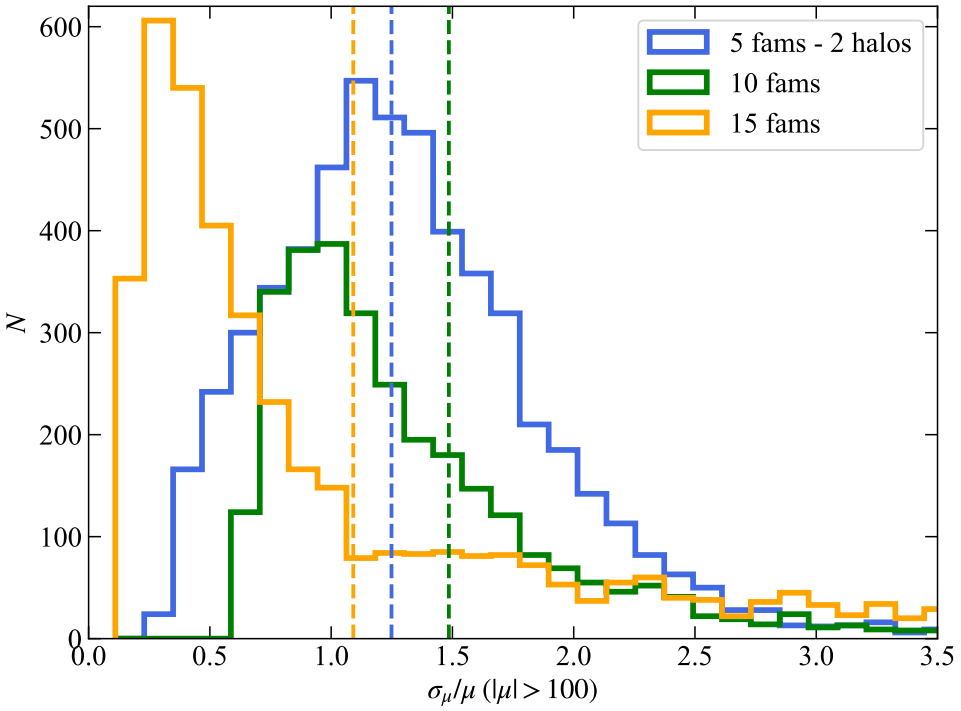

Figure 5.14: Distribution of the relative uncertainty on the magnification value μ for the pixels having $|\mu| > 100$ only. Each colour corresponds to a different set of lens models: 5f (blue), 10f (green), and 15 f(orange). The vertical dashed bar indicate the median value of the corresponding distribution.

Part III

Strong Lensing in the James Webb era

CHAPTER 6

SL analysis of MACS J0416.1−2403

As mentioned in the previous chapters, SL analyses and their applications rely on two key ingredients: imaging and spectroscopy. Having multi-band imaging enables the precise measurements of the position of cluster members and lensed sources, and the identification of multiple-image systems, based on their colours and morphologies. Until recent time, the state of art was represented by HST imaging, which operated in the optical wavelengths. A step forward has been made thanks to the launch of the James Webb Space Telescope (JWST) in late 2021. Operating in the near-infrared, the JWST has indeed enabled to view objects too old, distant (up to $z \sim 14$, Carniani et al. 2024; Naidu et al. 2025), or faint for HST (Rigby et al. 2023). The telescope was designed to reach four main goals: to study the first stars and galaxies that formed in the Universe, to track the formation and evolution of galaxies, to shed new light on stars and planet formation, and to study planetary systems. The telescope is equipped with four instruments: NIRCam, NIRSpec, MIRI, and FGS-NIRISS. The Near IRfrared Camera (NIRCam, Rieke et al. 2003, 2005, 2023; Beichman et al. 2012) is a camera operating in the wavelength range from $0.6\,\mu\mathrm{m}$ to $5\,\mu\mathrm{m}$. It is composed of ten detector arrays, each of which having in turn an array of 2048×2048 pixels. The camera has a field of view (FoV) of 2.2×2.2 arcminutes, with an angular resolution of 0.07 arcseconds at $2\,\mu\mathrm{m}$. NIRCam is also equipped with coronagraphs for collecting data on exoplanets near stars. The Near INfrared Spectrograph (NIRSpec, Jakobsen et al. 2022; Böker et al. 2023) is a multi-object spectrograph operating in the same wavelength range of NIRCam within a FoV of 3.4×3.6 arcminutes, with a pixel scale of 0.1 arcsecond/pixel. It operates in four observing modes, including, among others, an integral field unit, with resolving powers of ~ 100, $\sim 1,000$, and $\sim 2,700$. The Fine Guidance Sensor and Near InfraRed Imager and Slitless Spectrograph (FGS-NIRISS Doyon et al. 2012, 2023) is an instrument which combines a fine guidance sensor, a near-infrared camera, and a slitless spectrograph. NIRISS was designed to provide near-infrared imaging in the wavelength range $0.8 - 5.0\,\mu\mathrm{m}$, covering, as NIRCam, a FoV of 2.2×2.2 arcminutes, with an angular resolution of 0.07 arcseconds. The instrument also performs wide-field (WFSS) and single-object slitless (SOSS) spectrography with the same FoV and angular resolution. The WFSS operates in the wavelength range $0.8 - 2.2\,\mu\mathrm{m}$ with a resolving power of 150 at wavelength $\lambda = 1.4\,\mu\mathrm{m}$, whereas the SOSS works in the wavelength range $0.6 - 2.8\,\mu\mathrm{m}$ with a resolving power of 700 at $\lambda = 1.4\,\mu\mathrm{m}$. Finally, the Mid-InfraRed Instrument (MIRI, Glasse et al. 2015; Wright et al. 2023) provides imaging and spectroscopic observing modes in the range $\sim 5 - 28\,\mu\mathrm{m}$.

Since its launch, the JWST has paved the way for a new generation of high-accuracy lens models, thanks to the unprecedented quality and high resolution provided by its instruments (see, e.g., Caminha et al. 2022b; Bergamini et al. 2023b; Furtak et al. 2023; Mahler et al. 2023; Diego et al. 2024a; Gledhill et al. 2024), which motivated the surveys

mentioned in Sect. 2.5.2, including the CANUCS survey, previously mentioned. Of the five clusters targeted, the survey observed the galaxy cluster MACS J0416.1−2403.

MACS J0416.1−2403, hereafter M0416, is a massive galaxy cluster lying at redshift $z = 0.397$ which was discovered as part of the MACS survey (see Sect. 2.5.1). The system is a cluster merger, likely in a pre-collisional phase (Balestra et al. 2016), as reflected in its two-peaked X-ray surface brightness distribution (Mann & Ebeling 2012; Bonamigo et al. 2017, 2018). M0416 is a very effective gravitational lens, thanks to its elongated mass distribution, resulting in the production of an extremely high number of multiple images (Zitrin et al. 2013; Balestra et al. 2016; Hoag et al. 2016; Caminha et al. 2017; Bergamini et al. 2021; Diego et al. 2024b; Rihtaršič et al. 2025) and of high magnification transient events, that allowed for the study of stars at redshift $z \sim 1$ (Rodney et al. 2018; Chen et al. 2019; Kaurov et al. 2019; Yan et al. 2023; Diego et al. 2024b).

6.1 Previous lens models

After its discovery within the MACS campaign, M0416 was also observed within the CLASH and HFF surveys (see Sect. 2.5.1), which targeted the central core of the system, and helped to pave the way to the first strong lensing models of this cluster (Zitrin et al. 2013; Jauzac et al. 2015; Johnson et al. 2014; Diego et al. 2015; Kawamata et al. 2016; Sebesta et al. 2016). The cluster was also targeted by several spectroscopic follow-up observations, starting with the CLASH-VLT campaign. This led to the lens model by Grillo et al. (2015), comprising 30 spectroscopically confirmed multiple images corresponding to 10 background sources. A step forward was made with the HST/WFC3 infrared grism spectroscopy obtained with the Grism Lens-Amplified Survey from Space (GLASS, Schmidt et al. 2014; Treu et al. 2015), which led to the free-form lens model by Hoag et al. (2016), consisting of 30 spectroscopic multiple images from 15 background galaxies. Table 6.1 summarizes the main features of the multiple images catalogs used in several strong lensing models of M0416. An improvement was possible thanks to the advent of MUSE (see Sect. 2.6). The south-west region of the cluster was observed with MUSE as a part of the programme 094.A-0525 (PI: Bauer), which was given 11 hours of exposure time. The north-east region was instead targeted by the programs GTO 094.A-0115B (PI: Richard) and 0100.A-0764 (PI: Vanzella, Vanzella et al. 2021) for a total integration time of 17.1 hours, thus making M0416 the galaxy cluster with the deepest MUSE observations to date. Caminha et al. (2017) presented a lens model constrained by 102 spec-z multiple images corresponding to 37 sources. Their work was improved by including the hot X-ray emitting gas component (Bonamigo et al. 2017, 2018) and information on galaxy kinematics (Bergamini et al. 2019). The dataset of multiple images was further expanded by Bergamini et al. (2021), by taking advantage of the catalog by Vanzella et al. (2021). Richard et al. (2021) presented a catalog of 198 images from 71 galaxies. This number further increased to 237 images from 88 sources in Bergamini et al. (2023b). Another catalogue of 214 multiple images was compiled by Diego et al. (2024b) by re-analysing systems from existing literature, which led the non-parametric SL study of Diego et al. (2024a) based on JWST imaging, within the PEARLS collaboration (Sect. 2.5.2). Diego et al. (2024a) presents 343 multiple-image candidates, belonging to 119 systems. It is composed of all previously known systems with MUSE spectroscopic redshift as well as 41 additional candidates without spectroscopic confirmation.

Table 6.1: Number of multiple images $N_{\rm im}$ and corresponding number of systems $N_{\rm sys}$ with known spectroscopic redshift from several strong lensing studies of M0416.

Catalogue	$N_{\rm im}$	$N_{\rm sys}$	Spec. measurement
Zitrin et al. (2013)	34	1	CLASH
Grillo et al. (2015)	30	10	VLT/VIMOS
Hoag et al. (2016)	30	15	HST/GLASS
Caminha et al. (2017)	102	37	VLT/MUSE
Bergamini et al. (2021)	182	66	
Richard et al. (2021)	198	71	
Bergamini et al. (2023b)	237	88	
Diego et al. (2024a)	226	77	
Rihtaršič et al. (2025) - Gold	303	111	JWST/CANUCS
Rihtaršič et al. (2025) - Complete	349	124	
This Thesis - Gold	333	120	JWST/CANUCS + VLT/MUSE
This Thesis - Complete	437	162	

6.2 Data

6.2.1 Imaging and photometry

To study the galaxy cluster M0416, we employ the imaging dataset adopted by Rihtaršič et al. (2025), hereafter R25. It uses both JWST and archival HST imaging data. We use the CANUCS JWST/NIRCam observations in filters F090W, F115W, F150W, F200W, F277W, F356W, F410M, and F444W, which are characterized by a 6.4 ks exposure time per filter. We also rely on archival HST/ACS imaging data in F435W, F606W, and F814W filters, and HST/WFC3 data in F105W, F110W, F125W, F140W, F160W filters from the HFF and CLASH programs. The data were reduced and photometric catalogs were produced following the procedure outlined in Noirot et al. (2023) and Asada et al. (2024). The NIRCam and WFC3 images were first processed with the official JWST pipeline, drizzled on the same pixel scale, and aligned with respect to Gaia DR3 astrometry (Gaia Collaboration: Vallenari et al. 2023). We refer the reader to R25 and the references herein for a more detailed description of the pipeline. Figure 6.1 displays an RGB (red: F150W, green: F200W, blue: F090W) color-composite JWST image of the lensing galaxy cluster.

6.2.2 Spectroscopy

VLT/VIMOS and VLT/MUSE

We employed the same archival VLT/VIMOS and VLT/MUSE spectroscopy dataset used in Bergamini et al. (2021, 2023b) as a starting point to build our catalogue of multiple images. VLT/VIMOS observations provided redshift measurements over a $\sim 20'$ FoV (Balestra et al. 2016). VLT/MUSE observations were performed on the cluster core. In particular, one MUSE pointing (GTO 094.A0115B, P.I.: J. Richard) was centred on the north-east region of M0416 (2 hours of exposure time and $0.6''$ seeing). A second MUSE observation (094.A0525(A), P.I.: F. E. Bauer) was pointed to the south-west region of the cluster (11 hours of integration time and $1.0''$ seeing). As mentioned before, a deep MUSE observation on the north-east region of M0416 was performed through the observational program 0100.A0763(A) with P.I. E. Vanzella (Vanzella et al. 2021), which was

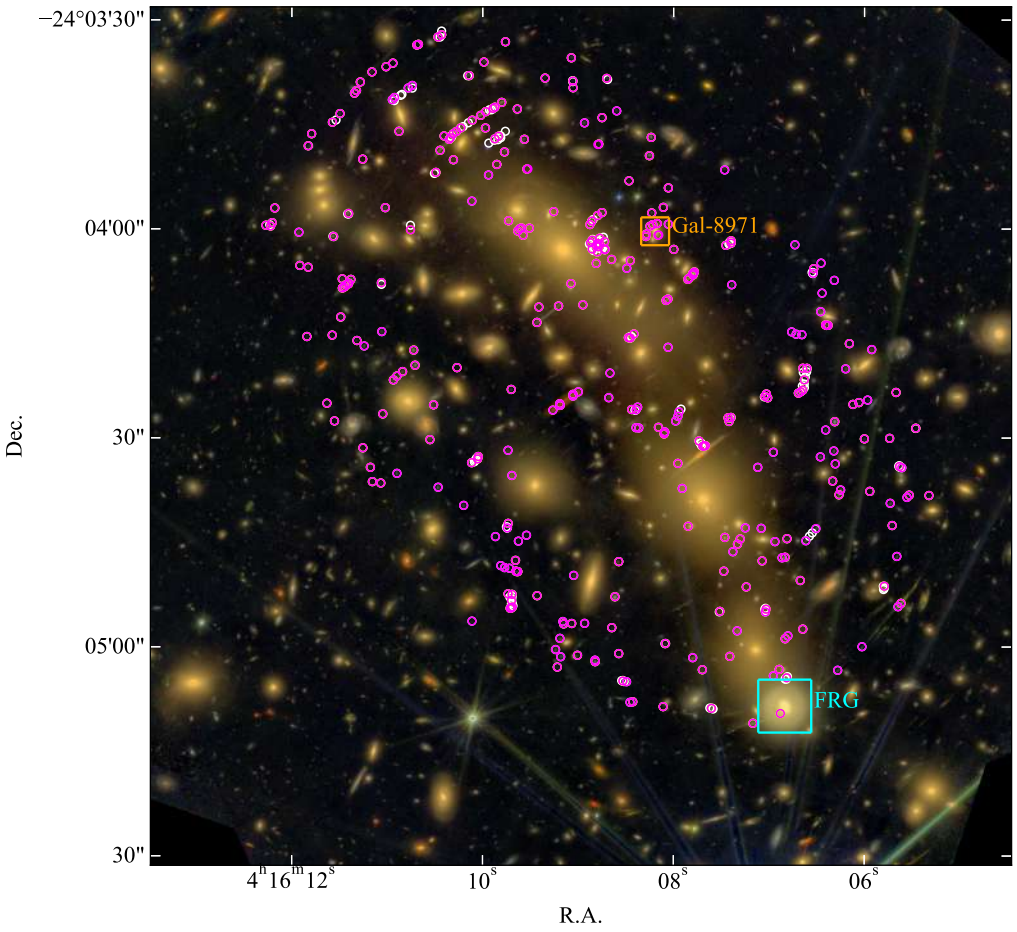

Figure 6.1: A RGB (red: F2000W, green: F150W, blue: F090W) color-composite JWST image of the lensing galaxy cluster MACS J0416.1−2403. The magneta circles represent the set of multiple images included in the gold model in this Thesis. The images added in the complete model are in white. The foreground spiral is indicated with a cyan box, galaxy 8971 with an orange one.

given 17.1 hours of integration time, with a seeing of $\sim 0.6''$.

JWST/NIRISS spectroscopy

Within the CANUCS survey, as described in R25, the galaxy cluster was targeted with NIRISS using the wide-field spectroscopy mode in F115W, F150W, and F200W filters and two orthogonal grisms (GR150C and GR150R, $R \sim 150$), with 9.7 ks exposure time per configuration. The data reduction process, the spectra extraction pipeline, and the redshift measurement procedure are presented in Noirot et al. (2023).

JWST/NIRSpec spectroscopy

M0416 was subsequently targeted with NIRSpec, with nominal resolving power $R \sim 100$ and the wavelength coverage range between 0.6μm and 5.3μm. The cluster was observed for a total integration time of 8.7 ks. Most images have a NIRSPec exposure of 3 ks, whereas for this cluster 3 configurations were taken.

6.3 Searching for new multiple images

In order to build a robust catalogue of multiple images, we started from the sample included in the lens model by Bergamini et al. (2023b), hereafter Bergamini+23, which consists of 237 spectroscopically-confirmed multiple images corresponding to 88 background sources, which in turn is based on the spectroscopic catalogues by Bergamini+23 and Richard et al. (2021). We then considered the catalogue compiled by R25, which adopted the one by Bergamini et al. (2023b) as starting point. They first analysed the new CANUCS NIRISS spectroscopy, which resulted in the identification of 11 new multiple images, relative to 4 background families. They then cross-matched the catalogue of Bergamini+23 with the one by Diego et al. (2024b) produced within the PEARLS survey (see Sect. 2.5.2). The complete catalogue of R25 consists of 415 multiple images candidates (corresponding to 150 families), which are classified into four quality categories: gold, bronze, sliver, and quartz. The gold class contains 303 images from 111 multiple-image systems, and is composed of all the galaxies having a reliable spectroscopic redshift as obtained with JWST/NIRISS or JWST/NIRSpec, or a previous MUSE measurement, and a clear JWST/NIRCam imaging counterpart. These are the images that were included in their lens model. The silver and bronze categories comprise 15 and 68, respectively, images characterized by an intermediate or low degree of confidence (R25). Finally, the quartz class is composed of 29 previously known multiple images with MUSE redshift measurements, but excluded from the lens model of R25, since they could not be clearly confirmed with NIRCam imaging. Out of the 303 gold multiple images of R25, 191 are in common with the catalogue of Bergamini+23. 8 out of the 112 new gold multiple images of R25 are part of the 11 above mentioned that were discovered using NIRSpec and NIRISS. The remaining 104 are from the catalogue by Diego et al. (2024b).

In this Thesis, we started from the catalogue of multiple images of Bergamini+23 and extended it by including the images labelled as gold by R25 that were not present in the model by Bergamini+23. We adopted the same nomenclature of R25 when labelling the multiple images. Namely, each clump is considered a separate system when reporting the total system count. The decimal digit represents the image ID, whereas the letter identifies the clump. The number following the dot denotes instead the image multiplicity. For instance, image K14b.3 is the third image of the second (b) clump of a galaxy

with ID 14. When adding the images of Bergamini+23 that were excluded in R25, we converted the nomenclature of Bergamini+23 into that of R25 to keep the consistency. When adding to the catalogue of B25 the extra golden images of R25, the initial sample consisted of 349 members, from which we excluded image K8a.3, since we could not securely associate it to the two other counter-images (K8a.2 and K8a.3), as well as other 15 images that we could not securely identify in the single-band and colour-composite images. This allowed us to produce a first catalogue consisting of 333 multiple images corresponding to 120 families.

We then visually examined these images looking for potential sub-knots within the multiply-lensed images, which was made possible thanks to the high-resolution in the near IR of the JWST imaging. To do so, we employed both single-band images (using the NIRCam filters F090W, F150W, and F200W) and a colour-composite RGB image (the same depicted in Figue 6.1). We considered as possible new knots only those satisfying the conditions on parity (see Chapter 1), and that could be detected in all the three bands cited. An example is given in Figs. 6.2, 6.3, and 6.4: the multiply-imaged knot K55b (images K55b.1, K55b.2, and K55b.3, identified with the gold circles) does clearly show four further luminosity peaks, encircled within black circles. We measured the position of these knots and added them into our catalogue. Another example is shown in Figs. 6.5, 6.6, and 6.7: the multiply-imaged K9 (images K9.1, K9.2, and K9.3, originally included in R25, identified with the gold circles), of which we managed to identify three additional knots (black circles): following the notation introduced above, we renamed images K9 as K9a, and labelled the other knots accordingly (K9b to K9d). This allowed us to obtain a catalogue of 437 multiple images, corresponding to 162 background sources. All of these are spectroscopically confirmed.

6.4 Lens modelling

We perform the SL analysis of the galaxy cluster M0416 using the software `Gravity.jl` (Lombardi 2024). We explored three lens models, characterized by the same total mass parametrization and set of cluster members, but a different sample of multiple images (see later). These models are labelled B23, Gold, and Complete, and a brief description of each of them is presented in Table 6.3. To sample the posterior distribution of the models explored in this Thesis, we employed the NRPT algorithm implementation in the software. All the optimizations of the lens models were carried out in the simplified image-plane configuration.

6.4.1 Total mass parametrization

To describe the total mass distribution of M0416, we adopt the same parametrization adopted in B23. Following Eq. (3.43), we describe the total gravitational potential $\phi^{\rm tot}$ of the galaxy cluster as the sum of the following terms,

$$\phi^{\rm tot} = \sum_{i=1}^{N_{\rm h}} \phi_i^{\rm halo} + \sum_{j=1}^{N_{\rm gas}} \phi_j^{\rm gas} + \sum_{j=1}^{N_{\rm g}} \phi_j^{\rm gal} + \phi^{\rm frg} + \phi^{\rm g8971}\,, \tag{6.1}$$

where, as usual, the first sum runs over the $N_{\rm h}$ extended dark matter haloes, whereas the second one over the $N_{\rm gas}$ extended hot gas haloes contributing to the total mass budget of the cluster. The third sum runs instead over the $N_{\rm g}$ cluster members following the scaling relations in Eq. (3.44) and Eq. (3.45). $\phi^{\rm frg}$ is the gravitational potential due to

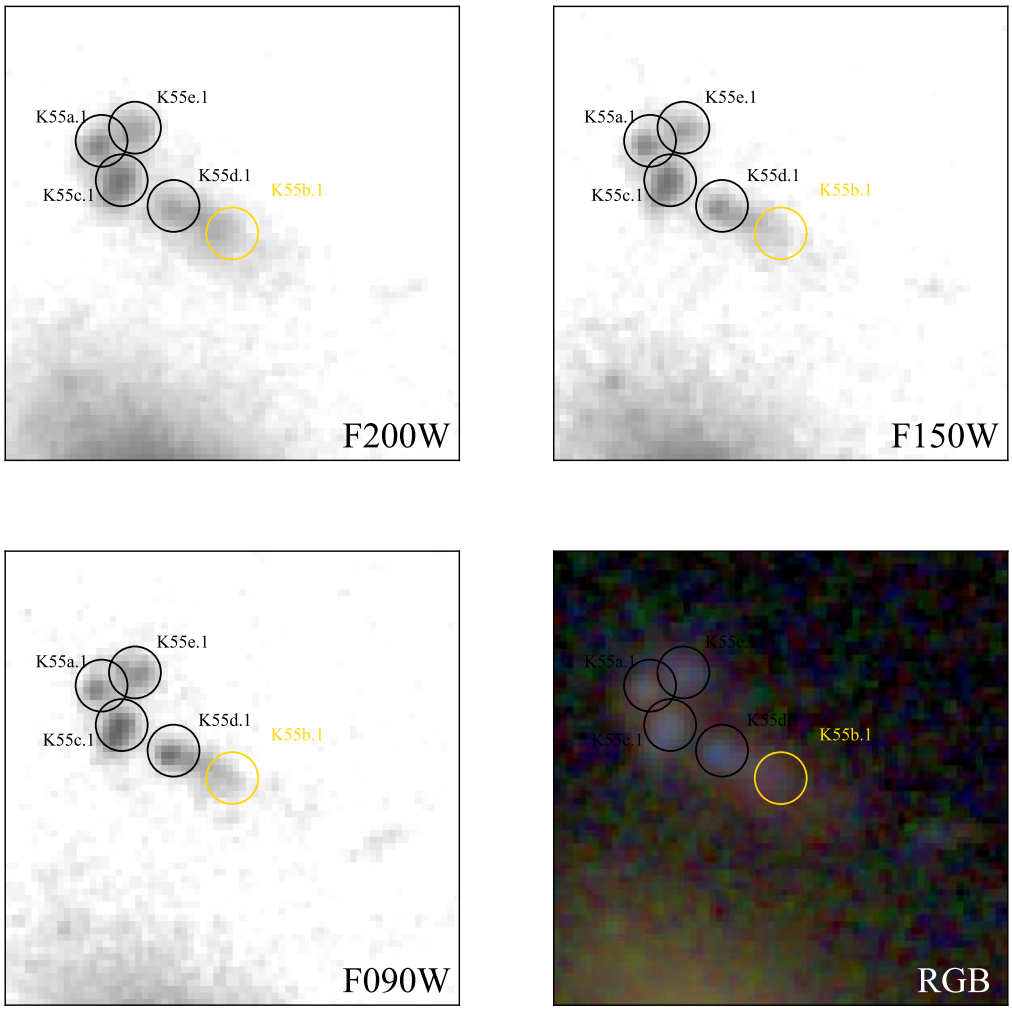

Figure 6.2: Cutouts of image K55b.1 (identified with the golden circle), as included in the lens model by R25, and the sub-knots identified while examining the multiple images (black circles). The cutouts are taken in the single bands F009W, F150W, and F200W, and in a colour-composite RGB image of the lens cluster.

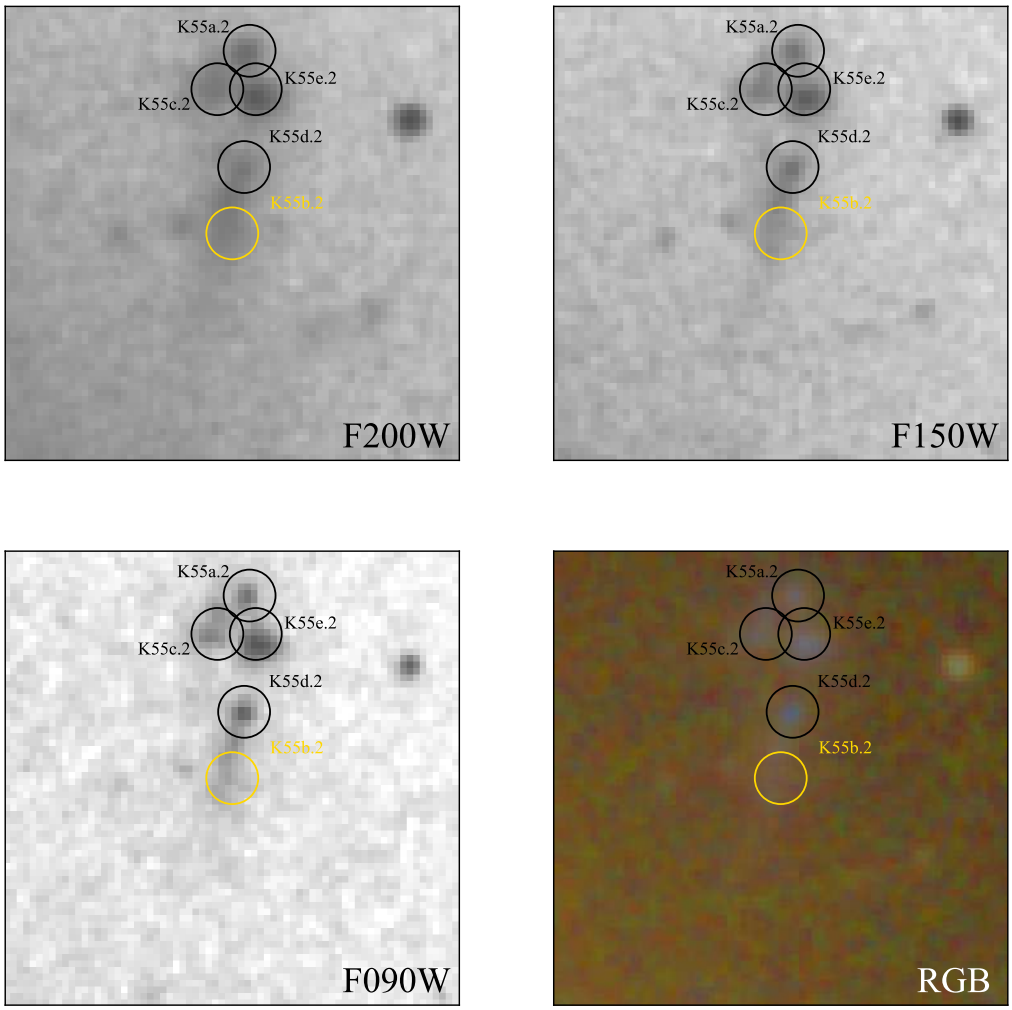

Figure 6.3: Cutouts of image K55b.2 (identified with the golden circle), as included in the lens model by R25, and the sub-knots identified while examining the multiple images (black circles). The cutouts are taken in the single bands F090W, F150W, and F200W, and in a colour-composite RGB image of the lens cluster.

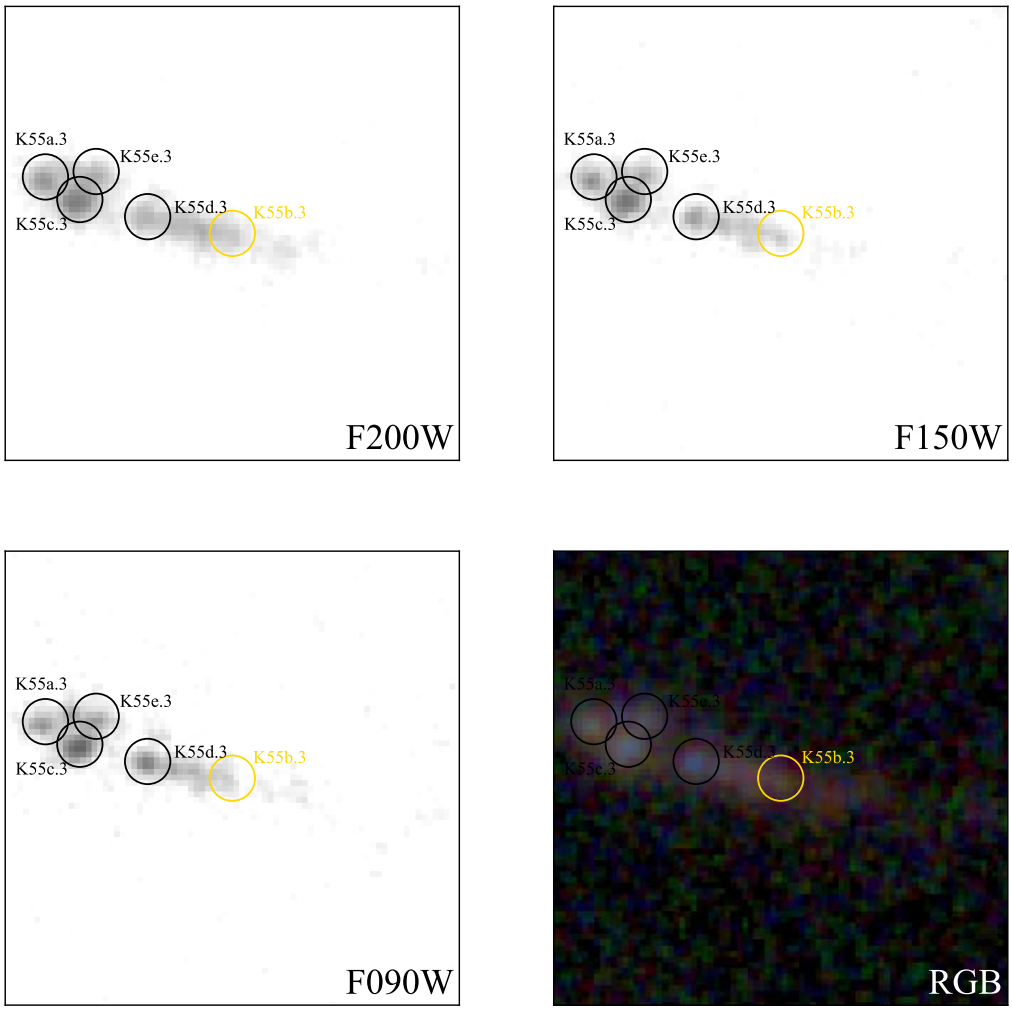

Figure 6.4: Cutouts of image K55b.3 (identified with the golden circle), as included in the lens model by R25, and the sub-knots identified while examining the multiple images (black circles). The cutouts are taken in the single bands F090W, F150W, and F200W, and in a colour-composite RGB image of the lens cluster.

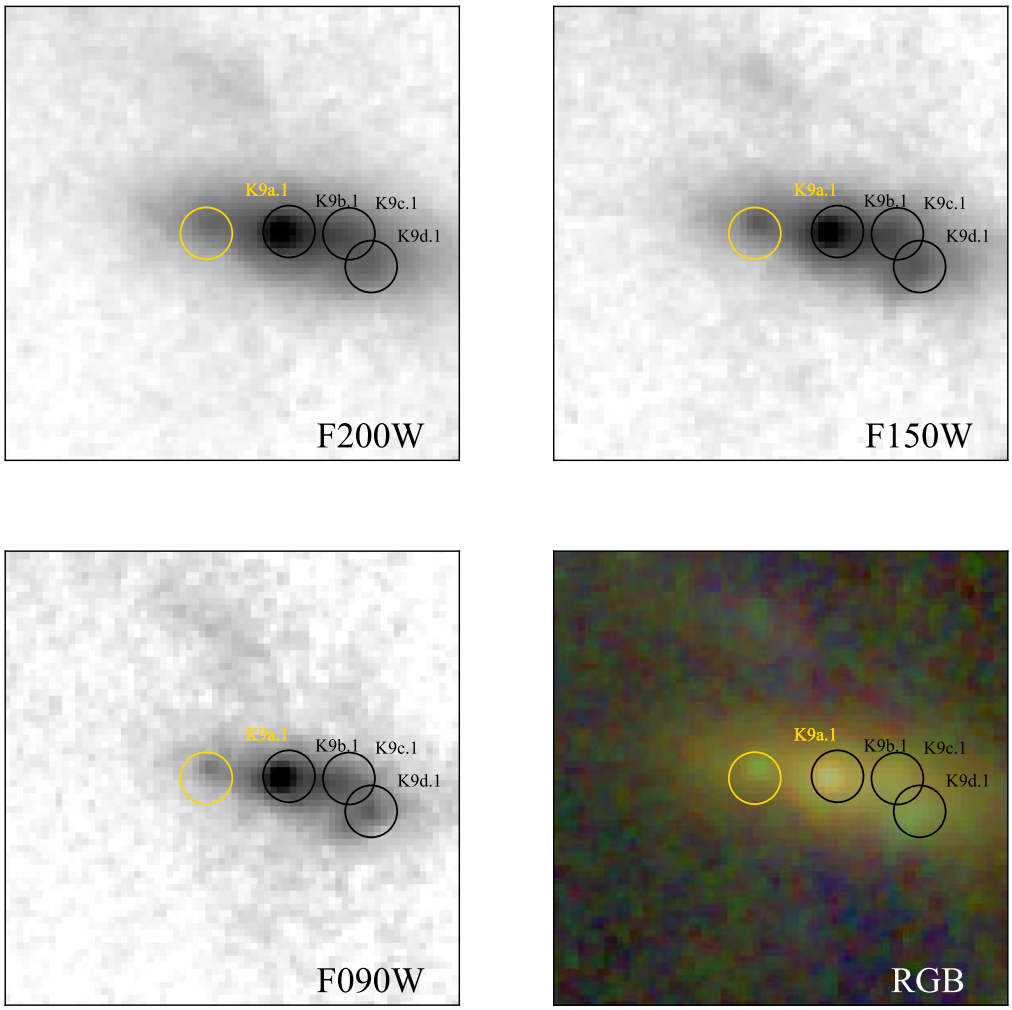

Figure 6.5: Cutouts of image K9a.1 (identified with the golden circle), included in the lens model by R25 as K9.1, and the sub-knots identified while examining the multiple images (K9b.1 to K9d.1, black circles). The cutouts are taken in the single bands F090W, F150W, and F200W, and in a colour-composite RGB image of the lens cluster.

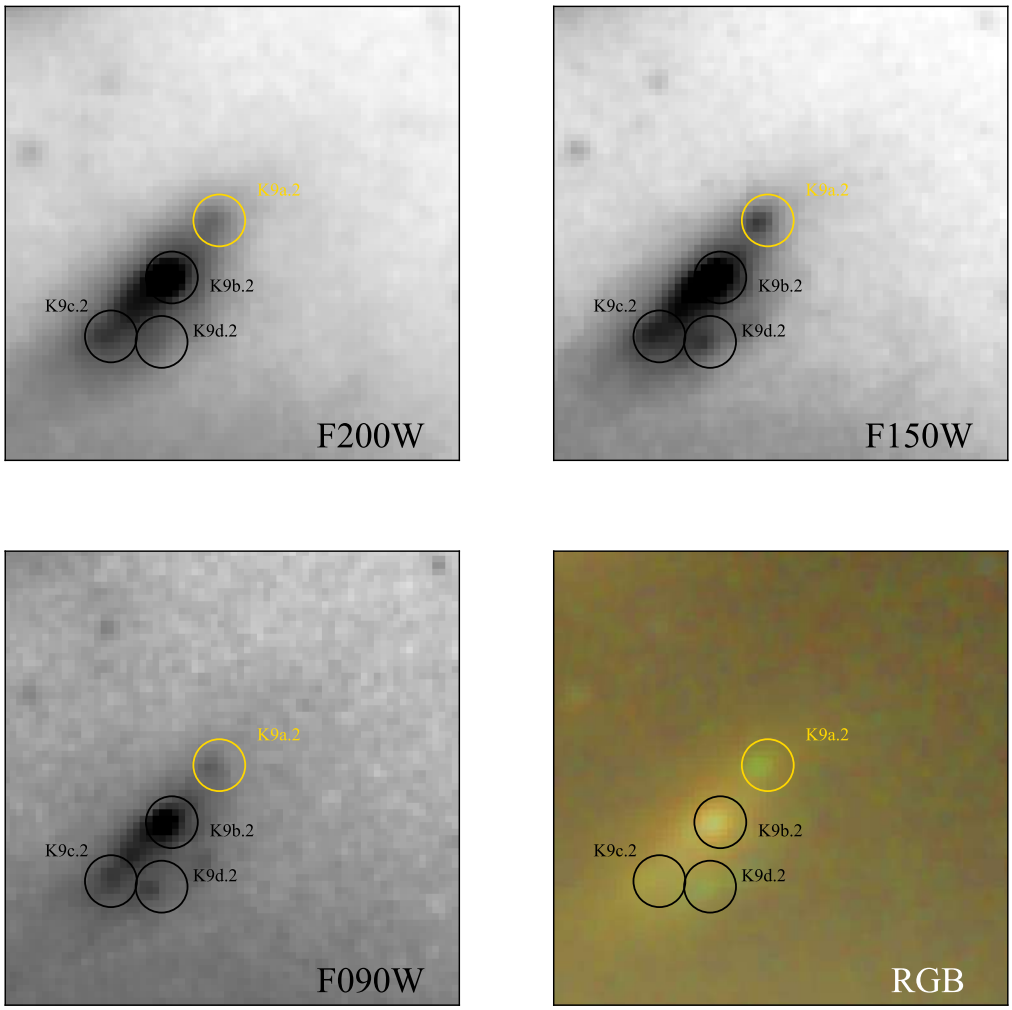

Figure 6.6: Cutouts of image K9a.2 (identified with the golden circle), included in the lens model by R25 as K9.2, and the sub-knots identified while examining the multiple images (K9b.2 to K9d.2, black circles). The cutouts are taken in the single bands F090W, F150W, and F200W, and in a colour-composite RGB image of the lens cluster.

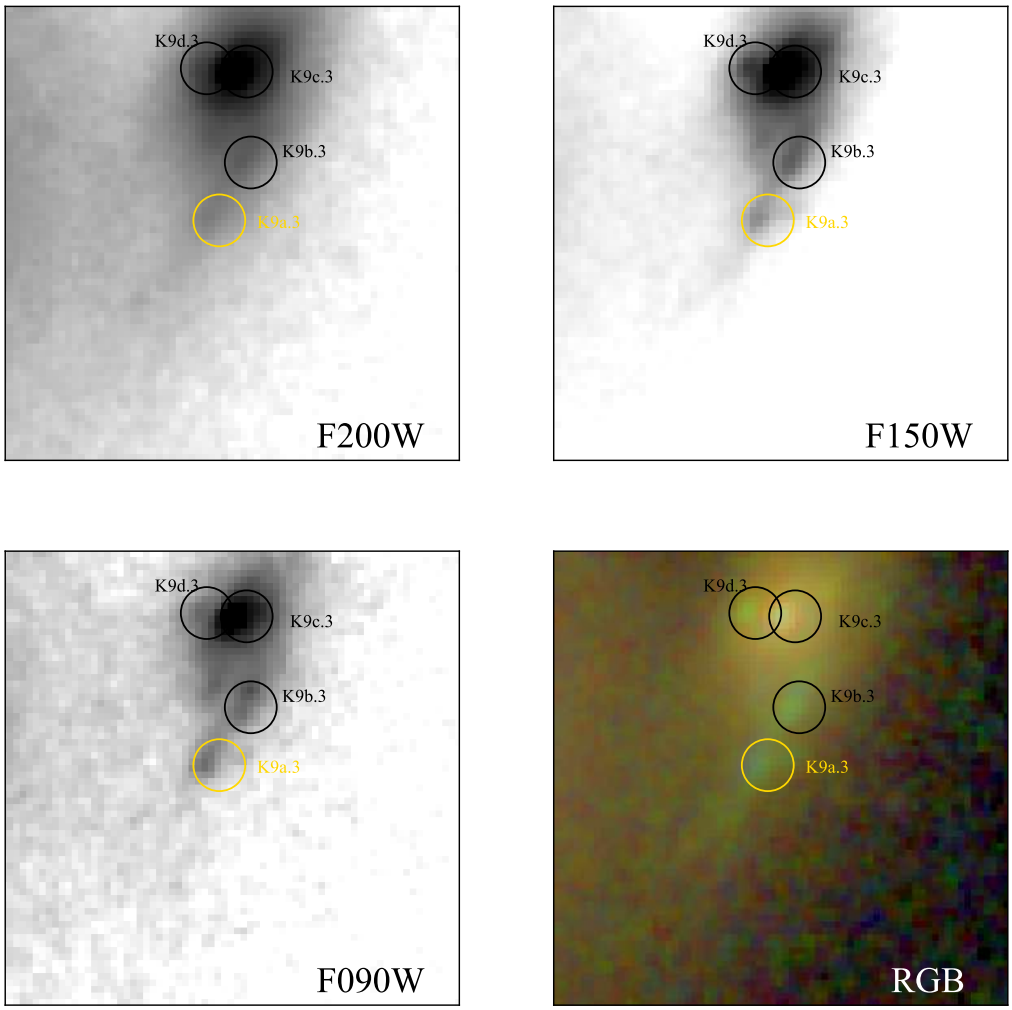

Figure 6.7: Cutouts of image K9a.3 (identified with the golden circle), included in the lens model by R25 as K9.3, and the sub-knots identified while examining the multiple images (K9b.3 to K9d.3, black circles). The cutouts are taken in the single bands F090W, F150W, and F200W, and in a colour-composite RGB image of the lens cluster.

a foreground spiral galaxy, identified with the cyan box in Figure 6.1, whereas $\phi^{\rm g8971}$ corresponds to the contribution of the cluster member 8971 (the number refers to the identification number of the spectroscopic catalogue of Bergamini+23, orange box in Figure 6.1), which is treated separately.

Extended dark matter halos

Following Bergamini+23, we include four extended dark matter haloes, described in terms of dPIE density profiles (see Sect. 3.3.2), labelled DM1 to DM4. Haloes DM1, DM2, and DM4 are represented with elliptical dPIE profiles. Differently from the previous Chapters, to model the galaxy cluster M0416 we did not use the parametrization of the dPIE density profiles of `Gravity.jl`, rather we adopted that of `LensTool` (Kneib et al. 1996; Jullo et al. 2007), which is also implemented in `Gravity.jl`. This choice was motivated as to make a direct comparison between the lens models of this Thesis and that of Bergamini+23, who performed their analysis using `LensTool`. The `LensTool`-based dPIE density profiles are characterized by six free parameters as well: the position on the sky (x, y), the ellipticity ε, the position angle θ (computed clockwise from the East axis in `LensTool`), the central velocity dispersion $\sigma_{\rm v}$ and the core radius $r_{\rm c}$. The relationship between the `LensTool` and `Gravity.jl` definitions of the parameters of the dPIE profile is given in Sect. 3.3.2. DM3 is instead described with a spherical `LensTool`-based dPIE profile, hence with four free parameters: the position in the sky, the velocity dispersion, and the core radius. For all four haloes, the truncation radius is set equal to 2×10^3 arcsec as to mimic an isothermal behaviour at large radii.

Cluster members

We use the same catalogue of cluster members in Bergamini+23, consisting of 213 galaxies. We exclude from this set galaxy Gal-8971 (orange box in Figure 6.1), which is treated separately (see later). The remaining 212 cluster member galaxies (the sub-halo component of the galaxy cluster) are modelled in terms of spherical `LensTool`-derived dPIE profiles. Since their position is fixed, each sub-halo is described by only three parameters: the central velocity dispersion σ_v, and the core and truncation radii, $r_{\rm c}$ and $r_{\rm t}$, respectively. We further reduced the number of free parameters by taking advantage of the scaling relations given by Eq. (3.44) and Eq. (3.45). Following Bergamini+23, we adopt HST/F160W photometry for their calibration. As reference luminosity, we use that of the BCG-North, whose total F160W magnitude is $m^{\rm BCG}_{\rm F160W} = 16.02$. We benefit from the measurements of the stellar velocity dispersion for 64 cluster members presented in Bergamini et al. (2019, 2021), and fix the coefficient of Eq. (3.44) $\alpha = 0.3$. This implies, in order to be consistent with the observed Fundamental Plane, $\beta = 0.6$. We impose a Gaussian prior on the reference velocity dispersion $\sigma_{\rm ref} = 248 \pm 28$ km s^{-1}. For the reference truncation radius, we adopt an uninformative uniform prior between 1 and 50 arcsec. For each cluster member, the core radius is kept equal to 0.005 arcsec.

Hot gas distribution

All the lens models presented in this Thesis contain four additional cluster-scale dPIEs, that are used to parametrize the hot gas mass distribution, obtained by fitting the *Chandra* deep X-ray surface brightness distribution, as done by Bonamigo et al. (2017, 2018). Each gas halo is described in terms of elliptical `LensTool`-derived dPIE profiles, with all the parameters kept fixed. The values of the parameters of the density profiles used to represent the hot gas haloes are quoted in Table 6.2.

Table 6.2: Parameter values of the four gas haloes introduced in the total mass parametrization of the galaxy cluster M0416, used in all the lens models explored in this Thesis. The first column reports the mass component. The second column contains the parameters of the density profile used to describe the corresponding mass component. Their values quoted in the last column. The x and y coordinates are measured with respect to the position of the BCG-N (RA $= 64.0382044°$, Dec $= -24.0674917°$, J2000.0).

Mass component	Parameter	Value
1st gas halo	x [″]	-18.1
	y [″]	-12.1
	$\sigma_{\rm v}$ [km s^{-1}]	433
	ε	0.12
	θ [deg]	-156.8
	$r_{\rm core}$ [″]	149.2
	$r_{\rm cut}$ [″]	149.8
2nd gas halo	x [″]	30.8
	y [″]	-48.7
	$\sigma_{\rm v}$ [km s^{-1}]	249
	ε	0.42
	θ [deg]	-71.5
	$r_{\rm core}$ [″]	34.8
	$r_{\rm cut}$ [″]	165.8
3rd gas halo	x [″]	-2.4
	y [″]	-1.3
	$\sigma_{\rm v}$ [km s^{-1}]	102
	ε	0.42
	θ [deg]	-54.7
	$r_{\rm core}$ [″]	8.3
	$r_{\rm cut}$ [″]	37.6
4th gas halo	x [″]	-20.1
	y [″]	14.7
	$\sigma_{\rm v}$ [km s^{-1}]	282
	ε	0.40
	θ [deg]	-49.3
	$r_{\rm core}$ [″]	51.7
	$r_{\rm cut}$ [″]	52.35

Foreground spiral

The foreground spiral ($z = 0.112$, cyan box in Figure 6.1), being an external perturber affecting the total gravitational potential of the cluster, is added as an additional contribute to the total mass budget of the lens. It is modelled in terms of a spherical `LensTool`-based dPIE density profile characterised by two free parameters: the velocity dispersion and the core radius. Its core radius is fixed to to 1×10^{-3} arcsec as to simulate an isothermal behaviour at small radii. Differently from Bergamini+23 and R25, we keep the spiral galaxy at its redshift, instead of fixing it at the redshift of the cluster, and thus perform a full multi-plane lensing analysis.

Galaxy Gal-8971

Galaxy Gal−8971 (R.A. = 4:16:08.18, Dec. = −24:04:00.28) is modelled separately from the other cluster members and excluded from the scaling relations. This choice is motivated by the fact that this elliptical galaxy produces a galaxy-galaxy strong lensing event consisting of seven multiple images. It is described in terms of an elliptical `LensTool`-derived dPIE profile with negligible core radius (the same as the foreground spiral), thus with four free parameters: the velocity dispersion, the ellipticity, the position angle, and the truncation radius.
Tables 6.4 and 6.5 contain the priors we adopted for the 30 free parameters of the lens models we explored in this Thesis.

6.4.2 Catalogue of multiple images

A anticipated, in this Thesis, we explore three lens models characterised by the same total mass parametrisation, but different sets of multiple images:

Model B23. We build a lens model having the same set of multiple images as in Bergamini+23, namely 237 spectroscopically-confirmed multiple images corresponding to 88 background sources. Differently from Bergamini+23, whose astrometry was anchored to HST/F814W imaging, we had to first correct the coordinates as to match them with JWST NIRCam/F150W imaging. To do so, we relied on the work by R25, who modified the positions of the multiple images of Bergamini+23 included in their gold model. We quantified the shift they measured and applied it to correct the remaining coordinates of Bergamini+23.

Model Gold. Starting from the set of multiple images included in model B23, we built another lens model by extending our initial sample to take into account the new gold images included in R25. This model is characterised by 333 multiple images corresponding to 120 sources.

Model Complete. We took advantage of the quality of the new JWST multi-band observations of the galaxy cluster to look for potential sub-knots within the different multiple images. This allowed us to identify several new knots in some of the multiply-lensed sources, allowing us to build a final lens model consisting of 437 point-like multiple images (162 background sources).

All the multiple images and knots which could be clearly detected within the NIRCam imaging were assigned a position uncertainty of $0.1''$. Complementarily, images which could not be clearly detected were given a measurement uncertainty of $0.4''$, consistent with the typical spatial resolution of the WFM of MUSE (see Sect. 2.6). A brief summary of the specifics of each lens model explored in this work is given in Table 6.3. The distribution in redshift of the multiple images included in the lens models we explored in this Thesis is given in Figure 6.8. The multiple images of model B23 are in black, whereas the new ones added are in blue (model Gold) and light blue (model Complete).

6.5 Results

The analysis of the galaxy cluster M0416 is still in progress, so in the following we are presenting the results obtained up to date. Tables 6.7 and 6.8 contain, for each of the three lens models explored, the best-fit values of all the 30 free parameters used to parametrize the total mass distribution of M0416. For each of them, we quote the median value, whereas the lower and upper values denote the interval of the 16th and 84th percentiles,

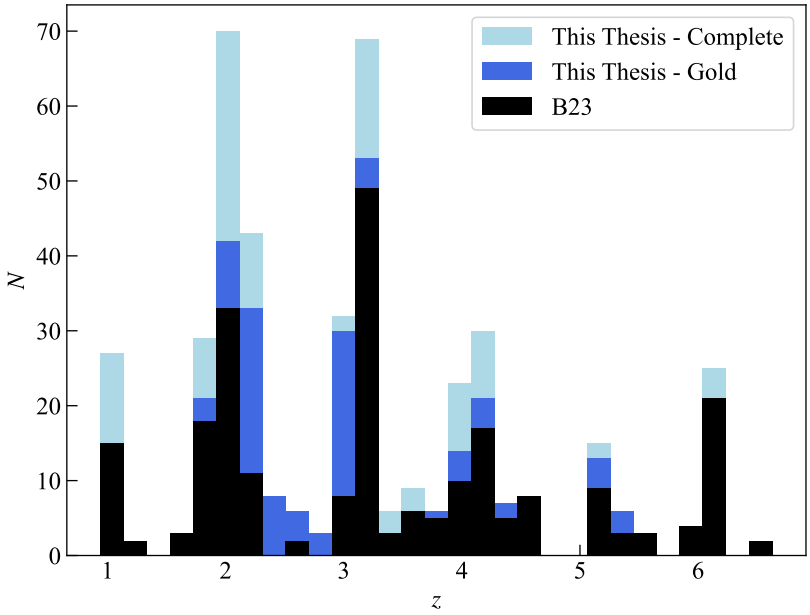

Figure 6.8: Redshift distribution of the multiple images included in the lens models explored in this Thesis: model B23 (black), model Gold (blue), and model Complete (light blue).

Table 6.3: Main specifics of the lens models explored. For each column, we report the number of multiple images included $N_{\rm imgs}$, the number of the corresponding background sources $N_{\rm src}$, the number of free parameters $N_{\rm par}$, and the number of degrees of freedom d.o.f.

Model	$N_{\rm imgs}$	$N_{\rm src}$	$N_{\rm par}$	d.o.f
B23	237	88	30	268
Gold	333	120	30	396
Complete	437	162	30	520

respectively. If we first compare models B23 and Gold, we observe an overall agreement, except for few parameters. As far as the scaling relations for the cluster members are concerned, model Gold predicts (as median value) a velocity dispersion $\sim 9\%$ lower than that predicted by model B23. Correspondingly, the value of the truncation radius in model Gold is $\sim 35\%$ higher than in model B23. As far as the foreground spiral is concerned, model Gold predicts a higher value of the velocity dispersion, and a lower value (approximately one fourth) for the truncation radius. When considering model Complete, the recovered values of the parameters are in general accordance with model Gold, except for the truncation radius of galaxy Gal-8971, whose value is approximately ten times larger than that of model B23, despite the remaining parameters describing the galaxy are in excellent agreement between each other. It is worth noticing how, in model Complete, the uncertainties on the velocity dispersion are way larger than in the other two lens models explored, especially for DM2 and DM4. We can explain this be-

Table 6.4: Input parameter values of all the lens models explored for the galaxy cluster M0416. The first column reports the mass component. The second column contains the parameters of the density profile used to describe the corresponding mass component. The third column shows the prior distributions adopted. When a flat prior on a free parameter value is considered, the boundaries of the prior separated by the ÷ symbol are reported. In case of a Gaussian prior, the notation $a \pm b$ is adopted, with a the mean and b the standard deviation of the distribution, respectively. The x and y coordinates are measured with respect to the position of the BCG-N (RA $= 64.0382044°$, Dec $= -24.0674917°$, J2000.0). In case the value of a parameter is kept fixed, its value is quoted in the last column.

Mass component	Parameter	Prior	Fixed
DM1	x [″]	$-15 \div 15$	–
	y [″]	$-15 \div 15$	–
	$\sigma_{\rm v}$ [km s^{-1}]	$350 \div 1000$	–
	ε	$0.2 \div 0.9$	–
	θ [deg]	$100 \div 180$	–
	$r_{\rm core}$ [″]	$0 \div 20$	–
	$r_{\rm cut}$ [″]	–	2000
DM2	x [″]	$-15 \div 30$	–
	y [″]	$-45 \div 30$	–
	$\sigma_{\rm v}$ [km s^{-1}]	$350 \div 1200$	–
	ε	$0.2 \div 0.9$	–
	θ [deg]	$90 \div 170$	–
	$r_{\rm core}$ [″]	$0 \div 25$	–
	$r_{\rm cut}$ [″]	–	2000
DM3	x [″]	$-55 \div -25$	–
	y [″]	$0 \div 30$	–
	$\sigma_{\rm v}$ [km s^{-1}]	$50 \div 750$	–
	ε	–	0.0
	θ [deg]	–	0.0
	$r_{\rm core}$ [″]	$0 \div 35$	–
	$r_{\rm cut}$ [″]	–	2000
DM4	x [″]	$-10 \div 50$	–
	y [″]	$-75 \div -15$	–
	$\sigma_{\rm v}$ [km s^{-1}]	$100 \div 1000$	–
	ε	$0.2 \div 0.9$	–
	θ [deg]	$0 \div 180$	–
	$r_{\rm core}$ [″]	$0 \div 20$	–
	$r_{\rm cut}$ [″]	–	2000
Scaling relations	$\sigma_{\rm ref}$ [km s^{-1}]	248 ± 28	–
	$r_{\rm cut,ref}$ [″]	$1 \div 50$	–

haviour by observing how these two dark matter haloes are close to each other ($\sim 10''$), with overlapping priors on their positions. If we compare our results with those obtained by Bergamini et al. (2023b), whose lens model is based on HST imaging, we find an overall agreement. Interestingly, they find, for Gal-8971, a value of the truncation

Table 6.5: Continued.

Mass component	Parameter	Prior	Fixed
Galaxy Gal-8971	x [″]	–	13.3
	y [″]	–	2.6
	$\sigma_{\rm v}$ [km s^{-1}]	$60 \div 200$	–
	ε	$0.0 \div 0.6$	–
	θ [deg]	$-90.0 \div 90.0$	–
	$r_{\rm core}$ [″]	–	0.001
	$r_{\rm cut}$ [″]	$0.0002 \div 50.0$	–
Foreground spiral ($z = 0.112$)	x [″]	–	32.0
	y [″]	–	-65.6
	$\sigma_{\rm v}$ [km s^{-1}]	$50 \div 350$	–
	ε	–	0.0
	θ [deg]	–	0.0
	$r_{\rm core}$ [″]	–	0.0
	$r_{\rm cut}$ [″]	$5.0 \div 100.0$	–

radius consistent with the value of model Complete, rather than the other two models, more specifically with our model B23, which has the same constraints. As far as the foreground spiral is concerned, the results of our model B23 are consistent with Bergamini et al. (2023b). The discrepancy with the other two models can be attributed to our multi-plane analysis. We still find a nice agreement when comparing our results with those by R25. Interestingly, we find for the fourth cluster-scale DM halo, a value for the velocity dispersion which is ~ 100 km s^{-1} higher than the values we recovered. Nevertheless, the values of model Complete and R25 are consistent within one standard deviation. Similarly, as far as the scaling relations for the cluster members are concerned, the value of the reference velocity dispersion of R25 is ~ 100 km s^{-1} higher than what we obtained with our three models. The findings for the truncation radius of the foreground spiral in models Gold and Complete are in disagreement with R25, which, in turn, is consistent with our model B23. Finally, the recovered value of the truncation radius of Gal-8971 by R25 agrees with model Complete, but disagrees by $\sim 10''$ with our other two lens models.

In Fig. 6.9 we show the displacements $\boldsymbol{\Delta}_i$ along the x and y directions between the observed and model-predicted multiple images included in models B23 (blue), Gold (red), and Complete (green). Out of the 237 multiple images included in model B23, 3 of them show a $|\boldsymbol{\Delta}_i| > 1''$. Similarly, 3 out of the 333 images used to constrain the Gold model have a $|\boldsymbol{\Delta}_i| > 1''$, whereas 11 multiple images (out of 437, $\sim 2.5\%$) of model Complete have a $|\boldsymbol{\Delta}_i| > 1''$. In Table 6.6 we quote the rms $\boldsymbol{\Delta}_{\rm rms}$ for all the three lens models. Model B23 is characterized by a $\boldsymbol{\Delta}_{\rm rms} = 0.36''$, slightly smaller than the value recovered by Bergamini et al. (2023b) of $\boldsymbol{\Delta}_{\rm rms} = 0.43''$ using HST data. Model Gold shows a $\boldsymbol{\Delta}_{\rm rms} = 0.41''$, whereas the Complete model has a $\boldsymbol{\Delta}_{\rm rms} = 0.47''$. For comparison, the lens model in R25, based on the same imaging but different constraints, has a $\boldsymbol{\Delta}_{\rm rms} = 0.52''$. Models Gold and Complete are characterized by an increase of $\sim 140\%$ and $\sim 185\%$, respectively, in the number of multiple images, with respect to model B23, hence resulting in an increased complexity of the system. These additional multiple images allow us to better constrain the fine details of the M0416 total mass distribution.

We then recovered the cumulative total mass distribution of the galaxy cluster for

Table 6.6: The root mean square error $\mathbf{\Delta}_{\rm rms}$ for the lens models explored in this Thesis for the lensing galaxy cluster M0416.

Model	$\mathbf{\Delta}_{\rm rms}$ [″]
B23	0.36
Gold	0.41
Complete	0.47

Table 6.7: Optimized parameter values of all the lens models explored for the galaxy cluster M0416. The first column reports the mass component, whereas the second contains the parameters of each constituent. In the last columns, we quote the median value, the 16th, and 84th percentiles of the marginalized posterior distribution, for each lens model. The x and y coordinates are measured with respect to the position of the BCG-N (RA $= 64.0382044°$, Dec $= -24.0674917°$, J2000.0).

Mass component	**Parameter**	**Model B23**	**Model Gold**	**Model Complete**
DM1	x [″]	$0.11^{+0.06}_{-0.06}$	$0.01^{+0.07}_{-0.06}$	$-0.05^{+0.30}_{-0.20}$
	y [″]	$0.05^{+0.05}_{-0.08}$	$-0.17^{+0.04}_{-0.08}$	$-0.46^{+0.13}_{-0.07}$
	$\sigma_{\rm v}$ [km s^{-1}]	615^{+3}_{-2}	602^{+1}_{-3}	604^{+16}_{-21}
	ε	$0.761^{+0.002}_{-0.004}$	$0.744^{+0.003}_{-0.003}$	$0.763^{+0.008}_{-0.008}$
	θ [deg]	$144.3^{+0.1}_{-0.2}$	$141.8^{+0.1}_{-0.2}$	$142.1^{+0.4}_{-0.6}$
	$r_{\rm core}$ [″]	$9.0^{+0.1}_{-0.1}$	$8.4^{+0.1}_{-0.1}$	$8.4^{+0.3}_{-0.6}$
DM2	x [″]	$20.82^{+0.10}_{-0.10}$	$22.94^{+0.12}_{-0.14}$	$23.06^{+0.26}_{-0.25}$
	y [″]	$-44.96^{+0.07}_{-0.03}$	$-48.28^{+0.21}_{-0.20}$	$-47.37^{+1.07}_{-1.53}$
	$\sigma_{\rm v}$ [km s^{-1}]	673^{+2}_{-1}	623^{+2}_{-5}	674^{+35}_{-59}
	ε	$0.763^{+0.003}_{-0.006}$	$0.705^{+0.005}_{-0.006}$	$0.721^{+0.010}_{-0.007}$
	θ [deg]	$123.9^{+0.1}_{-0.2}$	$125.8^{+0.2}_{-0.2}$	$125.9^{+0.7}_{-0.5}$
	$r_{\rm core}$ [″]	$12.1^{+0.1}_{-0.1}$	$10.4^{+0.1}_{-0.2}$	$11.3^{+0.4}_{-1.0}$
DM3	x [″]	$-31.25^{+0.13}_{-0.17}$	$-30.14^{+0.15}_{-0.15}$	$-30.87^{+0.64}_{-0.22}$
	y [″]	$9.35^{+0.10}_{-0.09}$	$10.16^{+0.15}_{-0.09}$	$10.30^{+0.18}_{-0.14}$
	$\sigma_{\rm v}$ [km s^{-1}]	323^{+2}_{-13}	346^{+2}_{-2}	347^{+9}_{-29}
	$r_{\rm core}$ [″]	$6.6^{+0.2}_{-0.6}$	$6.9^{+0.1}_{-0.1}$	$7.4^{+0.2}_{-1.1}$
DM4	x [″]	$24.96^{+0.18}_{-0.22}$	$22.32^{+0.10}_{-0.11}$	$22.64^{+0.18}_{-0.21}$
	y [″]	$-35.56^{+0.28}_{-0.19}$	$-32.79^{+0.17}_{-0.09}$	$-32.05^{+0.42}_{-1.33}$
	$\sigma_{\rm v}$ [km s^{-1}]	483^{+2}_{-1}	502^{+3}_{-5}	440^{+46}_{-58}
	ε	$0.865^{+0.005}_{-0.004}$	$0.821^{+0.005}_{-0.004}$	$0.831^{+0.029}_{-0.018}$
	θ [deg]	$132.3^{+0.3}_{-0.2}$	$132.0^{+0.5}_{-0.2}$	$132.9^{+1.4}_{-1.7}$
	$r_{\rm core}$ [″]	$7.3^{+0.1}_{-0.1}$	$7.2^{+0.2}_{-0.1}$	$5.8^{+0.9}_{-1.3}$
Scaling relations	$\sigma_{\rm ref}$ [km s^{-1}]	291^{+1}_{-1}	268^{+1}_{-1}	274^{+2}_{-12}
	$r_{\rm cut,ref}$ [″]	$9.9^{+0.1}_{-0.4}$	$13.4^{+0.3}_{-0.2}$	$13.3^{+3.6}_{-1.3}$

Table 6.8: Continued.

Mass component	Parameter	Model B23	Model Gold	Model Complete
Galaxy Gal-8971	$\sigma_{\rm v}$ [km s^{-1}]	120^{+10}_{-11}	110^{+10}_{-11}	101^{+5}_{-3}
	ε	$0.53^{+0.05}_{-0.14}$	$0.53^{+0.06}_{-0.24}$	$0.56^{+0.02}_{-0.25}$
	θ [deg]	$-55.8^{+5.5}_{-5.9}$	$-48.0^{+13.5}_{-6.6}$	$-48.5^{+13.3}_{-4.6}$
	$r_{\rm cut}$ [″]	$1.7^{+1.0}_{-0.5}$	$2.8^{+5.1}_{-2.0}$	$17.4^{+4.6}_{-6.5}$
Foreground spiral	$\sigma_{\rm v}$ [km s^{-1}]	132^{+5}_{-5}	186^{+4}_{-5}	173^{+11}_{-12}
	$r_{\rm cut}$ [″]	$60.0^{+15.1}_{-10.7}$	$15.2^{+1.6}_{-2.0}$	$18.7^{+1.8}_{-2.4}$

the three models explored. For each of them, we randomly extracted 300 points from the Markov Chain, and for each point estimated the corresponding total mass distribution, hence 300 total mass profiles per model. We estimated the uncertainty from the 16th and 84th quantiles of these profiles. We find an overall agreement between the three profiles, as can be seen in the top panel of Figure 6.10, which displays the cumulative total mass profiles as a function of the distance from the BCG-N. To better visualize the differences in the profiles, the bottom panel of the Figure shows the ratio of the three curves with respect to model B23. The cumulative total mass profiles of models Gold (red) and Complete (green) deviate from that of model B23 (blue) by less than $\sim 5\%$. We quote in Table 6.9 the values of the total mass of the cluster enclosed within a circle whose radius is the median distance of the multiple images included in model Gold from the BCG-N. The uncertainty corresponds to the interval between the 16th and the 84th quantiles.

Table 6.9: Total mass of M0416 estimated for all the lens models explored in this Thesis. Each value corresponds to the total mass enclosed within a circle whose radius is the median distance of the multiple images included in the Gold model. The uncertainty was estimated, for each model, by evaluating 300 total mass profiles obtained by randomly extracting 300 points from the Markov Chain, and then quantifying the 16th and 84th quantiles.

Model	Mass $[10^{14}\,M_{\odot}]$
B23	1.424 ± 0.003
Gold	1.434 ± 0.003
Complete	1.428 ± 0.009

Finally, we obtained the critical curves and the magnification maps for the three lens models explored. We estimated both at redshift $z = 3.067$, which is the median of the redshift distribution of the multiple images in model Gold. The critical curves estimated at this redshift are shown in Figure 6.11 for models B23 (cyan), Gold (magenta), and Complete (white). We find an overall agreement, except for a slight discrepancy in the north-east corner of the Figure, with respect to the BCG-N between the Gold model with respect to the other two. Similarly, models Gold and Complete slightly disagree with B23 in the neighborhood of the foreground spiral, which may result from the multi-plane analysis performed. Figure 6.12 shows the difference between models Gold (left) and Complete (right) with respect to model B23, in units of the magnification map for

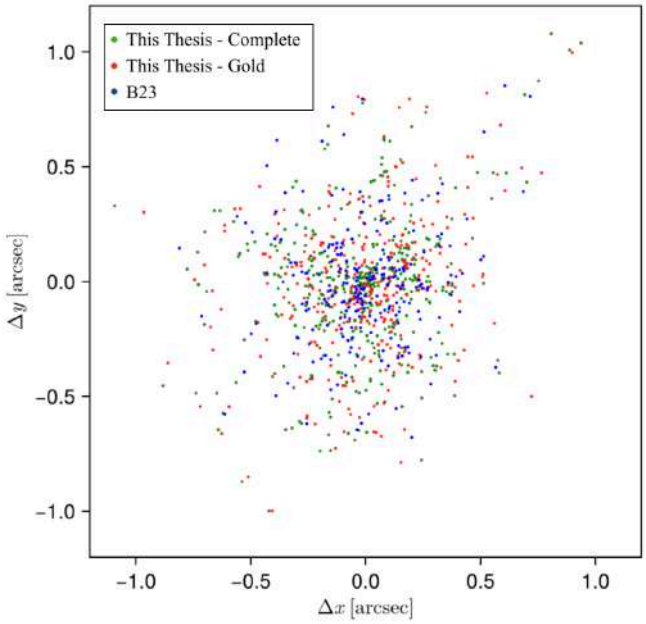

Figure 6.9: Displacements along the x and y directions between the observed and model-predicted multiple images included in models B23 (blue), Gold (red), and Complete (green).

model B23. As expected by looking at Figure 6.11, the main differences arise when the corresponding critical curves disagree. We also show in Fig. 6.13 the relative difference between model Complete and the lens model by R25. Both maps are estimated, as before, at redshift $z = 3.067$.

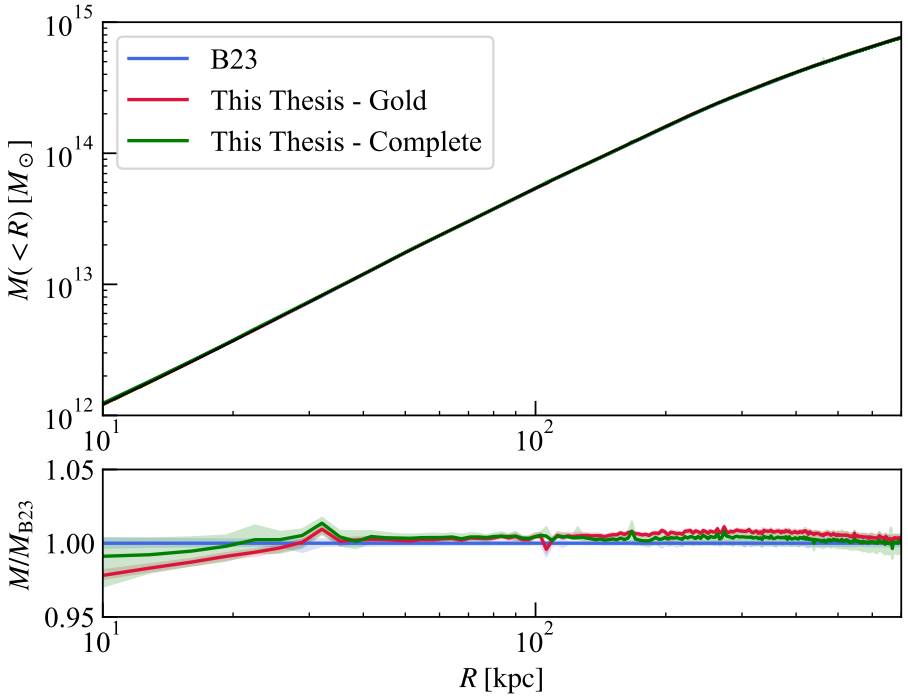

Figure 6.10: *Top*: Cumulative total mass profiles of the galaxy cluster M0416 as a function of the distance from the BCG-N for the three models explored in this Thesis, B23 (blue), Gold (red), and Complete (green). *Bottom*: Ratio between the cumulative total mass profiles with respect to model B23. The shaded band denote, for each model, the interval between the 16th and the 84th quantiles.

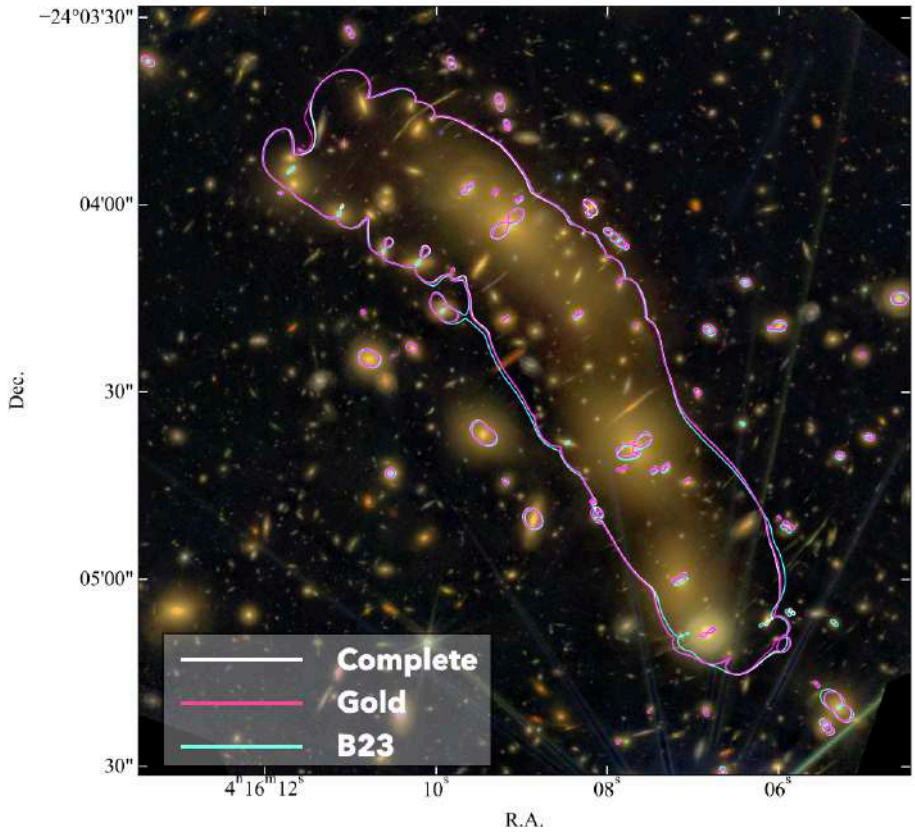

Figure 6.11: Critical curves estimated at redshift $z = 3.067$ for models B23 (cyan), Gold (magenta), and Complete (white).

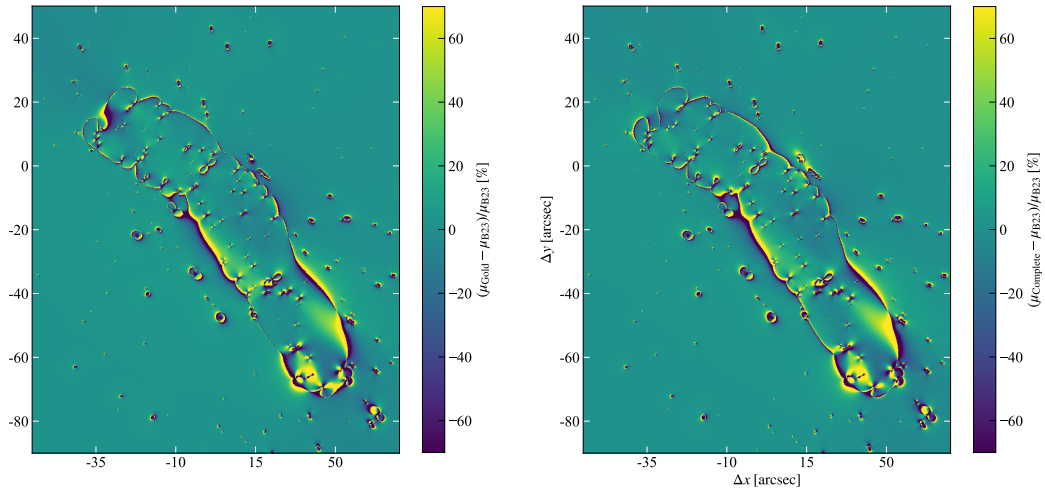

Figure 6.12: Relative difference between the median magnification maps for models Gold (left) and Complete (right) with respect to model B23. The magnification maps are estimated at redshift $z = 3.067$.

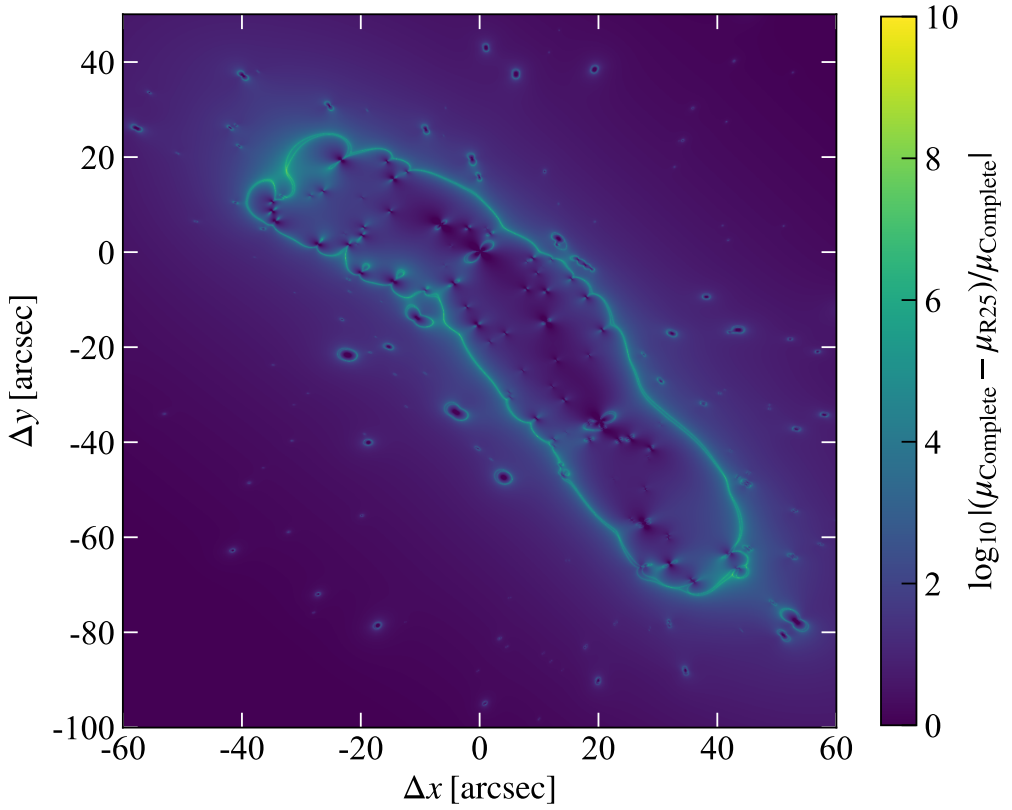

Figure 6.13: Relative difference between the median magnification map for model Complete and the lens model by R25, with respect to the model by R25. The magnification maps are estimated at redshift $z = 3.067$.

CHAPTER 7

Summary and conclusions

The aim of this Thesis was to provide a characterization of future SL analyses of galaxy clusters in the era of Big Data. These studies will follow two different but complementary directions. On the one hand, wide field surveys including *Euclid* and the LSST will provide thousands of cluster lens candidates, thus drastically increasing the number of known systems. Nevertheless, these facilities will provide wide but shallow images, resulting in the detection of a reduced number of multiple images, often without spectroscopic confirmation, whose positions represent the main constraints in SL studies. On the other hand, JWST is providing images of unprecedented quality and depth in the near infrared, allowing us to detect more images and even new knots. These elements are crucial to better constrain the lens models.

In this Thesis, we explored the peculiar case of the ERO galaxy cluster Abell 2390 ($z = 0.231$), which, differently from the targets of the *Euclid* Wide Survey, was given three times the typical exposure time, thus resulting in deeper imaging. We built high-precision SL models by combining, for the first time, the *Euclid* VIS and NISP observations with spectroscopy from MUSE and other archival data, which we fully reanalysed. Thanks to the availability of MUSE data, we were able to measure the stellar velocity dispersion of 22 cluster members, which allowed us to properly calibrate the sub-halo scaling relations used in the modelling and alleviate inherent degeneracies between the cluster- and the galaxy-scale mass components. We performed our analysis with the new software `Gravity.jl`, with which we explored 11 parametrizations of the total mass distribution of the galaxy cluster, with an increasing level of complexity. We were able to reconstruct the total mass distribution of the galaxy cluster and estimate the systematic uncertainty arising from our modelling choices by taking advantage of all the models efficiently explored with `Gravity.jl`. On average, a full optimization of a mass model required approximately 2 hours to be obtained on a 64-core workstation, thus allowing us to test different total mass models in a very limited amount of time. This proved that `Gravity.jl` allows fast and reliable total mass reconstruction of cluster lenses. Thus, it is an ideal tool for SL analyses of large samples of galaxy clusters, such as the one that *Euclid* will deliver. Indeed, based on the forecasts by Boldrin et al. (2012, 2016), we expect that *Euclid* will observe SL features in > 6000 galaxy clusters. These estimates are consistent with the number of SL clusters found in the Q1 data release (Euclid Collaboration: Bergamini et al. 2025). At the same time, `Gravity.jl` will also speed up the analysis of clusters observed at larger depth compared to *Euclid* observations. As suggested by recent JWST observations, deep follow-up observations of clusters identified in the *Euclid* surveys will likely reveal hundreds of families of multiple images. These observations, combined with spectroscopic follow-up, will enable detailed and robust SL mass models.

We then adopted a statistical approach to quantify the expected uncertainties on lensing-derived quantities of interest (including the total mass distribution, critical curves, and magnification maps) when studying *Euclid*-like lensing clusters, in case few constraints are available. We relied once again on the speed achievable with `Gravity.jl` to build hundreds of mock lens models. Our results show that, when very few systems of multiple images are used as constraints, the single lens parameters of the model are poorly constrained, despite the derived quantities, like the cumulative total mass distribution, have a relative total systematic+statistic uncertainty of few percent (less than $\sim 4\%$ as far as the total mass is concerned). When more information is added, the uncertainties decrease (to $\sim 1-2\%$ for the total mass). This study allowed us to forecast the impact on SL analyses following the little number of multiple images that will be detected in *Euclid* images, due to their limited depth with respect to the HST or the JWST. Nevertheless, our findings derive from an already HST-based robust model by Bergamini et al. (2019), with all the multiple images spectroscopically confirmed thanks to MUSE data. Hence, our study can be easily extended by following two further directions. First, since faint images are likely to be undetected, it is reasonable to build lens models by excluding an increasing number of multiple images according to their magnitude, hence resulting in less constraints. Secondly, secure confirmation of the images may not be possible in absence of spectroscopic follow-up. Therefore, we may build lens models for which a subset (e.g., half, or even all) of background families can have a free redshift (as additional free lens parameter). Nevertheless, steps forward are being done in extracting spectra from *Euclid*/NISP.

Finally, we exploited the unprecedented near-IR quality provided by the JWST imaging to push the limits achievable with SL in galaxy clusters, by studying the galaxy cluster MACS J0416.1-2403 ($z = 0.396$). This system was already characterized by the largest set of spectroscopically confirmed multiple images (Bergamini et al. 2023b; Rihtaršič et al. 2025) thanks to the deepest MUSE observations for a cluster to date. We took advantage of the multi-band JWST/NIRCam imaging and JWST/NIRISS and NIRSpec spectroscopy to build a first sample of secure multiple images, increasing by $\sim 140\%$ the number of images included in Bergamini et al. (2023b). We managed to identify additional multiply-lensed knots, thus increasing the number of multiple images to nearly 450, the highest ever for a cluster to date (an increase of $\sim 185\%$ with respect to Bergamini et al. (2023b)). Furthermore, thanks to `Gravity.jl`, we managed to perform multi-plane lensing analyses, differently from previous lensing studies of the same cluster. While identifying the new knots, we also found interesting new multiple images (not spectroscopically-confirmed), by studying their colors and parity. The next natural step would be to add them as additional constraints, and, possibly, to better identify all the knots in the giant arc in the south-west part of the cluster (behind the foreground spiral).

Another natural step to explore would be to further exploit the capabilities that `Gravity.jl` has made possible. Apart from the above-mentioned multi-plane analyses, it would be interesting to perform studies with parametric and non-parametric extended lenses and sources included (see Sect. 3.1.3), e.g. to properly model galaxy G29 in Abell 2390 (Chapter 4) and the giant arcs identified in other clusters.

In addition, thanks to its speed, `Gravity.jl` can be used to study galaxy clusters to perform cosmology studies by including time-delay measurements as further constraints or by exploiting the redshift distribution of the lensed sources (see Section 2.4.3). As briefly mentioned (since it was not the scope of this Thesis), the former approach allows to probe the value of the Hubble constant, whereas the latter the values of the

equation-of-state parameter for dark energy (ω_0) and the matter density parameter (Ω_m), since the redshift distribution of the sources is sensitive to the geometry of the Universe, hence on the values of these parameters. Galaxy clusters are ideal for these studies, thanks to the hundreds of multiple images of distant sources distributed in redshift. However, SL studies in galaxy clusters to recover the values of ω_0 and Ω_m are so far limited to few systems (see Caminha et al. 2022a). Nevertheless, it is possible to easily extend this methodology to other systems and obtain results in little time with `Gravity.jl`. The increase of SL systems suitable for cosmography will then help reduce the statistical uncertainty on the values of these cosmological parameters, thus making this method very competitive with respect to others. This method can also be applied for galaxy-scale systems, in particular, for double Einstein rings, whose number is expected to step from the few already known to tens or hundreds.

Bibliography

Abell, G. O. 1958, *Astrophys. J. Suppl.*, 3, 211

Abell, G. O., Corwin, Jr., H. G., & Olowin, R. P. 1989, *Astrophys. J. Suppl.*, 70, 1

Abolfathi, B., Aguado, D. S., Aguilar, G., et al. 2018, *Astrophys. J. Suppl.*, 235, 42

Abraham, R. G., Smecker-Hane, T. A., Hutchings, J. B., et al. 1996, *Astrophys. J.*, 471, 694

Abriola, D., Lombardi, M., Grillo, C., et al. 2025, *Astron. Astrophys.*, 704, A338

Acebron, A., Alon, M., Zitrin, A., et al. 2019, *Astrophys. J.*, 874, 132

Acebron, A., Cibirka, N., Zitrin, A., et al. 2018, *Astrophys. J.*, 858, 42

Acebron, A., Grillo, C., Bergamini, P., et al. 2022, *Astron. Astrophys.*, 668, A142

Acebron, A., Grillo, C., Suyu, S. H., et al. 2024, *Astrophys. J.*, 976, 110

Acebron, A., Jullo, E., Limousin, M., et al. 2017, *Mon. Not. R. Astron. Soc.*, 470, 1809

Acebron, A., Schuldt, S., Grillo, C., et al. 2023, *Astron. Astrophys.*, 680, L9

Acevedo Barroso, J. A., O'Riordan, C. M., Clément, B., et al. 2024, arXiv e-prints, arXiv:2408.06217

Adams, N. J., Conselice, C. J., Ferreira, L., et al. 2023, *Mon. Not. R. Astron. Soc.*, 518, 4755

Allen, S. W., Ettori, S., & Fabian, A. C. 2001, *Mon. Not. R. Astron. Soc.*, 324, 877

Annunziatella, M., Biviano, A., Mercurio, A., et al. 2014, *Astron. Astrophys.*, 571, A80

Annunziatella, M., Bonamigo, M., Grillo, C., et al. 2017, *Astrophys. J.*, 851, 81

Asada, Y., Sawicki, M., Abraham, R., et al. 2024, *Mon. Not. R. Astron. Soc.*, 527, 11372

Atek, H., Chemerynska, I., Wang, B., et al. 2023a, *Mon. Not. R. Astron. Soc.*, 524, 5486

Atek, H., Gavazzi, R., Weaver, J. R., et al. 2024, arXiv e-prints, arXiv:2405.13504

Atek, H., Richard, J., Kneib, J.-P., & Schaerer, D. 2018, *Mon. Not. R. Astron. Soc.*, 479, 5184

Atek, H., Shuntov, M., Furtak, L. J., et al. 2023b, *Mon. Not. R. Astron. Soc.*, 519, 1201

Bacon, R., Accardo, M., Adjali, L., et al. 2010, in Society of Photo-Optical Instrumentation Engineers (SPIE) Conference Series, Vol. 7735, Ground-based and Airborne Instrumentation for Astronomy III, ed. I. S. McLean, S. K. Ramsay, & H. Takami, 773508

Balestra, I., Mercurio, A., Sartoris, B., et al. 2016, *Astrophys. J. Suppl.*, 224, 33

Bartelmann, M. & Schneider, P. 2001, *Physics Reports*, 340, 291

Beichman, C. A., Rieke, M., Eisenstein, D., et al. 2012, in Society of Photo-Optical Instrumentation Engineers (SPIE) Conference Series, Vol. 8442, Space Telescopes and Instrumentation 2012: Optical, Infrared, and Millimeter Wave, ed. M. C. Clampin, G. G. Fazio, H. A. MacEwen, & J. M. Oschmann, Jr., 84422N

Bender, R., Burstein, D., & Faber, S. M. 1992, *Astrophys. J.*, 399, 462

Bergamini, P., Acebron, A., Grillo, C., et al. 2023a, *Astrophys. J.*, 952, 84

Bergamini, P., Grillo, C., Rosati, P., et al. 2023b, *Astron. Astrophys.*, 674, A79
Bergamini, P., Rosati, P., Mercurio, A., et al. 2019, *Astron. Astrophys.*, 631, A130
Bergamini, P., Rosati, P., Vanzella, E., et al. 2021, *Astron. Astrophys.*, 645, A140
Bergamini, P., Schuldt, S., Acebron, A., et al. 2024, *Astron. Astrophys.*, 682, L2
Bertin, E. 2006, in Astronomical Society of the Pacific Conference Series, Vol. 351, Astronomical Data Analysis Software and Systems XV, ed. C. Gabriel, C. Arviset, D. Ponz, & S. Enrique, 112
Bertin, E. & Arnouts, S. 1996, *Astron. Astrophys. Supp. Ser.*, 117, 393
Bertin, E., Schefer, M., Apostolakos, N., et al. 2022, SourceXtractor++: Extracts sources from astronomical images, Astrophysics Source Code Library, record ascl:2212.018
Betancourt, M. 2017, arXiv e-prints, arXiv:1706.01520
Bezanson, J., Edelman, A., Karpinski, S., & Shah, V. B. 2014, arXiv e-prints, arXiv:1411.1607
Bezanson, R., Labbe, I., Whitaker, K. E., et al. 2024, *Astrophys. J.*, 974, 92
Bezecourt, J. & Soucail, G. 1997, *Astron. Astrophys.*, 317, 661
Biviano, A. 2000, in Constructing the Universe with Clusters of Galaxies, ed. F. Durret & D. Gerbal, 1
Biviano, A., Rosati, P., Balestra, I., et al. 2013, *Astron. Astrophys.*, 558, A1
Blandford, R. & Narayan, R. 1986, *Astrophys. J.*, 310, 568
Boehringer, H., Tanaka, Y., Mushotzky, R. F., Ikebe, Y., & Hattori, M. 1998, *Astron. Astrophys.*, 334, 789
Böker, T., Beck, T. L., Birkmann, S. M., et al. 2023, *Publ. Astron. Soc. Pac.*, 135, 038001
Boldrin, M., Giocoli, C., Meneghetti, M., & Moscardini, L. 2012, *Mon. Not. R. Astron. Soc.*, 427, 3134
Boldrin, M., Giocoli, C., Meneghetti, M., et al. 2016, *Mon. Not. R. Astron. Soc.*, 457, 2738
Bonamigo, M., Grillo, C., Ettori, S., et al. 2017, *Astrophys. J.*, 842, 132
Bonamigo, M., Grillo, C., Ettori, S., et al. 2018, *Astrophys. J.*, 864, 98
Bouwens, R. J., Illingworth, G., Ellis, R. S., Oesch, P., & Stefanon, M. 2022, *Astrophys. J.*, 940, 55
Bradač, M., Clowe, D., Gonzalez, A. H., et al. 2006, *Astrophys. J.*, 652, 937
Broadhurst, T., Takada, M., Umetsu, K., et al. 2005, *Astrophys. J. Lett.*, 619, L143
Burke, W. L. 1981, *Astrophys. J. Lett.*, 244, L1
Caminha, G. B., Grillo, C., Rosati, P., et al. 2016, *Astron. Astrophys.*, 587, A80
Caminha, G. B., Grillo, C., Rosati, P., et al. 2017, *Astron. Astrophys.*, 600, A90
Caminha, G. B., Rosati, P., Grillo, C., et al. 2019, *Astron. Astrophys.*, 632, A36
Caminha, G. B., Suyu, S. H., Grillo, C., & Rosati, P. 2022a, *Astron. Astrophys.*, 657, A83
Caminha, G. B., Suyu, S. H., Mercurio, A., et al. 2022b, *Astron. Astrophys.*, 666, L9
Cappellari, M. 2023, *Mon. Not. R. Astron. Soc.*, 526, 3273
Cappellari, M. & Emsellem, E. 2004, *Publ. Astron. Soc. Pac.*, 116, 138
Cappellari, M., Scott, N., Alatalo, K., et al. 2013, MNRAS, 432, 1709
Carniani, S., Hainline, K., D'Eugenio, F., et al. 2024, Nature, 633, 318
Castellano, M., Fontana, A., Treu, T., et al. 2023, *Astrophys. J. Lett.*, 948, L14
Cavaliere, A. G., Gursky, H., & Tucker, W. H. 1971, *Nature*, 231, 437
Cha, S. & Jee, M. J. 2022, *Astrophys. J.*, 931, 127
Chen, W., Kelly, P. L., Diego, J. M., et al. 2019, *Astrophys. J.*, 881, 8
Chopin, N. & Robert, C. 2008, arXiv e-prints, arXiv:0801.3887

Clowe, D., Bradač, M., Gonzalez, A. H., et al. 2006, *Astrophys. J. Lett.*, 648, L109
Coe, D., Salmon, B., Bradač, M., et al. 2019, *Astrophys. J.*, 884, 85
Coe, D., Umetsu, K., Zitrin, A., et al. 2012, *Astrophys. J.*, 757, 22
Colless, M., Dalton, G., Maddox, S., et al. 2001, *Mon. Not. R. Astron. Soc.*, 328, 1039
Collett, T. E. 2015, *Astrophys. J.*, 811, 20
Comrie, A., Wang, K.-S., Hsu, S.-C., et al. 2021, CARTA: The Cube Analysis and Rendering Tool for Astronomy
Cuillandre, J. C., Bertin, E., Bolzonella, M., et al. 2024, arXiv e-prints, arXiv:2405.13496
De Grandi, S., Guzzo, L., Böhringer, H., et al. 1999, *Astrophys. J. Lett.*, 513, L17
DESI Collaboration, Aghamousa, A., Aguilar, J., et al. 2016, arXiv e-prints, arXiv:1611.00037
Diego, J. M., Adams, N. J., Willner, S. P., et al. 2024a, *Astron. Astrophys.*, 690, A114
Diego, J. M., Broadhurst, T., Zitrin, A., et al. 2015, *Mon. Not. R. Astron. Soc.*, 451, 3920
Diego, J. M., Congedo, G., Gavazzi, R., et al. 2025, arXiv e-prints, arXiv:2507.08545
Diego, J. M., Li, S. K., Meena, A. K., et al. 2024b, VizieR Online Data Catalog: Strong lensing dataset in MACS J0416.1-2403 (Diego+, 2024), VizieR On-line Data Catalog: J/A+A/681/A124. Originally published in: 2024A&A...681A.124D
Diego, J. M., Protopapas, P., Sandvik, H. B., & Tegmark, M. 2005, *Mon. Not. R. Astron. Soc.*, 360, 477
Diego, J. M., Tegmark, M., Protopapas, P., & Sandvik, H. B. 2007, *Mon. Not. R. Astron. Soc.*, 375, 958
Djorgovski, S. & Davis, M. 1987, *Astrophys. J.*, 313, 59
Doyon, R., Hutchings, J. B., Beaulieu, M., et al. 2012, in Society of Photo-Optical Instrumentation Engineers (SPIE) Conference Series, Vol. 8442, Space Telescopes and Instrumentation 2012: Optical, Infrared, and Millimeter Wave, ed. M. C. Clampin, G. G. Fazio, H. A. MacEwen, & J. M. Oschmann, Jr., 84422R
Doyon, R., Willott, C. J., Hutchings, J. B., et al. 2023, *Publ. Astron. Soc. Pac.*, 135, 098001
Dressler, A., Lynden-Bell, D., Burstein, D., et al. 1987, *Astrophys. J.*, 313, 42
Dyson, F. W., Eddington, A. S., & Davidson, C. 1920, Philosophical Transactions of the Royal Society of London Series A, 220, 291
Ebeling, H., Edge, A. C., Bohringer, H., et al. 1998, *Mon. Not. R. Astron. Soc.*, 301, 881
Ebeling, H., Edge, A. C., & Henry, J. P. 2001, *Astrophys. J.*, 553, 668
Ebeling, H., Edge, A. C., Mantz, A., et al. 2010, *Mon. Not. R. Astron. Soc.*, 407, 83
Einstein, A. 1915, Sitzungsber. preuss. Akad. Wiss., 47, 831
Einstein, A. 1936, Science, 84, 506
Elíasdóttir, Á., Limousin, M., Richard, J., et al. 2007, arXiv e-prints, arXiv:0710.5636
Ettori, S. & Eckert, D. 2022, *Astron. Astrophys.*, 657, L1
Ettori, S., Ghirardini, V., Eckert, D., et al. 2019, *Astron. Astrophys.*, 621, A39
Euclid Collaboration: Bergamini, P., Meneghetti, M., Acebron, A., et al. 2025, arXiv:2503.15330
Euclid Collaboration: Cropper, M., Al-Bahlawan, A., Amiaux, J., et al. 2024, arXiv e-prints, arXiv:2405.13492
Euclid Collaboration: Gillard, W., Maciaszek, T., Prieto, E., et al. 2025, arXiv e-prints, arXiv:2506.08378
Euclid Collaboration: Jahnke, K., Gillard, W., Schirmer, M., et al. 2024, arXiv e-prints, arXiv:2405.13493
Euclid Collaboration: Mellier, Y., Abdurro'uf, Acevedo Barroso, J. A., et al. 2024, arXiv

e-prints, arXiv:2405.13491
Euclid Collaboration: Scaramella, R., Amiaux, J., Mellier, Y., et al. 2022, *Astron. Astrophys.*, 662, A112
Faber, S. M. & Jackson, R. E. 1976, *Astrophys. J.*, 204, 668
Fabricant, D., Fata, R., Roll, J., et al. 2005, *Publ. Astron. Soc. Pac.*, 117, 1411
Feix, M., Zhao, H., Fedeli, C., Pestaña, J. L. G., & Hoekstra, H. 2010, *Phys. Rev. D*, 82, 124003
Foreman-Mackey, D., Hogg, D. W., Lang, D., & Goodman, J. 2013, *Publ. Astron. Soc. Pac.*, 125, 306
Forman, W., Jones, C., Murray, S., & Giacconi, R. 1978, *Astrophys. J. Lett.*, 225, L1
Fort, B. 1990, in Gravitational Lensing, ed. Y. Mellier, B. Fort, & G. Soucail, Vol. 360, 219–229
Furtak, L. J., Zitrin, A., Weaver, J. R., et al. 2023, *Mon. Not. R. Astron. Soc.*, 523, 4568
Gaia Collaboration: Vallenari, A., Brown, A. G. A., Prusti, T., et al. 2023, *Astron. Astrophys.*, 674, A1
Geller, M. J. & Huchra, J. P. 1989, Science, 246, 897
Ghosh, A., Adams, D., Williams, L. L. R., et al. 2023, *Mon. Not. R. Astron. Soc.*, 525, 2519
Giacconi, R., Murray, S., Gursky, H., et al. 1972, *Astrophys. J.*, 178, 281
Gilbank, D. G., Gladders, M. D., Yee, H. K. C., & Hsieh, B. C. 2011, *Astron. J.*, 141, 94
Gioia, I. M., Maccacaro, T., Schild, R. E., et al. 1990, *Astrophys. J. Suppl.*, 72, 567
Girardi, M., Giuricin, G., Mardirossian, F., Mezzetti, M., & Boschin, W. 1998, *Astrophys. J.*, 505, 74
Gladders, M. D. 2000, in American Astronomical Society Meeting Abstracts, Vol. 197, American Astronomical Society Meeting Abstracts, 57.03
Gladders, M. D., López-Cruz, O., Yee, H. K. C., & Kodama, T. 1998, *Astrophys. J.*, 501, 571
Gladders, M. D. & Yee, H. K. C. 2000, *Astron. J.*, 120, 2148
Glasse, A., Rieke, G. H., Bauwens, E., et al. 2015, *Publ. Astron. Soc. Pac.*, 127, 686
Gledhill, R., Strait, V., Desprez, G., et al. 2024, *Astrophys. J.*, 973, 77
Golse, G. & Kneib, J. P. 2002, *Astron. Astrophys.*, 390, 821
Gómez, P. L., Valkonen, L. E., Romer, A. K., et al. 2012, *Astron. J.*, 144, 79
Gonneau, A., Lyubenova, M., Lançon, A., et al. 2020, *Astron. Astrophys.*, 634, A133
Goodman, J. & Weare, J. 2010, Communications in Applied Mathematics and Computational Science, 5, 65
Granata, G., Bergamini, P., Grillo, C., et al. 2023, *Astron. Astrophys.*, 679, A124
Granata, G., Caminha, G. B., Ertl, S., et al. 2024, arXiv e-prints, arXiv:2412.13250
Granata, G., Mercurio, A., Grillo, C., et al. 2022, *Astron. Astrophys.*, 659, A24
Grillo, C., Gobat, R., Presotto, V., et al. 2014, *Astrophys. J.*, 786, 11
Grillo, C., Karman, W., Suyu, S. H., et al. 2016, *Astrophys. J.*, 822, 78
Grillo, C., Pagano, L., Rosati, P., & Suyu, S. H. 2024, *Astron. Astrophys.*, 684, L23
Grillo, C., Rosati, P., Suyu, S. H., et al. 2018, *Astrophys. J.*, 860, 94
Grillo, C., Rosati, P., Suyu, S. H., et al. 2020, *Astrophys. J.*, 898, 87
Grillo, C., Suyu, S. H., Rosati, P., et al. 2015, *Astrophys. J.*, 800, 38
Guzzo, L., Böhringer, H., Schuecker, P., et al. 1999, The Messenger, 95, 27
Hilbert, S., Hartlap, J., White, S. D. M., & Schneider, P. 2009, *Astron. Astrophys.*, 499, 31
Hinton, S. R., Davis, T. M., Lidman, C., Glazebrook, K., & Lewis, G. F. 2016, Astronomy and Computing, 15, 61
Hoag, A., Huang, K. H., Treu, T., et al. 2016, *Astrophys. J.*, 831, 182

Ivezić, Ž., Kahn, S. M., Tyson, J. A., et al. 2019, *Astrophys. J.*, 873, 111
Jakobsen, P., Ferruit, P., Alves de Oliveira, C., et al. 2022, *Astron. Astrophys.*, 661, A80
Jauzac, M., Richard, J., Jullo, E., et al. 2015, *Mon. Not. R. Astron. Soc.*, 452, 1437
Johnson, T. L., Rigby, J. R., Sharon, K., et al. 2017, *Astrophys. J. Lett.*, 843, L21
Johnson, T. L., Sharon, K., Bayliss, M. B., et al. 2014, *Astrophys. J.*, 797, 48
Jullo, E., Kneib, J. P., Limousin, M., et al. 2007, New Journal of Physics, 9, 447
Jullo, E., Natarajan, P., Kneib, J. P., et al. 2010, Science, 329, 924
Karman, W., Caputi, K. I., Caminha, G. B., et al. 2017, *Astron. Astrophys.*, 599, A28
Karman, W., Caputi, K. I., Grillo, C., et al. 2015, *Astron. Astrophys.*, 574, A11
Kaurov, A. A., Dai, L., Venumadhav, T., Miralda-Escudé, J., & Frye, B. 2019, *Astrophys. J.*, 880, 58
Kawamata, R., Oguri, M., Ishigaki, M., Shimasaku, K., & Ouchi, M. 2016, *Astrophys. J.*, 819, 114
Keeton, C. R. 2010, General Relativity and Gravitation, 42, 2151
Kneib, J. P., Ellis, R. S., Smail, I., Couch, W. J., & Sharples, R. M. 1996, *Astrophys. J.*, 471, 643
Kovner, I. 1987, *Astrophys. J.*, 316, 52
Kravtsov, A. V. & Borgani, S. 2012, *Annu. Rev. Astron. Astrophys.*, 50, 353
Kümmel, M., Álvarez-Ayllón, A., Bertin, E., et al. 2022, arXiv e-prints, arXiv:2212.02428
Le Borgne, J. F., Mathez, G., Mellier, Y., et al. 1991, *Astron. Astrophys. Supp. Ser.*, 88, 133
Le Fèvre, O., Saisse, M., Mancini, D., et al. 2003, in Society of Photo-Optical Instrumentation Engineers (SPIE) Conference Series, Vol. 4841, Instrument Design and Performance for Optical/Infrared Ground-based Telescopes, ed. M. Iye & A. F. M. Moorwood, 1670–1681
Liesenborgs, J., De Rijcke, S., & Dejonghe, H. 2006, *Mon. Not. R. Astron. Soc.*, 367, 1209
Limousin, M., Kneib, J.-P., & Natarajan, P. 2005, *Mon. Not. R. Astron. Soc.*, 356, 309
Lombardi, M. 2024, *Astron. Astrophys.*, 690, A346
Lotz, J. M., Koekemoer, A., Coe, D., et al. 2017, *Astrophys. J.*, 837, 97
Lynds, R. & Petrosian, V. 1986, in Bulletin of the American Astronomical Society, Vol. 18, 1014
Magaña, J., Acebrón, A., Motta, V., et al. 2018, *Astrophys. J.*, 865, 122
Mahler, G., Jauzac, M., Richard, J., et al. 2023, *Astrophys. J.*, 945, 49
Mamon, G. A., Biviano, A., & Boué, G. 2013, *Mon. Not. R. Astron. Soc.*, 429, 3079
Mann, A. W. & Ebeling, H. 2012, *Mon. Not. R. Astron. Soc.*, 420, 2120
Markevitch, M., Gonzalez, A. H., David, L., et al. 2002, *Astrophys. J. Lett.*, 567, L27
McKenzie, R. H. 1985, Journal of Mathematical Physics, 26, 1592
Mellier, Y., Soucail, G., Fort, B., Le Borgne, J. F., & Pello, R. 1990, in Gravitational Lensing, ed. Y. Mellier, B. Fort, & G. Soucail, Vol. 360, 261
Meneghetti, M. 2022, Introduction to Gravitational Lensing: With Python Examples
Meneghetti, M., Cui, W., Rasia, E., et al. 2023, *Astron. Astrophys.*, 678, L2
Meneghetti, M., Davoli, G., Bergamini, P., et al. 2020, Science, 369, 1347
Meneghetti, M., Fedeli, C., Pace, F., Gottlöber, S., & Yepes, G. 2010a, *Astron. Astrophys.*, 519, A90
Meneghetti, M., Natarajan, P., Coe, D., et al. 2017, *Mon. Not. R. Astron. Soc.*, 472, 3177
Meneghetti, M., Ragagnin, A., Borgani, S., et al. 2022, *Astron. Astrophys.*, 668, A188
Meneghetti, M., Rasia, E., Merten, J., et al. 2010b, *Astron. Astrophys.*, 514, A93

Meneghetti, M., Rasia, E., Vega, J., et al. 2014, *Astrophys. J.*, 797, 34
Mercurio, A., Rosati, P., Biviano, A., et al. 2021, *Astron. Astrophys.*, 656, A147
Merten, J., Meneghetti, M., Postman, M., et al. 2015, *Astrophys. J.*, 806, 4
Monna, A., Seitz, S., Greisel, N., et al. 2014, *Mon. Not. R. Astron. Soc.*, 438, 1417
Naidu, R. P., Oesch, P. A., Brammer, G., et al. 2025, arXiv e-prints, arXiv:2505.11263
Natarajan, P., Williams, L. L. R., Bradač, M., et al. 2024, [Space Science Reviews], 220, 19
Navarro, J. F., Frenk, C. S., & White, S. D. M. 1996, *Astrophys. J.*, 462, 563
Navarro, J. F., Frenk, C. S., & White, S. D. M. 1997, *Astrophys. J.*, 490, 493
Neal, R. 2011, in Handbook of Markov Chain Monte Carlo, 113–162
Noirot, G., Desprez, G., Asada, Y., et al. 2023, *Mon. Not. R. Astron. Soc.*, 525, 1867
Oguri, M. 2010a, glafic: Software Package for Analyzing Gravitational Lensing, Astrophysics Source Code Library, record ascl:1010.012
Oguri, M. 2010b, *Publ. Astron. Soc. Jpn.*, 62, 1017
Okabe, N. & Smith, G. P. 2016, *Mon. Not. R. Astron. Soc.*, 461, 3794
Olmstead, A., Rigby, J. R., Swinbank, M., & Veilleux, S. 2014, *Astron. J.*, 148, 65
Paczynski, B. 1987, *Nature*, 325, 572
Pelló, R., Kneib, J. P., Le Borgne, J. F., et al. 1999, *Astron. Astrophys.*, 346, 359
Pello, R., Le Borgne, J.-F., Soucail, G., Mellier, Y., & Sanahuja, B. 1991, *Astrophys. J.*, 366, 405
Pierre, M., Le Borgne, J. F., Soucail, G., & Kneib, J. P. 1996, *Astron. Astrophys.*, 311, 413
Postman, M., Coe, D., Benítez, N., et al. 2012, *Astrophys. J. Suppl.*, 199, 25
Rahaman, M., Raja, R., Datta, A., et al. 2021, *Mon. Not. R. Astron. Soc.*, 505, 480
Refsdal, S. 1964, *Mon. Not. R. Astron. Soc.*, 128, 307
Richard, J., Claeyssens, A., Lagattuta, D., et al. 2021, *Astron. Astrophys.*, 646, A83
Richard, J., Patricio, V., Martinez, J., et al. 2015, *Mon. Not. R. Astron. Soc.*, 446, L16
Rieke, M. J., Baum, S. A., Beichman, C. A., et al. 2003, in Society of Photo-Optical Instrumentation Engineers (SPIE) Conference Series, Vol. 4850, IR Space Telescopes and Instruments, ed. J. C. Mather, 478–485
Rieke, M. J., Kelly, D., & Horner, S. 2005, in Society of Photo-Optical Instrumentation Engineers (SPIE) Conference Series, Vol. 5904, Cryogenic Optical Systems and Instruments XI, ed. J. B. Heaney & L. G. Burriesci, 1–8
Rieke, M. J., Kelly, D. M., Misselt, K., et al. 2023, *Publ. Astron. Soc. Pac.*, 135, 028001
Rigby, J., Perrin, M., McElwain, M., et al. 2023, *Publ. Astron. Soc. Pac.*, 135, 048001
Rigby, J. R., Bayliss, M. B., Sharon, K., et al. 2018, *Astron. J.*, 155, 104
Rihtaršič, G., Bradač, M., Desprez, G., et al. 2025, *Astron. Astrophys.*, 696, A15
Roberts-Borsani, G., Treu, T., Chen, W., et al. 2023, *Nature*, 618, 480
Rodney, S. A., Balestra, I., Bradac, M., et al. 2018, Nature Astronomy, 2, 324
Rosati, P., Balestra, I., Grillo, C., et al. 2014, The Messenger, 158, 48
Rousseeuw, P. J. & Van Driessen, K. 2006, Data Min Knowl Disc, 12, 29
Salmon, B., Coe, D., Bradley, L., et al. 2018, *Astrophys. J. Lett.*, 864, L22
Sartoris, B., Biviano, A., Rosati, P., et al. 2014, *Astrophys. J. Lett.*, 783, L11
Schmidt, K. B., Treu, T., Brammer, G. B., et al. 2014, *Astrophys. J. Lett.*, 782, L36
Schneider, P. 1984, *Astron. Astrophys.*, 140, 119
Schneider, P. 1985, *Astron. Astrophys.*, 143, 413
Schneider, P. 2006, Extragalactic Astronomy and Cosmology
Schneider, P., Ehlers, J., & Falco, E. E. 1992, Gravitational Lenses

Schrabback, T., Congedo, G., Gavazzi, R., et al. 2025, arXiv e-prints, arXiv:2507.07629
Sebesta, K., Williams, L. L. R., Mohammed, I., Saha, P., & Liesenborgs, J. 2016, *Mon. Not. R. Astron. Soc.*, 461, 2126
Seitz, S. & Schneider, P. 1992, *Astron. Astrophys.*, 265, 1
Shapiro, I. I. 1964, PhysRevLett., 13, 789
Skilling, J. 2004, in American Institute of Physics Conference Series, Vol. 735, Bayesian Inference and Maximum Entropy Methods in Science and Engineering: 24th International Workshop on Bayesian Inference and Maximum Entropy Methods in Science and Engineering, ed. R. Fischer, R. Preuss, & U. V. Toussaint (AIP), 395–405
Smith, S. 1936, *Astrophys. J.*, 83, 23
Sohn, J., Fabricant, D. G., Geller, M. J., Hwang, H. S., & Diaferio, A. 2020, *Astrophys. J.*, 902, 17
Soto, K. T., Lilly, S. J., Bacon, R., Richard, J., & Conseil, S. 2016, *Mon. Not. R. Astron. Soc.*, 458, 3210
Soucail, G., Fort, B., Mellier, Y., & Picat, J. P. 1987, *Astron. Astrophys.*, 172, L14
Soucail, G., Mellier, Y., Fort, B., Mathez, G., & Cailloux, M. 1988, *Astron. Astrophys.*, 191, L19
Steinhardt, C. L., Jauzac, M., Acebron, A., et al. 2020, The Astrophysical Journal Supplement Series, 247, 64
Surjanovic, N., Biron-Lattes, M., Tiede, P., et al. 2023, arXiv e-prints, arXiv:2308.09769
Surjanovic, N., Syed, S., Bouchard-Côté, A., & Campbell, T. 2022, arXiv e-prints, arXiv:2206.00080
Suyu, S. H. & Halkola, A. 2010, *Astron. Astrophys.*, 524, A94
Swinbank, A. M., Bower, R. G., Smith, G. P., et al. 2006, *Mon. Not. R. Astron. Soc.*, 368, 1631
Syed, S., Bouchard-Côté, A., Deligiannidis, G., & Doucet, A. 2019, arXiv e-prints, arXiv:1905.02939
Torres-Ballesteros, D. A. & Castañeda, L. 2023, *Mon. Not. R. Astron. Soc.*, 518, 4494
Torri, E., Meneghetti, M., Bartelmann, M., et al. 2004, *Mon. Not. R. Astron. Soc.*, 349, 476
Treu, T., Roberts-Borsani, G., Bradac, M., et al. 2022, *Astrophys. J.*, 935, 110
Treu, T., Schmidt, K. B., Brammer, G. B., et al. 2015, *Astrophys. J.*, 812, 114
Trümper, J. 1984, MPE Report, 184, 254
Umetsu, K., Medezinski, E., Nonino, M., et al. 2014, *Astrophys. J.*, 795, 163
Umetsu, K., Medezinski, E., Nonino, M., et al. 2012, *Astrophys. J.*, 755, 56
Umetsu, K., Sereno, M., Lieu, M., et al. 2020, *Astrophys. J.*, 890, 148
Umetsu, K., Sereno, M., Tam, S.-I., et al. 2018, *Astrophys. J.*, 860, 104
Umetsu, K., Zitrin, A., Gruen, D., et al. 2016, *Astrophys. J.*, 821, 116
Vanzella, E., Caminha, G. B., Rosati, P., et al. 2021, VizieR Online Data Catalog: VLT/MUSE MACS J0416.1-2403 redshift catalogue (Vanzella+, 2021), VizieR On-line Data Catalog: J/A+A/646/A57. Originally published in: 2021A&A...646A..57V
Vikhlinin, A. A., Kravtsov, A. V., Markevich, M. L., Sunyaev, R. A., & Churazov, E. M. 2014, Physics Uspekhi, 57, 317
Voges, W., Aschenbach, B., Boller, T., et al. 1999, *Astron. Astrophys.*, 349, 389
Walker, S., Simionescu, A., Nagai, D., et al. 2019, Space Science Reviews, 215, 7
Walsh, D., Carswell, R. F., & Weymann, R. J. 1979, *Nature*, 279, 381
Wang, J., Bose, S., Frenk, C. S., et al. 2020, Nature, 585, 39
Williams, L. L. R. & Saha, P. 2004, *Astron. J.*, 128, 2631

Willott, C. J., Doyon, R., Albert, L., et al. 2022, *Publ. Astron. Soc. Pac.*, 134, 025002
Windhorst, R. A., Cohen, S. H., Jansen, R. A., et al. 2023, *Astron. J.*, 165, 13
Wright, G. S., Rieke, G. H., Glasse, A., et al. 2023, *Publ. Astron. Soc. Pac.*, 135, 048003
Yan, H., Ma, Z., Sun, B., et al. 2023, *Astrophys. J. Suppl.*, 269, 43
York, D. G., Adelman, J., Anderson, Jr., J. E., et al. 2000, *Astron. J.*, 120, 1579
Zehavi, I., Zheng, Z., Weinberg, D. H., et al. 2011, *Astrophys. J.*, 736, 59
Zitrin, A., Fabris, A., Merten, J., et al. 2015, *Astrophys. J.*, 801, 44
Zitrin, A., Menanteau, F., Hughes, J. P., et al. 2013, *Astrophys. J. Lett.*, 770, L15
Zwicky, F. 1933, Helvetica Physica Acta, 6, 110
Zwicky, F. 1937a, *Astrophys. J.*, 86, 217
Zwicky, F. 1937b, Physical Review, 51, 679
Zwicky, F., Herzog, E., & Wild, P. 1968, Catalogue of galaxies and of clusters of galaxies
Zwicky, F., Herzog, E., Wild, P., Karpowicz, M., & Kowal, C. T. 1961, Catalogue of galaxies and of clusters of galaxies, Vol. I

List of Publications

As of January 2026

Refereed publications

- *An improved Magellan weak lensing analysis of the galaxy cluster Abell 2744*, **Abriola, D.**, Della Pergola, D., Lombardi, M. and 4 additional co-authors, 2024, *Astron. Astrophys.*, 684, A193 – [Paper page]
- *Euclid: Early Release Observations – A preview of the Euclid era through a galaxy cluster magnifying lens*, Atek, H., Gavazzi, R., Weaver, J. R., and 200 additional co-authors (including **Abriola, D.**), 2025, *Astron. Astrophys.*, 697, A15 – [Paper page]
- *A new quasar strongly-lensed candidate by the galaxy cluster WHJ0400–27 with a* $18''$ *image-separation*, Bazzanini, L., Angora, G., Scialpi, M., and 14 additional co-authors (including **Abriola, D.**), 2025, *Astron. Astrophys.*, 698, A29 –[Paper page]
- *Euclid Quick Data Release (Q1). The first catalogue of strong-lensing galaxy clusters*, *Euclid* collaboration: Bergamini, P., Meneghetti, M., Acebron, A., and 364 additional co-authors (including **Abriola, D.**). Paper submitted as part of the *Astron. Astrophys.* Special Issue *Euclid Quick Data Release (Q1)* – [arXiv e-print page]
- *Euclid preparation. LXXIV. Euclidised observations of Hubble Frontier Fields and CLASH galaxy clusters*, *Euclid* collaboration: Bergamini, P., Meneghetti, M., Angora, G., and 262 additional co-authors (including **Abriola, D.**) – accepted for publication by *Astron. Astrophys.* – [arXiv e-print page]
- *Parametric strong lensing model of the galaxy cluster Abell 2390 from Euclid and MUSE observations*, **Abriola, D.**, Lombardi, M., Grillo, C., and 14 additional co-authors, 2025, *Astron. Astrophys.* 704, A338 – [Paper page]

Publications under review

- *Euclid Quick Data Release (Q1). TBD. Searching for giant gravitational arcs in galaxy clusters with mask region-based CNNs*, *Euclid* collaboration: Bazzanini, L., Angora, G., Bergamini, P., and 17 additional co-authors (including **Abriola, D.**) – internal review within the Euclid Consortium Editorial Board

Publications in preparation

- *Strong gravitational lensing in galaxy clusters in the wide field surveys era: a statistical approach. I. Reduced number of multiple images*, **Abriola, D.**, Lombardi, M., Grillo, C., and 1 additional co-author.

Publications in conference proceedings

- *Combined strong and weak gravitational lensing mass measurements in clusters of galaxies*, **Abriola, D.**, 2024, Strong Gravitational Lensing in the Era of Big Data. Edited by H. Stacey, A. Sonnenfeld, and C. Grillo. Proceedings of the International Astronomical Union, Volume 381, pp. 79-84 – [Paper page]

Acknowledgments